Slow and stopped light in negative refractive index waveguides

by

Edmund Ian Kirby

Submitted for the Degree of Doctor of Philosophy

Faculty of Electronic and Physical Sciences

Department of Physics

Advanced Technology Insitute

University of Surrey

November 2011

THESIS CONTAINS CD

Abstract

This thesis investigates the behaviour of light in waveguides with cores composed of a negative refractive index material. The ability of these structures to drastically slow and even halt light pulses is studied. The Finite-Difference Time-Domain computational simulation method is used to simulate these structures and the results produced are compared against those from analytic calculations.

It is observed that pulses in waveguides with thinner cores have smaller group velocities. By recording the change of the pulse's magnetic field with distance the pulse's effective refractive index is extracted and is found to match that calculated analytically. Reducing the magnitude of the core's intrinsic refractive index is also found to reduce the pulse's group velocity.

Due to the loss present in current negative refractive index materials, a method of supplying gain to the propagating pulse was investigated. This was achieved by placing a strip of gain material within the waveguide cladding. The gain supplied is found to increase when the separation between the strip and core is decreased, when the width of the strip is increased and when the width of the waveguide's core is reduced. Including the gain material creates a frequency region where the pulse experiences gain and the real part of its effective index is negative. Through recording the change in the pulse's magnetic field over time its complex frequency was extracted. Using the pulse's energy velocity it was possible to convert between the complex frequency and complex wavevector.

The use of a prism to couple to the waveguide was also examined. This allowed exceedingly slow modes, of the order of 0.00002c to be excited. It was discovered that keeping the prism in place once the light had coupled into the waveguide caused the value of the pulse's maximum wavevector component to shift.

Papers published

- E I Kirby, J M Hamm, K L Tsakmakidis and O Hess. FDTD analysis of slow light propagation in negative-refractive-index metamaterial waveguides. Journal of Optics A Pure and Applied Optics, 11, 114027, 2009

- E I Kirby, J M Hamm, T W Pickering, K L Tsakmakidis and O Hess. Evanescent gain for slow and stopped light in negative refractive index heterostructures. Phys. Rev. B, 84, 041103(R), 2011

Declaration

This thesis and the work to which it refers are the results of my own efforts. Any ideas, data, images or text resulting from the work of others (whether published or unpublished) are fully identified as such within the work and attributed to their originator in the text, bibliography or in footnotes. This thesis has not been submitted in whole or in part for any other academic degree or professional qualification. I agree that the University has the right to submit my work to the plagiarism detection service TurnitinUK for originality checks. Whether or not drafts have been so-assessed, the University reserves the right to require an electronic version of the final document (as submitted) for assessment as above.

Edmund Hirsby 08/05/2012

Contents

List of Figures

List of Tables

Glossary

$e^{i(kx-\omega t)}$	Spatial and temporal dependence of waves

Symbols

$\mathbf{E}$	Electric field vector
$\mathbf{B}$	Magnetic induction field vector
ρ	Volume charge density
σ	Surface charge density
ϵ_0	Free space permittivity
ϵ_r	Relative permittivity
ϵ_{cl}	Permittivity in cladding
ϵ_{co}	Permittivity in core
μ_0	Free space permeability
μ_r	Relative permeability
μ_{cl}	Permeability in cladding
μ_{co}	Permeability in core
$\mathbf{D}$	Displacement vector
$\mathbf{P}$	Polarisation vector
$\mathbf{H}$	Magnetic field vector
$\mathbf{M}$	Magnetisation vector
$\mathbf{j}$	Electric current density
$\mathbf{j}_f$	Free electric current density
$\mathbf{M}$	Magnetic current density
χ_e	Electric susceptibility of material
χ_m	Magnetic susceptibility of material

n	Refractive index
n_{eff}	Effective refractive index
v_p	Phase velocity
v_e	Energy velocity
c	Speed of light in vacuum
k	Wavevector $k = \left(\frac{2\pi}{\lambda}\right)$,$(k = \beta + i\alpha)$
k_0	Free space wavevector
β	Longitudinal propagation constant
α	Decay constant
λ	Wavevector
λ_0	Free space wavevector
$\mathbf{r}$	Displacement
ω	Angular frequency $(2\pi f)$
ω_p	Plasma frequency
Γ_e	Relaxation frequency
τ	Relaxation time
$\mathbf{S}$	Poynting vector
j_s	Surface currents
κ	Transverse propagation constant in the core
γ	Transverse propagation constant in the cladding
k_t	Generic transverse propagation constant
T_{att}	Duration of attack
T_{dec}	Duration of decay
T_{sus}	Duration of sustain

W	Energy density
S	Courant value
α_{abs}	Absorption Coefficient
U	Total energy stored in electromagnetic field
Q	Work done on charges by electromagnetic field
g	Pulse energy decay constant

Acronyms

ADE	Auxiliary Differential Equation
APM	Argument Principle Method
Arb.Units	Arbitrary Units
CW	Constant Wave
DMD	Dielectric Metal Dielectric
EIT	Electromagnetically Induced Transparency
EM	Electromagnetic
FDTD	Finite Difference Time Domain
FOM	Figure Of Merit
HWHM	Half Width Half Maximum
LHS	Left Hand Side
LHM	Left Handed Material
MDM	Metal Dielectric Metal
NRI	Negative Refractive Index
PBC	Periodic Boundary Conditions
PC	Photonic Crystal
PEC	Perfect Electric Conductor

PML	Perfectly Matched Layer
PRI	Positive Refractive Index
RH	Right Hand
RHS	Right Hand Side
SBS	Stimulated Brillouin Scattering
SPP	Surface Plasmon Polariton
SRR	Split Ring Resonator
TAC	Theory and Advanced Computation
TE	Transverse Electric
TFSF	Total Field Scattered Field
TM	Transverse Magnetic
TMM	Transfer Matrix Method

Acknowledgements

Throughout my PhD I have received immense help and support from other members of the Theoretical and Advanced Computation group at the University of Surrey.

I specifically want to acknowledge the support of Dr Joachim Hamm who is in charge of the group's FDTD code and who as well as creating many of the basic features of the FDTD program also created the material modules (NRI and Lorentz), the TFSF injection plane and the Energy box module which are used in this thesis.

I would also like to acknowledge Tim Pickering who as part of his PhD work created the analytic mode solver used in Chapter 5 and applied it to the structures I examined there.

I have also had numerous extremely useful talks with Dr Kosmas Tsakmakidis about aspects of the trapped rainbow concept and slow light.

My thanks also to: Andreas Pusch and Sebastian Wuestner who looked over later drafts of my thesis and the whole of the TAC group: Zeph Davies, Steven Hepplestone, James Cook, Durga Aryal, Sang Soon Oh, Klaus Boehringer and Richard Crowter whose friendships has helped to make my time in the group a happy one and I wish then all the best in the future.

I would like to thank my family for their constant support.

My thanks go to the EPSRC for funding this research.

Finally I wish to thank Professor Ortwin Hess for his encouragement and direction during my PhD.

Chapter 1

Introduction

1.1 Slow light

The term slow light seems almost paradoxical. In everyday language, the phrase "speed of light" is used to express the highest speed possible. However, this is only the case when light is propagating through a vacuum. When propagating through materials, the variety of velocities used to describe light can be smaller. The three most important of these velocities, with regard to the concept of slow light, are: the phase, group and energy.

The phase velocity is the most intuitive to understand. It is the velocity of points of constant phase, such as the velocity of the location of the maximum electric field intensity on each phase front. The phase velocity is obtained by dividing the speed of light in vacuum, c, by the refractive index of the medium through which the light travels.

Even though describing the behaviour of a single frequency is a useful mathematical tool, light beams are always composed of a range of frequencies. The constructive and destructive interference between these frequencies produce a pulse. The group velocity gives the speed of the pulse envelope. In a dispersion less medium, such as vacuum, each frequency propagates with the same phase velocity, resulting in the group and phase velocities being equal. However, in dispersive media, where the phase velocity of each frequency differs, the group velocity can take a wide range of values, including both faster and slower than that observed in vacuum [1].

The energy velocity of a light wave is defined by the energy flow rate, the Poynting vector, divided by the energy density of the wave [2]. In lossless materials, i.e. those where the light does not lose any energy, the energy and group velocities are identical. When loss is included calculations of the group velocity can lead to unphysical results and the energy velocity is the correct way to define pulse's velocity [2]. It is the group and energy velocities which are referred to when the term slow light is used.

In this thesis a novel method of slowing and even potentially stopping light is in-

vestigated. Slow light and the effects that it produces have many applications which are detailed below.

1.2 Applications of slow light

Telecommunications is one area of technology where the ability to control light is crucial. Light signals are commonly used as it allows data to be transfered at high speeds between and within networks. There are some situations, though, where being able to slow down light signals actually increases the performance of a network. The next three sections outline different areas which benefit through the incorporation of slow light.

1.2.1 Optical routers

Routers act as junctions in networks, receiving input signals and directing them to one of a number of outputs. Problems can occur, however, if two signals arrive simultaneously at the router; a so called contention issue [3]. The solution is to store one of the signals, while the other is being directed. Currently, with routers used to direct optical signals, this is achieved by converting the second signal into electronic form, which can then be stored. Once the first signal has been sent the second signal is then converted back into optical form and processed. The conversion from optical to electronic and back again takes time, and reduces the speed at which the router can work. Storing the signal through slowing the group velocity of its constituent optical pulses would enable the signal to remain in the optical form. This removes the lengthy conversion time to and from the electronic regime [4].

1.2.2 Optical switches

In the quest to reduce device size, lower power usage and increase the data rate of optical signal processing, work has been carried out into combining the different components of an optical circuit onto a single device [5]. An optical switch is one such component. One method of creating an optical switch is to use a Mach-Zehnder interferometer. Here, the light signal is split along the two arms of the interferometer and then recombined. By varying the phase change experienced by the light in one arm with respect to that in the other, the two signals will be out of phase when they recombine. If the phase difference between the two is π radians, then they will cancel each other. The interferometer will then be acting as a switch [6]. By varying the phase offset between the two signals from 0 to π radians, the device could also be used as a modulator [5].

The phase of the light is altered by varying the effective refractive index experienced by the light in the waveguide. This effective index emerges from the effect of the waveguide geometry and the intrinsic refractive indices of the waveguide's constituent materials. The intrinsic refractive index of the waveguide core material can be altered by changing the charge density within it [5]. This causes a shift, in frequency, of the dispersion curves, which describe for each mode the relationship between frequency and effective index. Due to this the effective index experienced at a particular frequency will also be shifted. Importantly, the shift in effective refractive index at a particular frequency is greater the slower the group velocity of the light at that frequency. This is due to a slower group velocity occuring at flatter parts of the dispersion curve. Therefore, to produce the greatest change in effective index (for as small a change in intrinsic index, and thus power, as possible), it is better for the light to be travelling as slow as possible. Thus, using slow light in such a device can improve its power efficiency.

1.2.3 Non-linear effects

Non-linear effects occur when light of sufficiently high intensity interacts with materials. These effects are used in many different areas. For instance, in optical switching it is possible for the refractive index in one arm of a Mach-Zehnder interferometer to be changed via the Kerr effect. Through this effect, the refractive index experienced by the optical signal is dependent on the intensity of the light [7]. When a slow light waveguide is used the energy intensity of the light is increased and so the Kerr effect is enhanced. The increase in the energy desnity of the pulse occurs as the pulse enters the slow light region and the front of the pulse is slowed down before the rear. This allows the rear of the pulse to catch up with the front and so the pulse is spatially compressed [6, 7]. This means that a lower intensity pulse can, in the slow light regime, achieve the same strength of Kerr interaction as a higher intensity pulse in a conventional waveguide.

Stimulated Raman scattering is another non-linear effect, that can be enhanced by using slow light. This effect can be used to pump light in silicon-on-insulator photonic crystals. As with the Kerr effect, this enhancement is due to the increase in the energy density of the pulse [8].

So, through increased energy density, the use of slow light can enhance non-linear effects. This would allow a reduction in both the power used to generate the initial pulse, and the physical size of some of the optical components.

1.3 Slow light methods

Several different methods of slowing light are being actively investigated. These include Electromagnetically Induced Transparency (EIT), Stimulated Brillouin Scattering (SBS) and Photonic Crystal waveguides (PC).

Most of these methods use a narrow resonance in the absorption spectrum of the material to produce a region of strong dispersion. The relation between the absorption and dispersion is given through the Kramers-Kronig equation. The dispersion in turn affects the group velocity. The two are related through:

$$v_g = \frac{\partial \omega}{\partial k}, \tag{1.1}$$

$$\frac{1}{v_g} = \frac{\partial k}{\partial \omega}. \tag{1.2}$$

The greater the variation in the wavevector with frequency (the dispersion), the smaller the group velocity [9].

Electromagnetically induced transparency is one method of achieving slow light. The general principle is to use a three level medium, in which two levels (1 and 2) couple to the same third level (level 3). Two light beams, a probe and a control, are used. The probe is set to the frequency of the transition between level-1 and level-3, while the control is set to the frequency of the transition between level-2 and 3. In the set-up used, no direct transition is possible between level-1 and level-2. If only the probe beam is sent through it is absorbed, due to atoms being excited from level-1 to level -3. If, however, the control beam is active at the same time as the probe it is possible to prevent any transitions to level-3. This is achieved if the probability amplitude of the transitions to level-3 from both level-1 and level-2 have the same frequency and are oppositely phased, ensuring that they destructively interfere [10]. With no transitions from levels 1 and 2 to level 3 no energy will be lost from the probe beam. This means the 3-level medium is now transparent to the probe frequency. This transparency region has a very small bandwidth which produces a sharp peak in the absorption spectrum. Through the Kramers-Kronig relation this leads to a steep gradient in the wavevector versus frequency dispersion curve, and via equation (1.2) a low group velocity [11].

The disadvantage of EIT is that experiments usually have to be performed at very low temperatures, which requires large and unwieldy equipment. There is also high absorption for frequencies that are outside the narrow transmission window.

Stimulated Brillouin scattering is another method that produces slow light, due to the creation of a sharp peak in the absorption spectrum. SBS has been observed in optical

fibres [12]. Here, two beams are used. One, the pump, supplies gain to the second, the probe. The coupling between the two is achieved by the high intensity pump scattering off a refractive index grating. This grating is produced in the fibre by an acoustic wave which the pump beam itself generates. If the parameters are chosen correctly, the frequency of the backward scattered wave will match that of the probe. As the probe is sent in from the opposite end of the fibre to the pump, the backward scattered wave can couple to the probe. Supplying energy to the probe creates a gain peak in the absorption spectrum [4]. This then leads to a region of high dispersion as with the EIT method.

There are two main advantages of this method. Firstly, it can operate at room temperature and, secondly, it can be implemented in optical fibres, which are ubiquitous in modern telecommunication technologies. However, only a small change in refractive index is found to be achievable using SBS, thus, the delay seen [12] is only possible using optical fibres over a kilometre in length.

The two methods described above generate a narrow feature in the imaginary part of the refractive index, i.e. the transparency region in the case of EIT and the gain region for SBS. This creates a rapid change in the real part of the refractive index and thus a reduction in the group velocity. A different method to produce slow light is used in Photonic Crystal (PC) waveguides.

A Photonic Crystal is formed by creating a regular pattern of regions of different refractive indices, for instance by cutting out an array of holes from a sheet of silicon. For wavevectors with wavelengths close to the spacing of these regions, the field profile distribution can take two forms. For low frequencies, the energy density of the fields is mainly situated in the regions of lower refractive index. For higher frequencies, it is mainly situated in the regions of higher refractive index. This creates a split in the photonic crystals dispersion band and produces stop bands. Frequencies situated in the stop band cannot propagate through the PC [13]. By removing a line of holes it is possible to create a waveguide since the frequencies within the stop band are prevented from propagating through the PC cladding surrounding this path.

Slow light can be produced in PC waveguides as they act as 1D Bragg gratings, scattering back certain frequencies. At the edge of the Brillouin zone, the phase of the backscattered light matches that of the forward propagating component, and interference takes place, which can result in a slow moving pulse envelope [6].

An advantage of PCs is that the slow light frequencies do not necessarily have to be located in regions of high dispersion. They can operate at room temperature and have already been used to produce slow light [14]. However, PCs suffer from loss as a consequence of extrinsic light scattering, which in turn is caused by surface roughness and any slight disorder in the positioning of the dielectric features [15].

1.4 Negative refractive index metamaterial waveguides

Recently a new method of slowing (potentially even stopping) light has been suggested [16, 17]. This method uses a waveguide comprised partly of a negative refractive index material [18]. The negative refractive index material could be created using metamaterials [19]. Unlike EIT or SBS, this method does not rely on having a sharp peak or dip in the imaginary part of the refractive index. Rather, as with Photonic Crystals, it has the potential to operate over a wider bandwidth and at room temperature.

The practical realisation of NRI materials has only been actively investigated for the last decade. At present, no bulk NRI material has been created. This is the type most commonly considered for use in NRI waveguides. As a result, investigations of NRI waveguides have to be carried out through either analytic calculations or computional simulations as is done in this thesis. An important aspect of current NRI materials is their high dissipative loss. To be of use in waveguides this loss will have to be compensated for. This is an area which is considered in this thesis.

1.5 Summary and thesis outline

As outlined above, the ability to slow light has the potential to be extremely useful in telecommunications and optical circuits. Although a number of methods already exist to slow down light, there is no clear favourite for widespread use. Photonic crystals and SBS are perhaps the most likely to be adopted into commercial use first, due to the relative ease of integrating them with existing technologies. However, the rapid development of NRI materials (described in the next chapter) means that NRI waveguides could, in the mid to far term, be a viable option to slow down and even stop light. It is these NRI waveguide structures which this thesis seeks to investigate. The thesis is organised as follows:

Chapter 2 provides background information on the topics covered in the thesis. It begins with an outline of how EM waves interact with materials. This describes the effects that materials have on EM waves and the parameters that define the optical properties of a material. By referring to the optical characteristics, the optical properties of NRI materials are discussed and compared with those of conventional positive refractive index (PRI) materials. To emphasise the possibility of bulk NRI materials being experimentally realised the field of metamaterials is introduced. Features of current metamaterial designs are described, as well as the issues which have to be overcome in order for their use to be a practical proposition. Having described NRI and NRI materials, the area of waveguide is detailed. Initially the basic principles of waveguides are outlined with concepts such as

light modes being examined. Using the basic principles of waveguides and NRI materials, the predicted properties of NRI waveguides are detailed. Particular attention is paid to the trapped rainbow concept which predicts that NRI waveguides could slow and even stop light. In addition to NRI waveguides other structures which could produce the trapped rainbow effect are examined. These are described since work conducted on them is applicable to NRI refractive index waveguides. The chapter finishes with a look at the issues surrounding the trapped rainbow concept, such as whether it is possible to stop light in NRI waveguides containing high dissipative loss.

The computational method which is used in the thesis is detailed in chapter 3 and appendix 8.1. In appendix 8.1 the basic principles of the FDTD method are outlined. The computational variables which could affect the simulation results, i.e. the Courant value and simulation resolution are also discussed here. The more non-standard aspects of the computational method used in the thesis are detailed in chapter 3. Here, the model implemented to simulate the NRI material is presented. A description is also given of the scheme used to extract the effective refractive index experienced by the pulse propagating through the waveguide. This extraction method is then tested by comparing the results it produces against those obtained from an analytic method.

Chapter 4 details the investigation into pulse propagation through loss-less NRI waveguides. In the first section the simulation setup is described, i.e. the types of simulation boundaries implemented, the resolution used and the Courant value set. The method used to inject light into the waveguide is then addressed. This method requires the transverse profile of the injected mode. The derivation of the equation used to calculate this profile is then given. Once the geometric setup and injection method have been outlined the investigations conducted are discussed. The first set of simulations investigate pulse propagation through loss-less waveguides with cores of different widths. The results from these are compared against results from analytic theory. Finally, a second method of implementing the trapped rainbow concept is examined; that of varying the core material's intrinsic refractive index. Again, the simulation results are compared against those from analytic theory.

Due to the high levels of dissipative loss belonging to current metamaterials any realised NRI waveguide will have high levels of absorption. The use of a gain material to overcome this loss is analysed in chapter 5. In the scheme used, a strip of gain material is placed within the waveguide cladding. The parameter extraction method is tested in situations where a light beam's amplitude increases. The stability of the simulations including loss is then examined with regard to different Courant and resolution values. Computational experiments are then conducted into the effect of varying both, the separation between the gain material and the core, and the width of the gain material strip.

The intrinsic loss of the NRI material is then adjusted to enable it to be compensated for by the gain material. A set of four simulations were conducted into the effects of including or excluding gain and loss in the waveguide. The invesigation was extended by recording the effect that varying the width of the waveguide core had with regard to the change in the amount of gain supplied to the propagating pulse. These results, as with those in chapter 4, are all compared against analytic theory. Finally, an attempt was made to adjust the frequency distribution of the loss experienced by the pulse through varying the intrinsic absorption of the gain material.

Chapter 6 examines the issues surrounding using a prism to couple to the stopped light mode of a NRI waveguide. As before, the effects of different compuational parameters are noted enabling their effects to be reduced in the subsequent investigations. Following this, issues relating to the removal of the prism once the light has been injected into the waveguide and the excitation of the correct mode parameters, are detailed.

The key results obtained are then reported in the concluding chapter, chapter 7. Ideas and avenues for future work are also outlined.

In summary, this thesis examins the use of NRI waveguides to both slow and stop light. These investigations are carried out via numerical computer simulations and analytical calculations. The thesis covers three main areas: first, the ability to slow down light through varying different waveguide parameters such as the width or refractive index of the waveguide's core. Second, the use of a gain material to compensate for the high amounts of intrinsic dissipative loss found in present NRI materials. Third, the issues associated with using a prism to couple into the stopped/slow light mode of a NRI waveguide.

Chapter 2

Background

2.1 Introduction

This chapter is divided into four main sections. The first briefly details Maxwell's equations and shows how they are adapted to account for the interactions between electric and magnetic fields and materials. The second explores the concept of a negative refractive index material, and explains the optical properties required in order for the material to have a negative refractive index. In the third, the field of metamaterials is examined as these are the materials which are being designed to have a negative refractive index. The final section examines the basic principles of waveguides and waveguides containing NRI materials, the unusual optical features NRI waveguides are predicted to have, and the work which has so far been carried out in examining them. Other waveguide geometries that have similar features to NRI waveguides are also looked at.

2.2 Electromagnetic waves and materials

2.2.1 Maxwell's equations

Maxwell's four equations are the most basic formulae used in electromagnetic (EM) theory. Faraday's (2.1) and Ampere's (2.2) laws describe the relation between the time varying electric $\mathbf{E}$ and magnetic induction $\mathbf{B}$ field vectors, whilst Gauss' electric and magnetic equations describe properties of static electric and magnetic fields. In vacuum Maxwell's equations, when expressed in SI units and assuming there are no electric or magnetic currents, take the form:

$$\nabla \times \mathbf{E} = -\frac{\partial \mathbf{B}}{\partial t}, \tag{2.1}$$

$$\nabla \times \mathbf{B} = \mu_0 \epsilon_0 \frac{\partial \mathbf{E}}{\partial t} + \mu_0 \mathbf{j}, \tag{2.2}$$

$$\nabla \cdot \mathbf{E} = \frac{\rho}{\epsilon_0}, \tag{2.3}$$

$$\nabla \cdot \mathbf{B} = 0. \tag{2.4}$$

Quantities included in the formulae, in addition to the electric field and magnetic induction vectors, are the charge density ρ, the free space permittivity ϵ_0 the free space permeability μ_0 and the current density source term $\mathbf{j}$. The free space permittivity and permeability describe the properties of vacuum as experienced by the electric and magnetic fields respectively. The current density source term can be split into two components, the first describes the contribution due to bound charges (usually included via the polarisation $\mathbf{P}$) and the second relates to the contribution due to free current, $\mathbf{j}_f$.

Faraday's (2.1) and Ampere's (2.2) laws describe how EM waves propagate. Ampere's law shows that an electric field varying with time induces a circulating magnetic field. The strength of this magnetic field is related to the rate of change of the electric field. The effect of this varying magnetic field is, as described by Faraday's law (2.1), to create a new circulating electric field. The minus sign in (2.1) shows that the newly created E-field opposes the original E-field, thus preventing positive feedback that would result in a non physical energy increase. This cycle of B-field generating E-field, which subsequently produces another B-field, repeats itself, and through this an EM wave can propagate.

Maxwell's equations (2.1)-(2.4) are sufficient to describe the behaviour of EM fields in vacuum. However, when light propagates through a material additional terms have to be added to account for the effect of both the EM wave on the material, and the material on the fields comprising the EM wave.

2.2.2 Electric field in a material

An external electric field, such as the one generated in an EM wave, produces a force upon the charges within the medium it passes through. These could be bound charges, such as orbital electrons in the atoms or molecules comprising the material, or charges which are not bound but drift freely, such as conduction electrons in metals.

This EM force separates the positive and negative charges. Conduction electrons are offset relative to the positively charged nuclei of the metallic lattice. Separating the charges generates a polarisation $\mathbf{P}$ within the material. The polarisation vector points from the positive to the negative charge and can be summed with the initial external

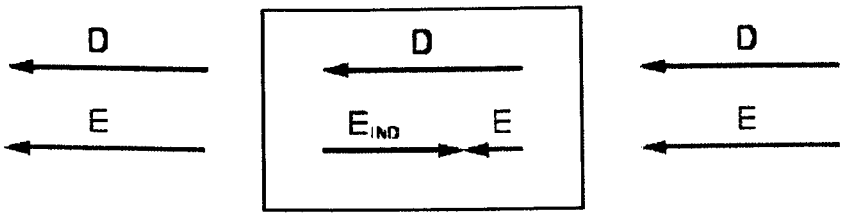

Figure 2.1: E-field (E) in a polarisable material relative to the displacement vector (D) and induced E-field (E_{IND}). If there are no free charges on the surface of the material then the displacement vector inside the material is the same as outside.

E-field. The resultant vector is defined as the displacement vector $\mathbf{D}$, therefore:

$$\mathbf{D} = \epsilon_0 \mathbf{E} + \mathbf{P}. \tag{2.5}$$

This displacement vector can either be greater or smaller than the initial external E-field, depending on the magnitude and direction of the polarisation vector. This in turn depends on the properties of the material and the frequency of the incident EM wave.

If there are no bound charges present, then the displacement vector is identical to the external E-field vector. If, however, there is a polarisable dielectric then the external E-field polarises the dielectric and creates surface charges on the dielectric's edges. These surface charges induce an E-field ($\mathbf{E}_{IND}$), which acts against the external field. The resultant E-field is the product of both the initial external E-field, and the induced E-field. Since the induced E-field acts in the opposite direction to the external field, the resultant E-field can be smaller than the external field, as in figure 2.1[20]. Furthermore, in some cases, if the polarisation is stronger than the external field, the resultant E-field can act in the opposite direction to the initial external field.

The polarisation can be included in Ampere's law as another source term for the magnetic inductance:

$$\nabla \times \mathbf{B} = \mu_0 \epsilon_0 \frac{\partial \mathbf{E}}{\partial t} + \mu_0 \frac{\partial \mathbf{P}}{\partial t} + \mu_0 \mathbf{j}_f. \tag{2.6}$$

Alternatively, the displacement vector can be used in Ampere's equation so that the polarisation is automatically included:

$$\nabla \times \mathbf{B} = \mu_0 \frac{\partial \mathbf{D}}{\partial t} + \mu_0 \mathbf{j}_f. \tag{2.7}$$

These updated versions of Ampere's law, equations (2.6) and (2.7) , show that the

value of the magnetic induction field produced is now dependent not only on the pre-existing electric field of the EM wave (the external E-field), but also on the polarisation it induces within the material it travels through. In the rest of this thesis the it is assumed that there is no free current so $\mathbf{j}_f = 0$.

The effect of a medium on the electric field can be quantified through defining the material's relative permittivity ϵ_r, i.e. the relation between the initial external E-field and the displacement field vector. To obtain the relative permittivity, the polarisation of the material is defined in terms of the external E-field and the material's electric susceptibility χ_e. If we assume the relationship between the polarisation density and electric field is linear and isotropic then, the polarisation is defined as:

$$\mathbf{P} = \chi_e(\epsilon_0\mathbf{E}). \tag{2.8}$$

It should be noted that this relationship might not always be linear. If, for instance, an external E-field of high amplitude is used, non-linear effects could occur. However, in this work only the linear relation is considered.

If the polarisation equation (2.8) is substituted into the displacement vector equation (2.5), and the E-field and vacuum permittivity values factored out, the displacement vector can be given as:

$$\mathbf{D} = \epsilon_0(1 + \chi_e)\mathbf{E}. \tag{2.9}$$

The relative permittivity can thus be defined as $\epsilon_r = 1 + \chi_e$. The product of the relative permittivity and permittivity of free space then gives the permittivity ($\epsilon = \epsilon_0\epsilon_r$). A new equation for the displacement field can then be produced:

$$\mathbf{D} = \epsilon\mathbf{E}. \tag{2.10}$$

Equation (2.10) can now be substituted into equation (2.7). This allows the effect of the material through which the EM wave is travelling to be completely defined using its relative permittivity:

$$\nabla \times \mathbf{B} = \mu_0\epsilon\frac{\partial \mathbf{E}}{\partial t}. \tag{2.11}$$

The ability to incorporate the material response in this manner makes it easier to

examine the effects that materials, such as those with a negative refractive index, have on propagating EM waves.

2.2.3 Magnetic field in a material

The response of a material to the magnetic field component of an EM wave is included in a similar manner to the response to the electric field. In this case, the external **B**-field of the EM wave can generate a dipole moment within the material, either through inducing it, such as in diamagnetic materials, or aligning pre-existing dipole moments, such as in paramagnetic materials [20].

As with the E-field, to obtain the magnetic field requires the induced field (the dipole moment, or magnetisation **M**) to be summed with the initial external field (the magnetic inductance **B**). The resulting vector is defined as the magnetic field **H** and can be given by:

$$\mathbf{H} = \frac{\mathbf{B}}{\mu_0} - \mathbf{M}. \tag{2.12}$$

The magnetisation can be redefined using the magnetic field vector to give:

$$\mathbf{M} = \chi_m \mathbf{H}. \tag{2.13}$$

In this formula, χ_m is the magnetic susceptibility, as with equation (2.8) it is assumed that the relation between the magnetic field and the magnetisation is linear and isotropic. By substituting equation (2.13) into equation (2.12), and then rearranging and factoring out the magnetic field vector, we arrive at:

$$\mathbf{B} = \mu_0(1 + \chi_m)\mathbf{H}, \tag{2.14}$$

$$\mathbf{B} = \mu_0\mu_r\mathbf{H}. \tag{2.15}$$

In parallel to the electric case, we can define the relative permeability as $\mu_r = 1 + \chi_m$. The free space and relative permeability can be combined into the permeability μ:

$$\mathbf{B} = \mu\mathbf{H}. \tag{2.16}$$

If we substitute equation (2.16) into both Faraday's (2.1) and Ampere's laws (2.2), and

change the free space permeability in Ampere's law to the permeability (μ), then we can see how the relative permeability can be included. As such:

$$\nabla \times \mathbf{E} = -\mu \frac{\partial \mathbf{H}}{\partial t}, \tag{2.17}$$

$$\nabla \times \mathbf{H} = \epsilon \frac{\partial \mathbf{E}}{\partial t}. \tag{2.18}$$

Thus, the permittivity and permeability affect the magnitude and, potentially, the sign of the induced magnetic and electric fields respectively. Later, these terms will be used to examine the optical properties of NRI materials.

2.3 Refractive index

2.3.1 Phase velocity

As has been seen, the effect of a material on electromagnetic radiation passing through it can be determined by the values of the material's permittivity and permeability. These two parameters can be combined to give the material's refractive index, n :

$$\mathrm{n} = \sqrt{\epsilon_r \mu_r}. \tag{2.19}$$

The refractive index is a dimensionless quantity, and is used to describe wave properties of the EM field. For example, the dynamics of a linearly polarised EM wave can be expressed using the wave equation:

$$\frac{\partial^2 \mathrm{E_z}}{\partial x^2} = \epsilon\mu \frac{\partial^2 \mathrm{E_z}}{\partial t^2}. \tag{2.20}$$

Equation (2.20) represents the case where the orientation of the E- and H-fields remain constant (unlike in circularly polarised waves), and the wave is propagating along the x-axis whilst having its E-field orientated along the z-axis and its H-field along the y-axis.

As with other wave equations, the phase velocity v_p of the propagating wave can be calculated using the terms in front of the time derivative in the wave equation. For equation (2.20), this gives:

$$v_p^2 = \frac{1}{\epsilon\mu}, \tag{2.21}$$

$$v_p = \pm\frac{1}{\sqrt{\epsilon\mu}}. \tag{2.22}$$

The phase velocity of light in vacuum is commonly referred to as c. Using equation (2.22) (and remembering that the permittivity and permeability in vacuum are defined as ϵ_0 and μ_0 respectively), allows us to write:

$$\mathrm{c} = \frac{1}{\sqrt{\epsilon_0\mu_0}}. \tag{2.23}$$

Both the permittivity and permeability have previously been defined as the product of the vacuum (or free space) value and the relative value in the medium. Using this relation, along with equations (2.19), (2.22) and (2.23), it is possible to include the refractive index into the equation for the phase velocity, thus:

$$v_p = \pm\frac{1}{\sqrt{\epsilon_0\mu_0}\sqrt{\epsilon_r\mu_r}} = \frac{\mathrm{c}}{\mathrm{n}}. \tag{2.24}$$

In equation (2.24) it can be observed that the refractive index of a material is the ratio between the phase velocity of light in vacuum and in the material. The refractive index therefore indicates the degree to which the phase velocity is reduced within the material.

2.3.2 Angle of refraction

As with any sinusoidally varying wave, the E- or H-field of an EM wave can be expressed in exponential form:

$$\mathbf{E}(\mathbf{r},t) = \mathbf{E}_0 e^{i(\mathbf{k}.\mathbf{r}-\omega t)}, \tag{2.25}$$

E_0 is the amplitude of the E-field, $\mathbf{r}$ is the displacement from the origin, and the wavevector $\mathbf{k}$ gives the number of wavelengths per unit distance along the propagation direction of the wave's phase fronts. The scalar product $\mathbf{k}.\mathbf{r}$ defines the distance, in terms of wavelengths, between the origin and point $\mathbf{r}$. The temporal separation between time zero and the present is given by t, and the angular frequency ω defines the number of cycles per unit time multiplied by 2π. As such the product ωt gives the duration, in units

of wave periods, between the start time ($t_0 = 0$) and time t, again multiplied by 2π. The exponent $\mathbf{k}.\mathbf{r} - \omega t$ gives the phase of the wave at point $\mathbf{r}$ and time t. The same equation can be written for the H-field. The frequency of an EM wave remains the same when it moves from one medium to another. However, the phase velocity of the wave varies with the material the wave is propagating through.

The direction of $\mathbf{k}$ is determined by the orientation of the E- and H-fields. The relation between these three quantities, obtained through substituting equation (2.25) and the H-field equivalent into Faraday's and Ampere's equations, is:

$$\mathbf{k} \times \mathbf{E} = \omega\mu\mathbf{H}, \tag{2.26}$$

$$\mathbf{k} \times \mathbf{H} = -\omega\epsilon\mathbf{E}. \tag{2.27}$$

At the interface between two media, the incident wave splits into two: the transmitted wave, which propagates into the second medium, and the reflected wave, which remains in the first medium. The phase of all three waves has to be the same at the interface. If we state that the situation is examined when t = 0, then in order for the phase of the three waves to be equal it is required that:

$$e^{i(\mathbf{k}_i.\mathbf{r})} = e^{i(\mathbf{k}_r.\mathbf{r})} = e^{i(\mathbf{k}_t.\mathbf{r})}, \tag{2.28}$$

$$\mathbf{k}_i.\mathbf{r} = \mathbf{k}_r.\mathbf{r} = \mathbf{k}_t.\mathbf{r}. \tag{2.29}$$

The scalar products can be expressed in terms of their components, for example $\mathbf{k}_i.\mathbf{r} = k_{ix}x + k_{iy}y + k_{iz}z$. If it is taken that the material interface is at point x=0, and the plane of incidence is the xy plane, this allows the wavevector component along the z direction to be set to zero. Equation (2.29) can thus be written as:

$$k_{iy} = k_{ry} = k_{ty}, \tag{2.30}$$

$$|\mathbf{k}_i| sin(\theta_i) = |\mathbf{k}_r| sin(\theta_r) = |\mathbf{k}_t| sin(\theta_t). \tag{2.31}$$

To examine refraction, it is only necessary to look at the incident and transmitted waves and to remember that the wavevector can be written as $\frac{2\pi}{\lambda} = \frac{n2\pi}{\lambda_0}$. Thereby rearranging equation (2.31) allows the relation between the incident and transmitted waves to be found:

$$\frac{sin(\theta_i)}{sin(\theta_t)} = \frac{|\mathbf{k}_t|}{|\mathbf{k}_i|}, \tag{2.32}$$

$$\frac{sin(\theta_i)}{sin(\theta_t)} = \frac{n_t}{n_i}. \tag{2.33}$$

As such, the angle of refraction is affected by the refractive index and thus the permittivity and permeability of the two media.

2.3.3 Negative refractive index (NRI)

As described earlier, the permittivity and permeability of a material defines its effects on the EM waves propagating through it. These two parameters can have various values in different materials. In parametric magnetic materials the permeability can be greater than 1, while in a diamagnetic material the permeability can be less than 1 [20] (though it still has to be positive). The permittivity value, too, can differ between materials. In metals at some frequencies it can even become negative.

Although a range of permittivity and permeability values exist in naturally occurring materials none with a negative permeability have been found so far and, therefore, neither has a material with both a negative permittivity and permeability. Despite the absence of such materials in 1964 a Russian scientist, V. G. Veselago, investigated theoretically the optical properties that a material with both a negative permittivity and permeability would have [18].

His initial step was to simply substitute negative values for the permittivity and permeability into Maxwell's equations. An immediate consequence was that equations (2.26) and (2.27) had to be re-written as:

$$\mathbf{k} \times \mathbf{E} = -|\mu|\omega\mathbf{H}, \tag{2.34}$$

$$\mathbf{k} \times \mathbf{H} = |\epsilon|\omega\mathbf{D}. \tag{2.35}$$

As such, the sign of the RHS of both equations is reversed. The effect of this alteration is to change the orientation of the $\mathbf{k}$, $\mathbf{E}$ and $\mathbf{H}$ vectors from that of a right handed triad to a left handed one. As a consequence, NRI materials are somethimes referred to as Left Handed Materials (LHM). The direction of an EM wave's k-vector will thus be reversed in NRI and PRI materials, provided the E- and H-fields have the same orientation in both, see figure 2.2.

Just as interesting, however, is what is not changed. The $\mathbf{k}$ vector details the propaga-

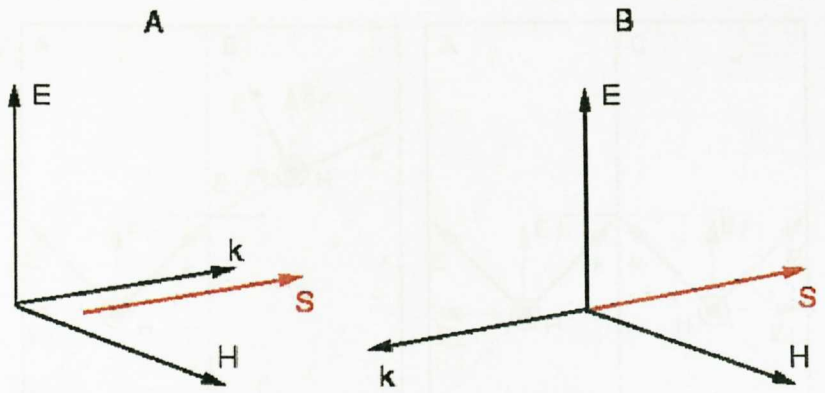

Figure 2.2: Relative orientations of E-fields, H-fields and wave (k) and Poynting (S) vectors in positive (A) and negative (B) refractive index materials

tion direction of the phase fronts of the EM wave. The direction of energy propagation is given by the Poynting vector **S**. As oscillating E- and H-fields are used in this thesis, the time averaged Poynting vector is required. This is given by [21]:

$$< \mathbf{S} > \; = \; \frac{1}{2}\mathrm{Re}(\mathbf{E} \times \mathbf{H}^*). \tag{2.36}$$

Since neither the permittivity nor permeability appear in equation (2.36), the direction of energy flow, relative to the direction of the E- and H-fields, is the same in the two materials, i.e. these three vectors always form a RH triad. Therefore, in homogeneous NRI materials the direction of energy flow is in the opposite direction to the direction of phase front propagation.

2.3.4 Negative refraction

The interface between a PRI and a NRI material is another area where Veselago predicted interesting optical effects would occur. To understand what happens to an EM wave propagating from one material into another, boundary equations are used. These equations detail the behaviour of the electric and magnetic field vectors at an interface between different media, and are derived from Maxwell's equations. They can be represented thus:

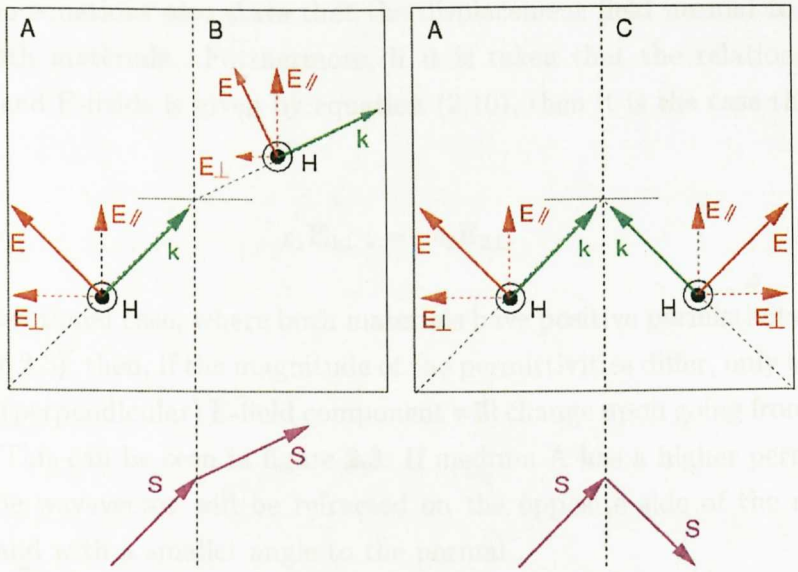

Figure 2.3: Refraction of a p-polarised light wave incident from vacuum (material A, refractive index = 1) into a PRI material (material B, refractive index = 2) and a NRI material (material C, refractive index = -1). The E-field components parallel to the material interface ($E_{\parallel}$) and perpendicular to the interface ($E_{\perp}$) are given along with the wavevector (k). The directions of the Poynting (S) vectors in both situations are also shown.

$$\begin{aligned} \mathbf{n}_{12}.(\mathbf{D}_2 - \mathbf{D}_1) &= \sigma_s, \\ \mathbf{n}_{12} \times (\mathbf{E}_2 - \mathbf{E}_1) &= 0, \\ \mathbf{n}_{12}.(\mathbf{B}_2 - \mathbf{B}_1) &= 0, \\ \mathbf{n}_{12} \times (\mathbf{H}_2 - \mathbf{H}_1) &= j_s. \end{aligned} \tag{2.37}$$

The free charge density at the material interface is written as σ_s , while the surface current at the material interface is written as j_s. In the absence of free surface charges or currents, which is assumed here, the boundary equations specify that the components of the E- and H-fields, parallel to the interface, should be equal in both the PRI and NRI materials. This should also be true for the components of the D- and B-fields, normal to the interface.

Figure 2.3 depicts two cases of a ray incident upon the interface between two materials. If the light is p-polarised, then the H-field is parallel to the interface, and the E-field has components parallel and perpendicular to the interface. From the boundary equations (2.37), both the H-field and the parallel component of the E-field are equal in both

materials. The equations also state that the displacement field normal to the interface is equal in both materials. Furthermore, if it is taken that the relation between the displacement and E-fields is given by equation (2.10), then it is the case that:

$$\epsilon_1 \mathbf{E}_{1\perp} = \epsilon_2 \mathbf{E}_{2\perp}. \tag{2.38}$$

In the conventional case, where both materials have positive permittivity (materials A and B in figure 2.3), then, if the magnitude of the permittivities differ, only the magnitude of the normal (perpendicular) E-field component will change upon going from one medium to the other. This can be seen in figure 2.3. If medium A has a higher permittivity than medium B, the wavevector will be refracted on the opposite side of the normal to the incident ray, and with a smaller angle to the normal .

However, where the light is incident onto a material with a negative permittivity (as is the case with materials A and C), then the direction of the normal component of the E-field is reversed, relative to its direction in medium A. This means that the refracted ray is on the same side of the normal as the incident ray. In addition, in medium C the wavevector points towards the interface rather than away, as in the conventional case. Although this seems unphysical it must be remembered that in a NRI material (as has been shown) the direction of energy flow is opposite to that of the wavevector. Thus, even though the wavevector is directed towards the interface in medium C, the energy still flows away from it. Negative refraction also occurs for s-polarised light. (Although, in this case, it is the normal H-field component that is reversed due to the negative permeability of medium C, while the E-field, now parallel to the interface remains constant.)

2.4 Metamaterials

2.4.1 Basic concepts

Although Veselago could describe in detail the properties of a material with a NRI, the work was still very much hypothetical since no materials with a NRI had been found or created at the time.

It was not until 30 years later that the creation of a material with a NRI began to seem possible. The first step, the outlining of a method to adjust a material's permittivity, was achieved by Pendry *et al* [22]. This work described how the position of a material's plasma frequency (ω_p) can be specified by artificially tailoring the medium's subwavelength structure. Although metals can have a negative permittivity (the plasma frequency defines the frequency below which the metal's permittivity is negative), using

this negative permittivity is difficult. There is only a finite frequency region in which a metal has a negative permittivity and small amounts of loss. At lower frequencies the losses in metals become significant, and the negative permittivity is irrelevant. By shifting the plasma frequency, the location of the bandwidth region where the material has both a negative permittivity and low losses can be adjusted to a more desirable frequency.

The plasma frequency is the resonance frequency of the negatively charged electron cloud, relative to the positively charged nuclei comprising the material lattice. The frequency of the resonance depends on both the density of electrons, and their effective mass.

Both of these parameters, it was discovered, could be controlled if the medium was composed not of a bulk material, but of a grid of metallic wires. The total volume of the wires would be less than that of a bulk material, reducing the density of electrons. In addition, any current generated in the wires via the electric field of the EM wave would, through Lenz's law, induce a magnetic field orientated so as to produce a force on the electrons opposing this motion. The extra force required to overcome this induced force would be equivalent to an increase in the electron's effective mass.

While metals naturally have a negative permittivity, no naturally occurring material has been found with a negative permeability. The weak interaction of the magnetic component of the EM field with the constituents of the materials makes it hard for the permeability of a medium to differ from 1. A method of strengthening this coupling was devised by Pendry *et al.* [23]. As the permittivity could be adjusted by including artificial components within the medium, they reasoned a similar effect could be achieved for the permeability. Instead of wires, however, subwavelength structures, which would have a large magnetic response when they interact with the magnetic field component of the EM wave, could be used.

These structures took the form of electronic circuits, containing both a capacitance and an inductance, and therefore having a resonance. One of the designs proposed was of two concentric rings, each having a section removed and arranged so the missing sections were facing in opposite directions [23]. This structure was named a Split Ring Resonator, SRR. It was envisioned that these SRRs could be arranged in an array to form an artificial medium. If the H-field of the EM wave is orientated along the axis of the SRR (i.e. perpendicular to the plane of the rings), then electric currents are induced in the rings. This, in turn produces an induced magnetic dipole, which interacts with the external H-field. The dispersion curve produced by the SRRs for the material's permeability takes the shape of a Lorentz dispersion curve in the presence of loss. At frequencies below the resonance frequency the permeability value takes larger values, while at frequencies above the resonance smaller values of permeability are generated. By careful design of the SRR

components it might be possible to cause the smaller values of permeability, which occur at frequencies slightly higher than that of the resonance, to become smaller than -1. In the frequency range where the permeability is smaller than -1 the induced magnetic field is directed opposite to the initial external field and is of greater magnitude. By varying the design and spacing of the SRR, the frequency at which the resonance occurs could be adjusted (in a similar manner to that of the wires for the permittivity).

Even though the SRR could generate a magnetic field antiparallel to the external H-field, there is a question of whether this can be interpreted as a negative permeability. Assigning a material a permittivity and permeability implies that it can be described as a homogeneous medium, i.e. the permittivity and permeability are the same at any point within the medium. However, if a material is composed of discrete structures, such as SRR, then the induced magnetic field will not be homogeneous, but rather stronger in regions close to the SRR. This line of argument, however, if followed to its ultimate conclusion, would preclude any material from being described as having a bulk permittivity or permeability. All materials are, ultimately, constructed of discrete units, i.e. atoms or molecules. What determines whether assigning a material an effective permittivity and permeability is appropriate is whether the incident light behaves as if the material is homogeneous or a collection of discrete elements. This is determined by the ratio between the light's wavelength and the dimensions of the material's constituent elements. Provided the SRRs are sufficiently smaller than the wavelength of the incident light, the light experiences an effective permeability that is uniform across the entire medium.

Following the proposal of the wires and SRRs, efforts were made to combine the two and produce the first NRI material. This work was initially conducted in the microwave regime, which, having wavelengths of the order of centimeters, made it comparatively easy to manufacture components small enough for the material to be considered homogeneous. The first successful demonstration of a NRI material was by Smith *et al.* [24]. Here, the NRI was verified by creating a material which was opaque in a certain frequency band when only wires were included, suggesting that at those frequencies it had a negative permittivity but positive permeability. Upon the insertion of SRRs, the material became transparent; an effect which was explained by the creation of a negative permeability.

A demonstration of negative refraction soon followed, with the creation of a prism out of a 2D arrangement of wires and SRRs by Shelby *et al.* [25]. This metamaterial refracted a 10.5 GHz microwave beam onto the same side of the normal axis as it was incident from. When a PRI material was used for the prism, the beam was refracted on the same side of the normal to that it was incident upon.

These results provided convincing evidence that a material with a NRI is a practical proposition.

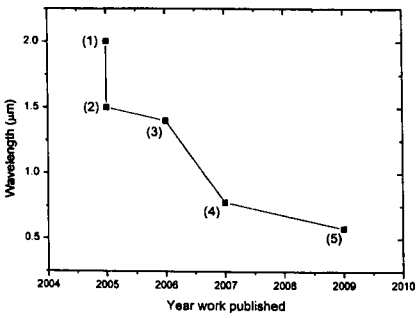

(a) Wavelength at which negative refraction occurs

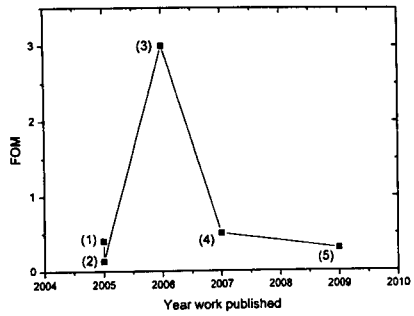

(b) FOM obtained for negative refractive index materials

Figure 2.4: Progress in metamaterial design: Zhang *et al* [26] (1), Shalaev *et al* [27] (2), Dolling *et al* [28] (3), Dolling *et al* [29] (4) and Xiao *et al* [30] (5)

2.4.2 Achieving higher frequencies and lower loss

Early experimental demonstrations of NRI metamaterials used microwaves [24, 25]. Many of the applications envisioned for metamaterials, however, are for frequencies in the visible or telecommunication regimes, such as for use in optical switches with wavelengths in the nm and μm range. The creation of metamaterials, which can operate in these areas of the EM spectrum, has been the focus of research over the last decade, see figure 2.4a.

A number of different geometries were investigated in order to incorporate the structures producing the effective permittvity and permeabilty onto a single material. A Metal-Dielectric-Metal (MDM) stack of thin layers with an array of holes cut out from it was one of the first structures tested and is an early example of the so called "fishnet" design. The metal layers acted as both the inductive elements for the generation of the magnetic dipole, and as a grid of wires to affect the permittivity [26]. Arrays of split wire pairs were also considered [27]. The arrangement which has proved to be the most successful, in terms of scaling to higher frequencies, is a slightly more complicated "fishnet" structure 2.5.

This design again uses a MDM layered structure but the surface patterning can be thought of as a grid, with thin wires along one axis and wider wires along the other. The surface is orientated so that the E-field component of the incident EM wave is directed along the thin wires (figure 2.5a), as in [22], while the H-field component is parallel to the thicker wires (figure2.5b) . The H-field can then generate currents across the thicker wires, with the dielectric spacer between the metal sheets acting as a capacitor. This circulating current generates a magnetic dipole.

Although work on the fishnet design has reached the point where a NRI at telecommunication and even visible wavelengths is possible [28], there are drawbacks with the

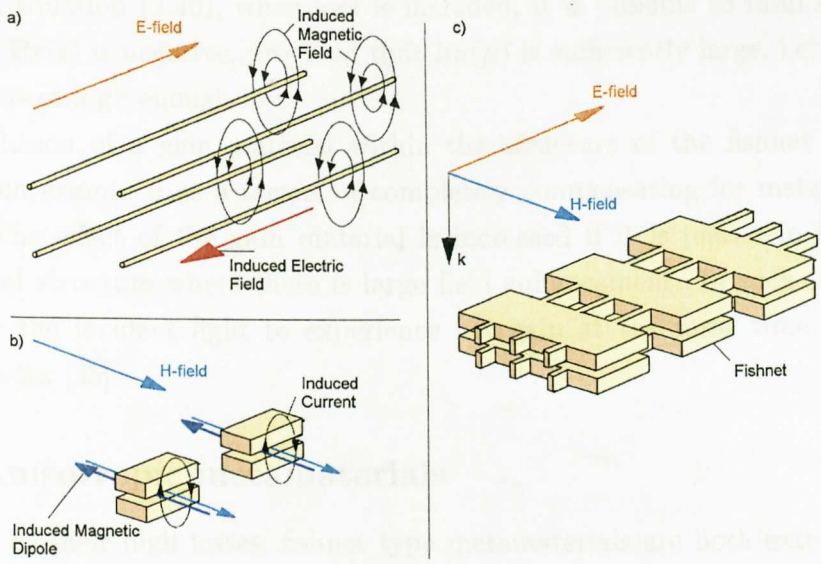

Figure 2.5: Fishnet structure a) Array of metal wires to produce negative permittivity, b) Cut wire pairs used to produce negative permeability and c) Composite "fishnet" structure containing both wires and cut wire pairs.

design as it suffers from high losses. The figure of merits (FOMs) for the materials are plotted in figure 2.4b , where:

$$\text{FOM} = \frac{-|\text{Re(n)}|}{\text{Im(n)}}. \tag{2.39}$$

These high loss values occur from a combination of factors. Firstly, high levels of intrinsic loss are associated with metals at frequencies approaching the metal's plasma frequency [29]. Secondly, the broadening of the material resonance due to surface roughness [30]. Lastly, many of the materials referenced in figure 2.4a do not actually have a negative permeability. It is still possible, however, for a negative refractive index to exist in these materials. When loss is included in the material's permittivity and permeability, an alternative criterion for the existence of negative refraction must be used [31, 32]:

$$\text{Re}(\epsilon)\text{Im}(\mu) + \text{Im}(\epsilon)\text{Re}(\mu) < 0. \tag{2.40}$$

This criterion is applicable for passive materials [31, 33] (i.e. not when gain is present), $\text{Re}(\epsilon)$ and $\text{Im}(\epsilon)$ are the real and imaginary parts of the permittivity, respectively, while $\text{Re}(\mu)$ and $\text{Im}(\mu)$ are the real and imaginary parts of the permeability, respectively. When loss is included the imaginary components of the permittivity and permeability become

positive. In equation (2.40), when loss is included, it is possible to fulfil the inequality even if only $\mathrm{Re}(\epsilon)$ is negative, provided that $\mathrm{Im}(\mu)$ is sufficiently large, i.e. the magnetic field experiences high enough loss.

The inclusion of a gain material within the structure of the fishnet metamaterial has also been examined as a means of completely compensating for metal's dissipative loss [34]. The effect of the gain material is increased if it is placed in regions of the metamaterial structure where there is large field enhancement. In such structures it is possible for the incident light to experience net gain at the same time as a negative refractive index [35].

2.4.3 Anisotropic metamaterials

In addition to their high losses, fishnet type metamaterials are both extremely difficult to fabricate and are anisotropic, i.e. the behaviour of light in the material is affected by the angle of incidence of the light. In all of the designs detailed in the previous sections, the metamaterial is orientated so that light is incident at an angle close to the normal of its surface. For some of the structures shown, the polarisation of the light also has an effect, for example the fishnet design in [28]. The E-field component has to be orientated along the thin wires to produce the negative permittivity, and the H-field along the wider wires so that the magnetic dipole can be generated.

Although this anisotropic behaviour is a drawback, there are situations where a homogeneous NRI is not an essential requirement. Waveguides are a prime example of this kind of structure, since most of the interesting effects only require the direction of the Poynting and wavevector components to be reversed along a single axis. Therefore, for the correct polarisation, a waveguide containing an anisotropic metamaterial will have the same properties as one with an isotropic metamaterial. If only anistropic metamaterials are required for a device then more simple designs of metamaterials can be used.

A layered structure composed of alternating $\epsilon < 0$ and $\epsilon > 0$ materials is one of the simplest anisotropic metamaterial designs. If an extraordinary wave is used (where the propagating mode's E-field is orientated along the optical axis of the layered material, i.e. across the layers), then the sign of the Poynting vector component directed along the wave's propagation direction depends on the component of permittivity along the optical axis [36]. The value of the permittivity components is determined by both the intrinsic refractive index of the materials comprising the layers and the relative proportions of each material. Through the careful selection of these parameters the direction of the Poynting vector can be made antiparallel to the phase velocity. This allows features predicted in waveguides containing bulk NRI materials to exist when anisotropic materials are used[37, 38].

A disadvantage with an anisotropic waveguide is that it can only support one polarisation, whereas a waveguide with a bulk anisotropic NRI material would be able to support all polarisations.

2.5 Waveguides

2.5.1 Basic concepts

Waveguides confine light inside a region (the core), allowing it to be directed along a predefined path. In waveguides composed of dielectric materials the confinement mechanism is total internal reflection, where light propagating inside the core is completely reflected at the interface between the core and the surrounding (cladding) material. For light waves to undergo total internal reflection at the interface, the refractive index of the core material needs to be sufficiently higher than that of the cladding, and the angle between the normal to the interface and the incident light ray to be greater than the critical angle. The E- and H-fields of totally internally reflected light are depicted as undergoing an exponential decay as they extend from the interface into the cladding. For bulk waveguide modes, the field in the core has a sinusoidal distribution. It is these modes which are examined in this thesis.

Due to its confinement, the propagation characteristics of light along the waveguide differ from those it would have in regions composed solely of either the core or cladding material.

The light wave in a waveguide can be analysed using two variables: its longitudinal propagation and transverse wavevectors. The longitudinal propagation wavevector β is the wavevector component of the light orientated along the axis of the waveguide. The transverse wavevector κ is the component directed across the waveguide in the direction along which the wave is confined. These two components are related to the light's wavevector through the conventional relation:

$$k^2 = \beta^2 + \kappa^2. \tag{2.41}$$

Here, k is the wavevector of the light within the core material. The longitudinal wavevector is particularly important, since the effective refractive index (n_{eff}) can be obtained from it, thus:

$$\beta = n_{eff} k_0, \tag{2.42}$$

with k_0 being the free space wavevector. Calculating the effective index allows the effect of the waveguide on the propagating light to be expressed in terms of a hypothetical uniform medium, with a refractive index n_{eff}.

Only waves with certain values of β are bound within any particular waveguide. These can be determined using both the field distribution of the E- and H-field components and the boundary conditions. These conditions require that the E- and H-field components orientated parallel to the interface in the core and cladding regions are equal at the interface.

The fact that only waves with certain values of β can exist can be found by examining the component of the propagating wave directed across the waveguide. The wavevector of this component κ is related to β through the trigonometric relation $\beta = \kappa\tan(\theta)$, where θ is the angle between the wavevector and the normal to the surface. The phase change undergone by the light as it crosses the core is $2\alpha\kappa$, where 2α is the core width. When the light undergoes total internal reflection there is an additional phase change, denoted as ϕ. Therefore, in a complete round trip, where, the light travels across the waveguide, is totally internally reflected from the top interface, re-crosses the waveguide and is totally internally reflected from the bottom interface the total phase change is $2(2\alpha)\kappa - 2\phi$. Crucially, however, the total phase change the light undergoes over one whole trip must be an integer multiple of 2π. This is necessary to prevent destructive interference occurring when the light returns to its original position. If the phase change is not an integer multiple of 2π the wave will decay as it propagates [39]. This requirement can be expressed as:

$$2\alpha\kappa - 2\phi = \mathrm{m}2\pi, \tag{2.43}$$

where m takes integer values. A value of β which solves this equation ensures that constructive interference occurs when the light returns to its original position.

The allowed modes differ from each other with respect to their longitudinal propagation constant, and the transverse profile of their electric and magnetic fields. The modes are classified into different orders, defined by the number of times the transverse field switches sign within the core (the number of nodal points).

Slab waveguides are the type examined in this work. Here, the geometry only varies in one plane. The materials are considered to be uniform along the third axis, which is taken to extend to infinity. Two different polarisations of mode are available in slab waveguides: the Transverse Electric (TE), where an electric field vector points along the infinitely extended axis, and the Transverse Magnetic (TM), where it is the magnetic

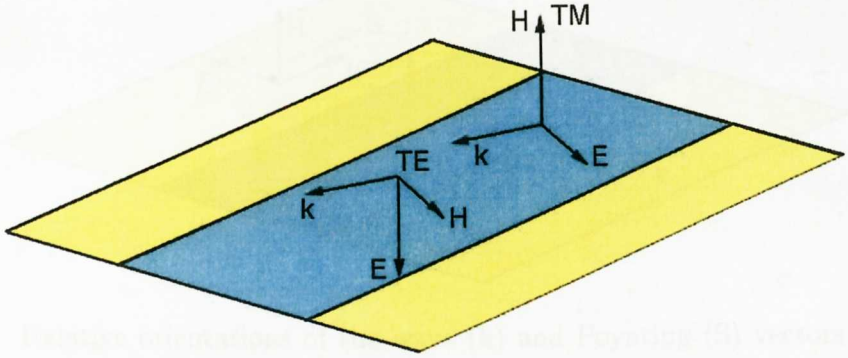

Figure 2.6: Field orientation in TE and TM modes within a 2D waveguide

field vector pointing in this direction, see figure 2.6.

Two different types of bound mode can exist in waveguides, surface and bulk. Both have exponentially decaying fields in the cladding, which is a requirement for them to be bound. However, bulk modes have an oscillating field within the core while surface modes have an evanescent field.

2.5.2 Negative refractive index (NRI) waveguides

After the discovery of the unusual optical properties of Negative Refractive Index (NRI) materials [18], theoretical work was conducted to investigate the effects that including such materials into waveguides would have on the waveguide's optical properties. It was found that these NRI waveguides have some different properties to conventional Positive Refractive Index (PRI) material waveguides. In this thesis it is the properties of these NRI waveguides which are examined.

The first key feature of NRI waveguides [16] is that they can support both TE and TM surface modes. The ability to support both TE and TM surface modes is due to the requirement that the sign of the permittivity and permeability be reversed in the core and cladding materials. For each polarisation, i.e. TE or TM, only one of the optical parameters need be reversed upon crossing the interface; the permeability for a TE mode and the permittivity for a TM [40]. The use of a NRI material is therefore not a strict requirement, and TM polarised surface modes can be excited on the surface of metals, which at some frequencies naturally have a negative permittivity [41]. However, to support a TE mode, a negative permeability is required for which an artificial material needs to be created.

Another key feature observed is that when a NRI material is used for the core, the fundamental mode (i.e. the mode with no nodal points) disappears. This is due to both

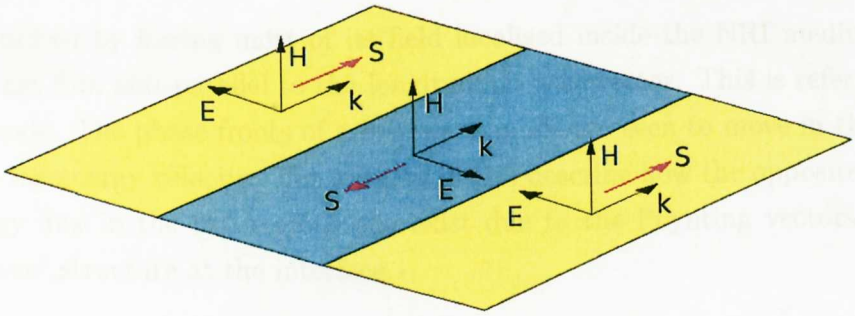

Figure 2.7: Relative orientations of the wave (k) and Poynting (S) vectors in the NRI core (blue) and PRI cladding (yellow) regions of the waveguide.

the phase change experienced by the mode as it crosses the core, and the phase change experienced by the mode when it undergoes total internal reflection, being negative. It is now impossible for the two sets of phase changes to cancel each other, which is the requirement for the generation of the fundamental mode [42]. The fact that symmetric waveguides containing a NRI core lack a fundamental mode must be borne in mind when it comes to classifying the modes [43]. In the classification system used in this work, the modes are defined by specifying firstly, if they are TE or TM; secondly, the number of nodes they have in the core region; and, lastly, whether they are forward or backward. Therefore, the TM backward mode with one nodal point is defined as TM_1^b. The mode which is examined the most in this thesis is the backward TM mode with two nodal points TM_2^b. Although not considered in this thesis, it should be noted that if the NRI material is used for the waveguide's substrate or cover, and a PRI material for the core, then under certain conditions the fundamental mode can also be supported [44].

It has also been discovered that mode degeneracy could occur in NRI waveguides. At a single frequency it is possible for modes, with the same number of nodal points but with different effective indices and transverse profiles, to exist. This feature is a key element in the trapped rainbow concept [17].

The most intriguing property of NRI waveguides, in the context of slow light, is that the direction of energy propagation is anti-parallel in the NRI core and the PRI cladding. This is a consequence of the requirement that the longitudinal wavevectors of a bound mode are parallel in both the core and cladding. Since, as shown earlier, in a NRI material the Poynting vector is anti-parallel to the wavevector, the Poynting vectors in the core and cladding point in opposite directions.

Degenerate modes highlight the effect of the reversal of the Poynting vector. One has most of its field in the PRI medium and, as a consequence, the net energy flux directed along the waveguide (obtained by integrating across the waveguide) is parallel to the mode's longitudinal wavevector. Such a mode is called a forward mode. The second

mode is identified by having most of its field localised inside the NRI medium and, as such, has a net flux anti-parallel to the longitudinal wavevector. This is referred to as a backward mode. The phase fronts of a backward mode are seen to move in the opposite direction to the energy velocity. The authors in [16] describe how the opposite directions of the energy flux in the two regions can exist due to the Poynting vectors forming a "double vortex" structure at the interface.

2.5.3 Trapped rainbow

By adjusting the transverse profile of a mode, the magnitude of the component of the net energy flux directed along the longitudinal axis of the waveguide can be altered. This means NRI waveguides have the potential to be used for slowing and even stopping light. This is a consequence of the fact that, in lossless situations, the energy velocity (ν_e) of a wave is defined by the Poynting vector $\mathbf{S}$ divided by the energy density W, and is equivalent to the group velocity ν_g [45]:

$$\nu_e = \frac{\mathbf{S}}{W}. \tag{2.44}$$

By altering the thickness of the waveguide core, the transverse profile of a mode can be re-shaped. Balancing the E- and H-field distribution in the core and cladding reduces the difference between the energy flux in the two regions. As the energy flux flows in opposite directions in the core and cladding regions, see figure 2.7, reducing the difference in the magnitudes causes the net energy flux along the waveguide to be decreased. A reduction in the net energy flux can be expressed as a reduction in the magnitude of the Poynting vector. Thus, via equation (2.44), the mode's energy and group velocities are reduced. At the critical point where the flux in the core is equal to that in the cladding, the light is predicted to be stopped [16]. This critical point is called the stopped light or the mode degeneracy point. Here, the dispersion curves for the forward and backward modes merge as their transverse field profiles become identical.

Even at the stopped light point the energy would still be confined inside the pulse. This is due to the double vortex structure formed by the Poynting vector [16, 46]. An adiabatic taper in the thickness of the core material has been suggested as a means of gradually altering the mode profile [46]. Making the taper adiabatic means the gradient is shallow enough to prevent the propagating mode from experiencing an abrupt change in core thickness, which would cause it to be reflected or to couple to other modes.

Numerical simulations have been conducted to test the ability of waveguides containing isotropic NRI materials to produce slow light. A waveguide geometry, where the

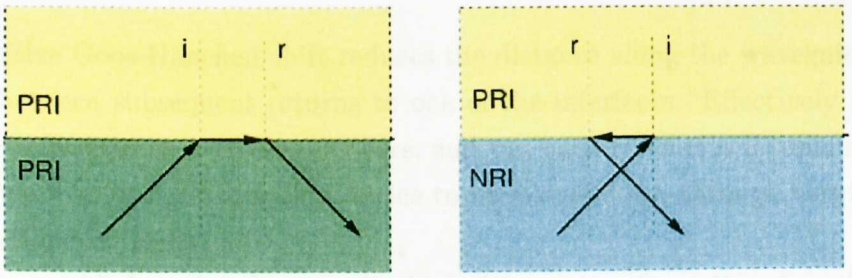

Figure 2.8: The difference in the Goos-Hänchen shift experienced by a ray at the interface between two positive refractive index materials and the interface between a negative and a positive refractive index material (when it is initially in the negative refractive index material). The shift is between the point on the interface where the beam is incident (i) upon and point on the interface where it is reflected from (r).

substrate was substituted for the NRI material rather than the core, was analysed [47]. The core thickness was varied in two different sections, this allowed the authors to show that the light propagated slower when the core was thinner and the distribution of the energy flux was more equal in the core and substrate.

Stopped light in NRI waveguides was first examined in detail in [17]. Here, a ray, rather than a field picture, is used to explain the effect. From the ray optics perspective, the slowing of light in a NRI waveguide is due to the negative lateral Goos-Hänchen shift experienced by a ray when undergoing total internal refraction at the core/cladding interface [42]. When total internal reflection occurs, the point the ray is reflected from is shifted from the point it is incident on the interface, see figure 2.8. This lateral shift is a consequence of the plane wave components which comprise the light beam, each undergoing a slightly different phase shift when they are totally internally reflected. This variation in the phase change occurs since each plane wave component is incident upon the interface at a slightly different angle [48]. At the interface between two conventional materials this shift is in the same direction as the light's longitudinal wavevector component β. However, for a ray of light incident from a NRI material onto an interface with a PRI material, the direction of this lateral shift is reversed. The direction of the shift is opposite to that of the light's longitudinal component as shown in figure 2.8.

As the light ray denotes power flow [17], the phase velocity must be in the same direction as the ray in the PRI cladding material. In the conventional double positive waveguide, the Goos-Hänchen shift is positive, so the propagation direction of the phase and the ray are the same. With a NRI waveguide, the relative directions of the phase and power flow depend on the magnitude of the Goos-Hänchen shift. When the shift is smaller than the propagation across the core, the phase and power flow are in opposite directions (backward mode), and when it is larger, they are in the same direction (forward

mode).

The negative Goos-Hänchen shift reduces the distance along the waveguide travelled by the ray between subsequent returns to one of the interfaces. Effectively it is taking two long steps forward as it crosses the core, and two back when it is internally reflected. Thus, it is possible for light in such a device to be slowed down through varying the size of the Goos-Hänchen shifts.

At the stopped light point the magnitude of the negative Goos-Hänchen shift is equal to the propagation across the core, meaning that the path of the ray has the shape of an hour glass or "optical clepsydra" [17], thus trapping or stopping the light.

The width of waveguide core at which light is stopped varies with frequency. Therefore in a structure with a tapered core different frequencies will be stopped at different points along it. This effect has been called the "trapped rainbow" [17], as a white light source would be separated into its constituent colours in such a structure.

The need for the taper to be adiabatic, first mentioned in [46], was discussed in [17]. Here, the authors show the calculation for the maximum allowable gradient for the waveguide's taper, which still prevents coupling between modes of different order. However, the authors do not mention the possibility of coupling between the two degeneracy modes when determining the parameters for the taper. Recently, this has started to be considered a large obstacle to the stopping of light via an adiabatic taper [49]. As the propagating mode approaches the degeneracy point, the authors in [49] show, through the use of mode coupling calculations between different sections of the taper, that an increasing amount of energy will couple between the two degenerate modes. Therefore, at the critical waveguide thickness the light will not be stopped, but rather it will couple into the degenerate mode propagating in the opposite direction, back along the waveguide. Increasing the length of the taper only serves to reduce the amount of energy lost by reflection, i.e. when a forward mode propagating to the right is transformed into a forward mode propagating to the left. Even if the length of the taper is increased, coupling between the two degenerate modes is still found. If a continuous wave is used, rather then a pulse, then this coupling into a mode propagating backwards creates an interference pattern, formed between the forward and backward propagating modes.

These investigations [49] indicate that using an adiabatic taper to achieve stopped light is not possible. However, drastically slowing light in a tapered waveguide would still be achievable.

Coupling to the NRI waveguide (and thus the tapered structure) was also examined in [17]. The conclusion is reached that, for a specific core thickness in a NRI waveguide, it is possible to have a mode with the same impedance and of the same order as a mode which exists in a conventional waveguide. If, for this core thickness, the transverse profile

of the mode in the NRI and PRI waveguides are similar, it should be possible to directly couple the two waveguides together with minimal reflection. However, once the mode has been coupled into the NRI waveguide, the NRI waveguide would still have to be tapered for the mode to approach the stopped light point.

A different coupling method has been proposed which not only allows light to be coupled into the NRI waveguide, but could also allow light to be stopped once inside. The prism coupling structure was proposed for use with NRI waveguides in [47], and examined in detail in [50]. The scheme involves placing a high refractive index material, the prism, alongside the NRI waveguide core, with a small gap between the two. A light beam, totally internally reflected from the inside of the prism, generates an evanescent field. This evanescent field extends into the core, allowing it to excite modes in the waveguide. The advantage of this setup is that it allows for the wavevector of the excited mode to be selected, through changing either the angle of incidence of the light in the prism or the refractive index of the prism. This means that either a forward or backward mode can be excited, even if, for the frequency of the light, the two are degenerate. This method could also allow the mode at the stopped light point to be excited. Provided that the correct parameters of the stopped light mode are excited, the mode should not propagate. This setup removes the need for an adiabatic taper [50], thus potentially reducing the length of the stop light device.

In addition to the use of bulk NRI materials to create the trapped rainbow structures, other materials and geometries have been investigated in the literature.

2.5.3.1 Anisotropic metamaterials

As mentioned in section 2.4.3, an anisotropic metamaterial composed of alternating layers of $\epsilon > 0$ and $\epsilon < 0$ is an alternative to bulk metamaterials in structures such as waveguides. The behaviour of certain polarisations of light in these structures is the same as that in waveguides containing an isotropic NRI material. In this type of anisotropic metamaterial the E-field should be orientated so that it crosses these layers. This causes the E-field to be reversed and, thus, the power flow in the anisotropic metamaterial is antiparallel to that in the PRI material. The trapped rainbow effect is, therefore, also theoretically feasible in devices containing anisotropic metamaterials since the degeneracy point, predicted in waveguides with bulk NRI materials, is present .

Investigations have been carried out into tapered anisotropic structures, i.e. structures designed to slow and stop different frequencies of light through changing the core width. In one case the properties of a waveguide consisting of an anisotropic material cladding and air core [51] were examined. The FDTD simulations of a continuous wave in this geometry show that the group velocity is slowed and the amplitude at the front of the

pulse increases as the wave travels down the taper. When a range of frequencies were injected, the lower frequencies were found to halt in wider core widths than the higher frequencies.

Interestingly, although the light pulse in the waveguide reaches a point where it can no longer propagate, it does not remain at this position. Almost instantly the pulse spreads out, back along the length of the waveguide through which it has just travelled. The authors attribute this behaviour to the pulse exciting a "backward-propagating forward-mode"; the forward mode injected into the waveguide is reflected when it reaches the stopped light point. For the light to be stopped they suggest a much longer taper is required which is adiabatic. However, an alternative interpretation could be that this reflection is evidence of coupling between the degenerate modes. If this is the case, as with a tapered waveguide containing a bulk NRI material [49], a tapered anisotropic waveguide would be unable to stop light.

2.5.3.2 Photonic crystal

Photonic crystals (PCs) can also be used to produce an antiparallel wavevector and energy flux along the propagation direction of a waveguide. This property means PCs could be used to produce the trapped rainbow effect. A PC waveguide containing a tapered core has been analysed [52]. Since the dispersion curve of a PC waveguide is different from that of a NRI waveguide (the dispersion curve for each mode dips rather than peaks), modes can propagate at small core widths, but are cut off when the core width is increased; the reverse of that found with NRI waveguides. Therefore, for the propagating mode to reach the stopped light point the width of the core needs to be increased and the light be injected into the thinner end of the waveguide.

In this tapered PC waveguide [52] a forward mode is observed to be compressed and stopped. The pulse does not remain at the stopped light point for long, but couples out of it, in a similar manner to that observed in the case of anisotropic waveguides [51]. However, instead of being reflected, it is suggested by the authors that the injected forward mode couples to the backward mode [52]. Given that at the degeneracy point the field profiles and optical properties of the two modes are identical, this seems a reasonable supposition. The authors' suggestion is given support by the fact that the backward-propagating mode is seen to radiate out of the waveguide when it reaches the core thickness corresponding to the cut off thickness of the backward mode.

When frequencies are injected into the waveguide individually, i.e. a CW is used, it is seen that they stop at different points along it. From the figures presented in [52] it is hard to determine, though, if any reflection occurs, since a CW is used.

In addition to tapering the width of the core material, the effect of varying the re-

fractive index of the PC waveguide has been examined [53]. This is mainly with regard to releasing trapped light pulses. Here, a pump pulse is injected into the waveguide first. Through non-linear carrier and optical Kerr effects this causes a change in the refractive index of the waveguide. This shifts the dispersion curve and thus changes the frequencies for which the stopped light point occurs in the waveguide. The signal pulse which follows the pump is thus stopped, with each frequency it is comprised of reaching its respective stopped light point somewhere along the tapered waveguide. Finally, a third control pulse can be sent through. This is designed to have the opposite effect on the waveguides' refractive index to that of the pump and thus releases the signal pulse.

2.5.3.3 Plasmonics

Plasmonic modes, also known as surface waves or slow modes, propagate along the interface between two different materials. For them to exist it is required that the sign of either the permittivity or permeability is reversed between the two materials. The geometry configurations usually studied are either dielectric-metal-dielectric (DMD) structures, or, the reverse, metal-dielectric-metal (MDM) structures. That the permittivity of the metal can be negative at some frequencies allows TM plasmonic modes to be supported, see section 2.5.2. If the core region is thin enough then the plasmonic modes propagating along the two interfaces can overlap and become a bound mode. These bound modes can either be symmetric or antisymmetric [16]. In symmetric modes the two plasmons are in phase and the transverse field has no nodal point in the core region. In antisymmetric modes a single nodal point is present in the core.

In a similar manner to bulk/oscillatory modes, dispersion curves of these plasmonic modes have been investigated [54]. It is shown that, in the lossless case, degeneracy points exist for both the symmetric and antisymmetric plasmonic modes in the MDM structure, but only for the symmetric mode in the DMD structure. Degeneracy points are found in Surface Plasmon Polariton (SPP) dispersion curves for certain material parameters. These points correspond to locations where the net longitudinal power flow along the core and cladding regions goes to zero and an energy vortex is created at the material interfaces. This shows, therefore, that the trapped rainbow effect can also be produced for plasmonic modes [55, 16].

Methods of reaching the degeneracy point are discussed in [54]. First, decreasing the reduced core width value (ak_0) is investigated. This value is the ratio between the core width and the wavelength of the light. Altering it thus changes either the width of the core or the operating frequency. However, the authors also suggest a second method. By, varying the permittivity of either the core or cladding material, the degeneracy point of the dispersion curve could be shifted to reach the frequency of the excited mode. Since

plasmonic and bulk modes have similar features this method could be applicable for bulk modes.

2.5.3.4 Spoof-Surface Plasmon Polaritons (Spoof-SPPs) on a metallic grating

Surface Plasmon Polaritons (SPPs) are created when light couples to a plasmon (an oscillation in the free electron density of a material). Both SPPs and plasmons travel along the interface between a metal and a dielectric, with evanescent fields extending into both. The term spoof is used to refer to SPPs which propagate along structured surfaces [56].

Structuring the surface allows added control over the properties of the SPP. If holes or grooves are fabricated in the metal, it is possible for the E-field to penetrate and excite modes in these air gap regions. SPPs are thus able to propagate along these structures. Provided these features are much smaller then the wavelength the metal can be assigned an effective permittivity.

Extensive investigations into the use of spoof SPP structures, with regard to creating a 'trapped rainbow'-like system, have been conducted by the group of Bartolli [57, 58, 59]. The specific structure studied here is an air/metal interface, with grooves cut into the metal. The spoof SPP dispersion curve of such a geometry varies with frequency, approaching the light line at lower frequencies and the plasma frequency at higher frequencies. As it tends towards the plasma frequency, the dispersion curve flattens out. It is this flat region of the dispersion curve that shows why such a structure could be used for slow light, since the group velocity is reduced as the dispersion curve's gradient flattens out.

The depth of the grooves in the metal affects the dispersion curve. The deeper the grooves, the lower the effective plasma frequency. This means that at deeper groove depths a given frequency is both slower (as the dispersion curve at that frequency becomes flatter) and more confined to the interface [59].

The momentum mismatch, which hinders coupling into the SPP mode, is minimised the greater the similarity between the dispersion curve of the grating structure and the light line. These are most similar at lower frequencies. However, it is the higher frequencies that experience the smallest group velocities since these frequencies are closest to the flatter region of the dispersion curve. To allow the same frequency to both couple into an SPP mode and be slowed, a tapered structure is introduced. The depth of the grooves is slowly increased at positions further away from the injection point. As long as the grooves are shallow enough (i.e. the excited frequency does not become greater than the surface's plasma frequency), SPP modes can exist within this structure [59].

This tapered structure has been tested in FDTD simulations [57]. These show that different frequencies are halted at different depths. The stopping points of the different frequencies are separated, since for different frequencies the flat point of the dispersion curve occurs at different groove depths. The higher the frequency, the shallower the groove depth at which the light is halted. This is similar to the effect predicted in [17], and allows the spatial separation of different frequencies of light.

The authors note that this structure would be able to operate at room temperature [57]. This is true for trapped rainbow structures in general. However the grating structure is found to be sensitive to small shifts in temperature due to the thermal expansion or contraction of the metal [57].

Although the FDTD simulations were carried out at THz frequencies [57], it was found that by reducing the dimensions of the grating, from μm to nm, it is possible to reduce the working wavelength to the telecommunication and visible domains [58]. Silver is used at these shorter wavelengths. In the visible regime, the intrinsic loss associated with the silver becomes significant and the stopped light point disappears.

The investigations of Bartolli's group were extended to examine if light which has been stopped could be released, provided loss is ignored [58]. Altering the dispersion curve of the structure was the method investigated. One way to do this is to cover the metal with a dielectric material. The thermo-electric effect could then be used to change the intrinsic permittivity of the dielectric, via adjusting the temperature. The effective permittivity of the whole structure and its dispersion curve would then be shifted. This, though, would be a relatively slow mechanism, limiting its usefulness.

Significantly, the spoof SPP grating structure has been investigated experimentally [60]. These experiments use visible light (500-700)nm. Two different experimental setups are employed. In one, the top (grooved) and the bottom (smooth) surface of the metal were used to form the two arms of a Mach-Zehnder interferometer. In the second, a tapered grating structure, such as that analysed previously, was used.

From the Mach-Zehnder interferometer setup, the interference pattern created between the light propagating along the top and bottom surfaces can be obtained. This enables both the group velocity and effective refractive index experienced on the grooved surface to be extracted. These experiments show, as would be expected, that the group velocity of the light propagating along a surface with deeper grooves is slower than that propagating along ones with shallower grooves.

The investigations using the tapered grating structure were found to produce the effects predicted computationally [58]. Red (low frequency) and green (higher frequency) light beams were coupled into the shallow grooved end of the taper. The red light was observed to propagate further along the taper than the green. Further evidence that the

structure was behaving as predicted was that, when both frequencies were coupled at the deep groove end, both were immediately scattered. This is a consequence of the plasma frequency of the material (when it contains grooves) being smaller than the frequency of both the red and green light.

This work shows that the grating structure has great potential, both for the sub-wavelength confinement and trapping of spoof SPPs. The experimental work conducted on these metal grating structures is one of the few occasions where the effects of the trapped rainbow have been practically demonstrated.

2.5.3.5 Clarricoats-Waldron waveguides

The Clarricoats-Waldron type waveguide has been known about since the 1960s [61]. It consists of a circular high dielectric material core separated from an outer metal layer by a region of air. Initially, the structure was of interest due to its ability to support backward modes [61]. Recently, however, this feature has been analysed in the context of the trapped rainbow effect.

The discontinuity of the dielectric material within the structure allows the creation of hybrid modes. These modes contain a mixture of two normal modes usually found in a circular metallic waveguide. The key aspect of these hybrid modes, which leads to the backward wave and the trapped rainbow, is that the magnetic field lines show a double vortex like structure at the interface between the high dielectric and the air [62]. As the E-field lines do not change direction when crossing this interface, equation (2.36) shows that the Poynting vector (and thus the energy flux) will be oppositely directed within the core and air regions.

As both NRI and Clarricoats-Waldron waveguides have oppositely directed energy flux in the core and surrounding material, optical effects predicted in NRI waveguides can also be observed in Clarricoats-Waldron waveguides. In fact the production of the trapped rainbow has been suggested in a Clarricoats-Waldron waveguide through reducing the width of the high dielectric core material [63]. Numerical simulations show that injected waves of different wavelengths are stopped at different points along this tapered core.

In addition to changing the width of the high dielectric core, an alternative method of altering the energy distribution of the mode has been investigated. In this new concept the permittivity of the core would be varied rather than its width [63]. This variation of permittivity, it is envisioned, could be done through heating one end of the waveguide, thus creating a temperature gradient. Since the permittivity of a material is temperature dependent, a gradual variation in the dielectric constant should be produced.

Simulations of this structure using frequencies in approximately the THz regime and realistic material parameters (i.e. GaAs for the dielectric core) were conducted. It is

found that slow modes can be produced and that field magnitudes are enhanced as the group velocity is reduced. However, the authors, referring to [64], claim that when losses are included the mode can no longer be brought to a complete halt. They suggest that this loss could be mitigated, or even that the wave could be amplified by replacing the high dielectric material of the core with a gain material.

The Clarricoats-Waldron waveguide, therefore, looks like a promising candidate for slow or even potentially stopped light applications. However, so far only its operation at wavelengths in the millimeter range has been investigated, whereas many of the potential applications for stopped light structures are in the telecommunication or even visible regimes.

2.5.4 Trapped rainbow and dissipative loss

If material loss is taken into account, the existence of a stopped light point, as predicted for example in [16, 46, 17], has been questioned [64, 44]. With loss included the dispersion curves of the forward and backward modes fail to combine, thus removing the degeneracy (stopped light) point [64, 44]. The significance of this analysis is covered in this thesis.

Interestingly, the disappearance of the degeneracy point only occurs if the loss in the waveguide is included as spatial loss [65]. This assumption is made if the loss is represented through a complex wavevector. If the loss is represented as temporal loss, a complex frequency, then the degeneracy point remains. The reason for this is that if the loss is represented as spatial loss then the magnitude of the group velocity of the pulse has an effect (if it takes longer for the pulse to travel between two different points in space, then it will register as a greater spatial loss) [66]. However, the temporal loss is unaffected by the group velocity. For this reason the temporal and spatial losses are related through the group velocity of the wave [66].

Even if loss is included via a complex wavevector the degeneracy point can be restored if a gain material is incorporated into the structure [37]. This has been shown by placing a gain material in the core region of a waveguide comprising an air core and anisotropic metamaterial cladding. The fields of the bulk modes are most intense in the core region, which allows the most efficient coupling between the gain material and the propagating field.

Complete loss compensation using a gain material has also been shown for coupled SPP propagation in conventional materials [67]. Again, the gain material is placed in the core where the highest field intensities are. However, it is also found that, if the gain material is located in the cladding region where the evanescent fields could be weaker, the mode could be pumped [68]. When examining the propagation of a bound SPP mode along a metal slab it is found that the loss experienced by the mode is reduced as the

thickness of the metal slab is decreased (as a consequence of there being less overlap between the mode and the dissipative metal). The effect of varying both the thickness of the gain material, and its distance away from the metal strip along which the SPP propagates, is also examined [68]. It is found that the gain felt by the propagating mode decreases with increasing distance between the metal and gain strips and with decreasing thickness of the gain strip.

Though extremely interesting, most of the previous works examining loss compensation in NRI waveguides examine only a single frequency. Little has been done regarding loss compensation with respect to the pulse as a whole. Examining the effect of the dispersion of both the gain and NRI materials would be a step towards a more realistic description of the optical properties of pumped NRI waveguides. Another area of interest would be to examine the possibility of pumping a waveguide containing a bulk NRI material through the introduction of the gain in the cladding material, in a similar manner to that done in [68].

2.6 Summary and areas to investigate

Negative refractive index materials, have interesting optical properties, such as negative refraction and the opposite direction of the wave and Poynting vectors. Recently, work in the field of metamaterials has allowed materials with these novel properties to be experimentally realised. These metamaterials are composed of subwavelength components, which interact more strongly with the electric and magnetic fields of a propagating EM wave than conventional materials. The first metamaterials created operated in the microwave regime and over the last decade the dimensions of the metamaterial components have been reduced, allowing them to operate at progressively higher frequencies. Negative refraction has now been shown at the telecommunication and optical bandwidths, regions of the electromagnetic spectrum in which the properties of NRI materials are expected to be of most use.

In parallel with the development of NRI materials, potential uses of these materials have been examined. One branch of this work has focused on the effects of inserting NRI materials into waveguides. It has been discovered that waveguides containing NRI materials have optical properties that differ from those of conventional waveguides, such as the ability to support both TE and TM plasmonic modes. The trapped rainbow effect is another feature NRI waveguides are envisioned to have. This effect is a consequence of the reversal of the power flow in the NRI and PRI regions of the waveguide. Through this effect, light it is predicted, could be slowed significantly and potentially even stopped.

Although the use of NRI waveguides for slowing light has been examined using analytic

methods, there is still a need for further investigation of their properties using computational techniques. An example of the area which would benefit from more in depth investigation would be a check of the effective index experienced by modes propagating in NRI waveguides of different core widths. Another feature of NRI waveguides which has not yet been investigated is the use of a varying core refractive index to reduce the group velocity of a propagating pulse.

A key draw-back with all metamaterials created so far is their high intrinsic loss. This will cause the propagating light to experience a decrease in amplitude. Simulations of NRI waveguides containing gain have been conducted, which mitigate and even eliminate the loss experienced by the light. These simulations, though, focus mainly on a single frequency. Work examining the effect on each frequency present in the pulse, and on the total energy of a propagating pulse, could be of use.

Finally, although a NRI waveguide has the potential to enable the slowing down of light, there is doubt as to whether in its tapered configuration it could be used to completely stop light pulses. Recent work claims that the coupling between the degenerate modes would prevent light from remaining at the critical core thickness. This explanation seems to be supported by results of previous computational simulations of tapered waveguide structures, which show the light immediately propagating back away from the stopped light point once it arrives there. This difficulty with the tapered structure motivates a more in-depth examination of the prism coupling method. This method allows coupling straight to the mode at the stopped light point and therefore should not be susceptible to coupling between degenerate modes since the core thickness can be kept constant. Therefore light coupled to the stopped light point should remain stationary, rather than move away as predicted in tapered waveguides.

Simulations have been used extensively to investigate both NRI materials and NRI waveguides. A key reason for this is that, at present, a waveguide containing a NRI isotropic material has not been created experimentally. Simulations are therefore the only ways to test the properties of NRI waveguides predicted by analytic theory. Examining the macroscopic properties of NRI materials and devices is especially suited to computational modelling since these properties can be described using bulk parameters. This is possible since the structures comprising metamaterials are subwavelength in size and so do not need to be modelled individually. This reduces the computing resources required and allows larger geometries to be examined than would otherwise be the case. By analysing the output of the simulation it is possible to extract the complex frequency and complex wavevector parameters. The use of the computational simulation method also allows the effects of varying different aspects of the geometry to be easily tested.

In the next chapter, the specific computational method used to investigate the prop-

erties of NRI waveguides is detailed and its ability to model NRI materials is tested.

Chapter 3

Computational techniques and methods

3.1 Introduction

As described in the previous section Negative Refractive Index (NRI) materials are still in their infancy, at least for the visible regime. This means that investigation into devices and structures using these materials has to be conducted either analytically or using computer simulations.

A popular simulation method is Finite-Difference Time-Domain (FDTD) computation. This method is particularly useful in investigating NRI materials since it "solves Maxwell's equations directly, without any assumption of the sign of the refractive index or direction of wave propagation inside the LHM slab" (Note LHM revers to Left Handed Materials) [69]. It has been used in many studies of NRI materials and waveguides containing them [47, 52, 51, 70]. The FDTD method is used to conduct the simulations presented in this thesis.

A description of the basic features of the FDTD method is provided in appendix 8.1. In this appendix the adaption of Ampere's and Faraday's equations into forms suited to the FDTD method is given and the use of these equations in the FDTD method is detailed. The appendix goes on to give the meaning of terms such as the Courant value and resolution in the context of the FDTD method.

This current chapter provides a description of the more non-standard aspects of the FDTD method required in this thesis. This includes details of how both the NRI and gain materials are modelled in the group's FDTD code. An outline is also given of the method used to extract the refractive index of light propagating in the simulation (the effective refractive index in the case of waveguides). Finally, tests of both the NRI material model and parameter extraction method are conducted by comparing the refractive index of the NRI obtained from the simulation with analytic predictions.

3.2 Implementing materials

The effect of materials on the propagating EM wave is incorporated into Ampere's and Faraday's equations through the polarisation and magnetisation of the materials:

$$\nabla \times \mathbf{H} = \epsilon_0 \frac{\partial \mathbf{E}}{\partial t} + \mathbf{j}, \tag{3.1}$$

$$\nabla \times \mathbf{E} = -\mu_0 \frac{\partial \mathbf{H}}{\partial t} - \mu_0 \frac{\partial \mathbf{M}}{\partial t} \tag{3.2}$$

In equation (3.1) the polarisation is included via the current density $\mathbf{j}$, where $\mathbf{j} = \partial \mathbf{P}/\partial t$.

To simulate the response of the materials, the behaviour of the polarisation and magnetisation need to be modelled. This is accomplished through the use of material equations. These equations relate the material's polarisation and magnetisation to the incident E- and H-fields. Incorporating the material response into the FDTD simulation in this way is called the Auxiliary Differential Equation (ADE) method since the behaviour of the polarisation and magnetisation are given through differential equations. This method allows the dispersive characteristics of the material to be modelled, i.e. the variation in its response with frequency. Dispersionless materials can be modelled by simply setting the current density and magnetisation to 0 and varying the free space permittivity and permeability. However, in NRI materials, modelling the dispersion is found to be a crucial requirement as it removes the potential problem of the material parameters averaging to zero; for instance, at the interface between mediums with refractive indices of 1 and -1 [69]. That the NRI material be dispersive is also required to ensure that the energy density of the material remains positive when an EM-wave propagates through it [18].

Two different material models are used in this thesis, the Drude and Lorentz. These are described in the sections below as is the method used to incorporate them into the FDTD model.

3.3 Drude model

The response of the NRI material is modelled using a Drude model. This model was developed by P. Drude to describe the properties of metals [71]. It is a relatively simple model which assumes that the free electrons within a metal can be described using a kinetic theory, which had previously been used to look at gases. In this model electrons

are treated as particles. The only interaction mechanisms considered are their collisions with other electrons and positive ions. Between these collisions they are assumed not to interact. After a collision the velocity of each electron is taken to be random and the change in momentum each undergoes between collisions to be due to the effect of the E-field.

Given these assumptions, and defining such concepts as the relaxation time (τ) as the average time between collisions, it is possible to derive a material equation for the free electrons within the material expressed in terms of the displacement:

$$m\frac{\partial^2 \mathbf{x}}{\partial t^2} + \frac{m}{\tau}\frac{\partial \mathbf{x}}{\partial t} = e\mathbf{E}, \tag{3.3}$$

where m is the effective mass of the electron and $\mathbf{E}$ is the driving electric field. This equation can be expressed in the frequency domain as:

$$-m\omega^2\mathbf{x} - i\Gamma_e m\omega\mathbf{x} = e\mathbf{E}, \tag{3.4}$$

where $\Gamma_e = 1/\tau$ is the collision frequency. The displacement of the electrons as a function of frequency is thus:

$$\mathbf{x} = -\frac{e}{m}(\omega^2 + i\Gamma_e\omega)^{-1}\mathbf{E}. \tag{3.5}$$

The polarisation of the material can be found from this equation as $\mathbf{P} = -Ne\mathbf{x}$ where N is the density of electrons. This gives:

$$\mathbf{P} = -Ne\mathbf{x} = \frac{e^2 N}{m}(\omega^2 + i\Gamma_e\omega)^{-1}\mathbf{E}. \tag{3.6}$$

As $\chi = \mathbf{P}/\epsilon_0\mathbf{E}$ we find that:

$$\chi = \frac{e^2 N}{\epsilon_0 m}(\omega^2 + i\Gamma_e\omega)^{-1}, \tag{3.7}$$

and as $\epsilon_r = 1 + \chi$ we can derive the frequency response of the Drude material's permittivity as:

$$\epsilon = 1 + \frac{e^2 N}{\epsilon_0 m}(\omega^2 + i\Gamma_e \omega)^{-1}, \tag{3.8}$$

where the term $\frac{e^2 N}{\epsilon_0 m} = \omega_p^2$ is defined as the plasma frequency [22], this allows the known frequency dependance of the permittivity to be obtained [71]:

$$\epsilon = 1 + \frac{\omega_p^2}{\omega^2 + i\Gamma\omega}. \tag{3.9}$$

The Drude equation can be found by subsituting $\mathbf{x} = \frac{\mathbf{P}}{Ne}$ and $\frac{e^2 N}{\epsilon_0 m} = \omega_p^2$ into equation (3.3) to give:

$$\frac{\partial^2 \mathbf{P}}{\partial t^2} + \Gamma_e \frac{\partial \mathbf{P}}{\partial t} = \epsilon_0 \omega_p \mathbf{E}. \tag{3.10}$$

The Drude equation is included into the FDTD simulation by expressing it in terms of the current density $\mathbf{j} = \frac{\partial \mathbf{P}}{\partial t}$. This means equation (3.10) can be expressed as:

$$\frac{\partial \mathbf{j}}{\partial t} + \Gamma_e \mathbf{j} = \epsilon_0 \omega_p^2 \mathbf{E}, \tag{3.11}$$

where the plasma frequency ω_p, is as defined earlier.

As with Maxwell's equations in appendix 8.1, this equation needs to be discretised before it can be used in the FDTD system. Since the E-field is calculated at integer steps, see appendix 8.1, equation (3.11) is also evaluated at integer steps.

In equation (3.11) the differential of the current density appears. To calculate this differential requires the value of the current density at the half steps before and after the time step at which the differential is used. If the magnitude of the current density is found at integer steps, i.e. in the same step as the differential is required, then to obtain the differential it is necessary to average the current density to obtain the values at each half-integer time step, see figure 3.1. These values are then used to obtain the differential. If, however, the current density is initially calculated at half-integer time steps this removes the need for averaging which increases the accuracy of the derivative. A drawback with calculating the current density at half-integer time steps is that averaging is now necessary to find the second term in equation (3.11). However, since this term is smaller than the first, more accurate results are obtained if this is the term that is averaged.

The current density components are calculated at the same points in the Yee cell as

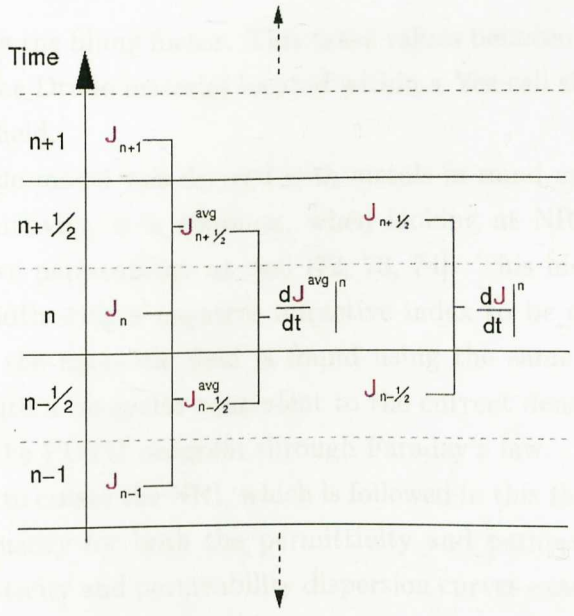

Figure 3.1: The two different methods for calculating the derivative of the current density at integer time steps.

their E-field counterparts (in turn the magnetisation and H-field values are also located together). In a similar manner to equations (8.3), (8.8) and (8.9), equation (3.11) can be discretised, thus:

$$\frac{\mathbf{j}^{n+\frac{1}{2}} - \mathbf{j}^{n-\frac{1}{2}}}{\Delta t} + \Gamma_e \left(\frac{\mathbf{j}^{n+\frac{1}{2}} + \mathbf{j}^{n-\frac{1}{2}}}{2} \right) = \epsilon_0 \omega_p^2 \mathbf{E}^n. \tag{3.12}$$

As with equations (8.4), (8.10) and (8.11), with some manipulation this equation can be rearranged to allow the current density in the next time step to be calculated:

$$\mathbf{j}^{n+\frac{1}{2}} = \left(\frac{2 - \Gamma_e \Delta t}{2 + \Gamma_e \Delta t} \right) \mathbf{j}^{n-\frac{1}{2}} + \left(\frac{2\Delta t}{2 + \Gamma_e \Delta t} \right) \epsilon_0 \omega_p^2 \mathbf{E}^n. \tag{3.13}$$

This equation for the current density can be included into the calculation of the E field by using Ampere's equation, equation (3.1). For instance adding the current density into equation (8.11) produces:

$$\mathrm{E}^{n+1}_{x(i+1,j+\frac{1}{2})} = \mathrm{E}^{n}_{x(i+1,j+\frac{1}{2})} + \frac{\Delta t}{\epsilon} \left[\frac{\mathrm{H}^{n+\frac{1}{2}}_{z(i+1,j+2)} - \mathrm{H}^{n+\frac{1}{2}}_{z(i+1,j)}}{\Delta y} \right] + \frac{\Delta t}{\epsilon} w(i,j,k) \mathrm{j}^{n+\frac{1}{2}}_{x(i+1,j+\frac{1}{2})} \tag{3.14}$$

where the term w is the filling factor. This takes values between 0 and 1, and depends on the proportion of the Drude material located within a Yee cell sized cube surrounding the position of the E-field.

Although the Drude model was derived with metals in mind and thus only intended to apply to the permittivity, it is common, when looking at NRI materials, to use it to produce a dispersive permeability as well [72, 73, 74]. This method is popular as it allows a large bandwidth with a negative refractive index to be created. The effect of the NRI material on the magnetic field is found using the same material equation as equation (3.11) but with a magnetic equivalent to the current density. This variable can be incorporated into the FDTD program through Faraday's law.

The usual method to create the NRI, which is followed in this thesis, is to use identical values of plasma frequency for both the permittivity and permeability response. This means that the permittivity and permeability dispersion curves exactly overlay each other providing the widest possible region of NRI.

3.4 Lorentz model

The other material model used is the Lorentz model. This allows gain materials (materials that supply energy to the system) to be modelled. This is possible since the Lorentz model produces the basic shape of a two level system [75, 76] and can be taken as describing an inverted system (with the population of carriers in the higher energy level being greater than that in the lower level) [77]. Carriers moving from a higher energy level to a lower energy level of this inverted system thus supply energy to the EM field. However, the Lorentz model does not take into account the change in carrier population of the two levels. Thus it can be taken as only applying in the gain material's linear regime and cannot be used to probe non-linear effects.

The Lorentz model's material equation, equation (3.15), is equivalent to equation (3.11) for the Drude and calculates the material's polarisation:

$$\frac{\partial^2 \mathbf{P}}{\partial t^2} + 2\Gamma_e \frac{\partial \mathbf{P}}{\partial t} + \omega_p^2 \mathbf{P} = \epsilon_0 \Delta\epsilon \omega_p^2 \mathbf{E}, \tag{3.15}$$

where $\Delta\epsilon$ is the net change in permittivity between frequencies on either side of the Lorentz resonance [78]. Equation (3.15) can be incorporated into Ampere's law through equation (3.16):

$$\nabla \times \mathbf{H} = \epsilon_0 \frac{\partial \mathbf{E}}{\partial t} + \frac{\partial \mathbf{P}}{\partial t}. \tag{3.16}$$

Using the relation between the current density and polarisation, $\mathbf{j} = \partial \mathbf{P}/\partial t$, it can be seen that equation (3.15) is very similar to equation (3.11). The added term on the left hand side represents a restoring force, meaning that the Lorentz model can be used to model electrons bound within atoms in the material instead of only the free electrons which the Drude model simulates. Unlike the current density, the polarisation is calculated at integer time steps (i.e. at the same time as the E-field) since this allows the second order term to be discretised without the need for averaging. The differential at $n+\frac{1}{2}$ and $n-\frac{1}{2}$ are found by taking the difference of $\mathbf{P}^{n+1}$,$\mathbf{P}^{n}$ and $\mathbf{P}^{n}$,$\mathbf{P}^{n-1}$ respectively and dividing by the time step. The difference between these two differentials is then divided by the time step to obtain the second order differential. Using the other discretisation methods shown in appendix 8.1, and through manipulation, an equation is obtained allowing the polarisation at the next time step to be found:

$$\mathbf{P}^{n+1} = \left[\frac{2-\omega_p^2\Delta t^2}{1+\Delta t\Gamma_e}\right]\mathbf{P}^{n} + \left[\frac{-1+\Gamma_e\Delta t}{1+\Delta t\Gamma_e}\right]\mathbf{P}^{n-1} + \frac{\epsilon_0\Delta\epsilon\omega_p^2\Delta t^2}{1+\Delta t\Gamma_e}\mathbf{E}^{n}. \tag{3.17}$$

The polarisation found using this equation can then be subsituted into equation (3.16).

3.5 Extraction of refractive index (complex - wavevector)

One of the most important parameters which will be extracted from the simulations is the refractive index (or, in the case of a mode in a waveguide, the effective refractive index). Since this functionality was not built into the group's FDTD code it has been implemented specifically for this work. The method used is described in [70] and [78].

Two points are used, positioned along the propagation direction of the wave, which in a waveguide is along the longitudinal axis of the core. The value of either a E or H-field component is recorded at both points at each time step. The time signal of the field at the two points is thus obtained. Both of these signals are then Fourier transformed giving the amplitude and phase of each frequency present in the signal (since in the FDTD method time is discretised, a discrete number of frequency components are extracted from this Fourier transform with the separation between the frequencies found to be dependent on the duration of the signal).

By placing the two spatial points close together the frequency dependence of the refractive index can be calculated by finding the phase difference between the two points for each frequency. Similarly the imaginary part of the refractive index can be found by examining the change in the amplitude of each frequency. It is important that the recording points are close together (their separation smaller than the wavelength of each frequency excited in the material) so as to remove any ambiguity in the phase difference found. Since only the phase is obtained, a complete wavelength between the points would not be accounted for and the phase change calculated would be a factor of 2π out. If we take the time dependence used in the Fourier transform as being $e^{-i\omega t}$, then using the shift method [79] the relation between the two points is given by equation (3.18):

$$F(\omega, x_2) = e^{ikd} F(\omega, x_1). \tag{3.18}$$

Here $F(\omega, x_2)$ and $F(\omega, x_1)$ are the Fourier transforms of the time signals at points x_2 and x_1 respectively. Point x_2 is further from the source (and thus the origin of the x-axis) than x_1 . Therefore $x_2 > x_1$. As mentioned previously the Fourier transform at both points gives an amplitude and a phase so equation (3.18) can be rewritten as:

$$A_2 e^{i\phi_2} = e^{ikd} A_1 e^{i\phi_1}, \tag{3.19}$$

with A_2 and A_1 being the amplitude at points 2 and 1, respectively, and ϕ_2 and ϕ_1 being the phase at points 2 and 1, respectively. If k is expanded into its real and imaginary values $k = \beta + i\alpha$, where β is the longitudinal propagation constant ($\mathrm{Re}(n)k_0$) and α the decay constant ($\mathrm{Im}(n)k_0$). This relation can be substituted into (3.19) allowing both β and α to be found:

$$\ln(A_2) + i\phi_2 = ikd + \ln(A_1) + i\phi_1, \tag{3.20}$$

$$\ln(A_2) + i\phi_2 = i(\beta + i\alpha)d + \ln(A_1) + i\phi_1, \tag{3.21}$$

$$\ln(A_2) + i\phi_2 = i\beta d - \alpha d + \ln(A_1) + i\phi_1. \tag{3.22}$$

Separating the real and imaginary terms gives:

$$\ln(A_2) - \ln(A_1) = -\alpha d, \tag{3.23}$$

$$\frac{1}{d}\ln\left(\frac{A_1}{A_2}\right) = \alpha, \tag{3.24}$$

$$\frac{1}{k_0 d}\ln\left(\frac{A_1}{A_2}\right) = \mathrm{Im(n)}, \tag{3.25}$$

and

$$i\phi_2 = i\beta d + i\phi_1, \tag{3.26}$$

$$\frac{(\phi_2 - \phi_1)}{d} = \beta, \tag{3.27}$$

$$\frac{(\phi_2 - \phi_1)}{k_0 d} = \mathrm{Re(n)}. \tag{3.28}$$

Thus equations (3.25) and (3.28) show how both the real and imaginary parts of the refractive index are extracted from the simulation.

3.6 Material parameters test

To test the material models present in the group's FDTD code (which had been implemented by a different member of the group) a test simulation was conducted. This simulation consisted of a 1D geometry with a length of NRI material positioned between two regions of conventional material.

The refractive index experienced by the propagating wave in the NRI material was extracted using the method described in section 3.5 and then compared against an analytical calculation of the NRI material's dispersive refractive index.

The analytical refractive index of the NRI material was arrived at through substituting $\mathbf{j} = \partial\mathbf{P}/\partial t$ into equation (3.11) to produce:

$$\frac{\partial^2 \mathbf{P}}{\partial t^2} + \Gamma_e \frac{\partial \mathbf{P}}{\partial t} = \epsilon_0 \omega_p^2 \mathbf{E}. \tag{3.29}$$

By making the substitutions $\mathbf{P} = \mathbf{P}e^{-i\omega t}$ and $\mathbf{E} = \mathbf{E}e^{-i\omega t}$ and then differentiating, equation (3.29) is transformed into:

$$-\omega^2\mathbf{P} - i\Gamma_e\omega\mathbf{P} = \epsilon_0\omega_p^2\mathbf{E}, \tag{3.30}$$

$$\mathbf{P} = -\frac{\epsilon_0\omega_p^2}{\omega^2 + i\Gamma_e\omega}\mathbf{E}. \tag{3.31}$$

By comparing equation (3.31) with (2.8) the value of the electric susceptibility can be extracted and substituted in the equation for the material's relative permittivity ($\epsilon_r = 1 + \chi_e$). This leads to the materials permittivity being given by:

$$\epsilon_r = 1 - \frac{\omega_p^2}{\omega^2 + i\Gamma_e\omega}. \tag{3.32}$$

As mentioned in section 3.3 the magnetic response of the NRI material is incorporated using an identical equation to that of the electric response. This means that the equation for the relative permeability of the NRI material is the same as (3.32) with μ_r substituted for ϵ_r. In all of the simulations conducted in this work the plasma frequencies used to define the permittivity and permeability of the NRI material are identical, as are the collision frequencies. Since the relationship between the permittivity, permeability and refractive index is given by $n = \sqrt{\epsilon_r\mu_r}$, the refractive index of the NRI material is also given by (3.32).

Writing the refractive index of the NRI material in terms of its real and imaginary components gives:

$$\mathrm{Re(n}(\omega)) = 1 - \frac{\omega_p^2}{\omega^2 + \Gamma^2}, \tag{3.33}$$

$$\mathrm{Im(n}(\omega)) = \frac{\omega_p^2\Gamma}{\omega^3 + \omega\Gamma}. \tag{3.34}$$

The refractive index of the conventional material in the test simulation is set to 1. The plasma frequency required for the NRI material to have a refractive index of -1 at the central frequency (ω) is determined through rearranging equation (3.33) to get:

$$\omega_p = \sqrt{(1 - \mathrm{Re(n)})(\omega^2 + \Gamma^2)}. \tag{3.35}$$

In this initial simulation the NRI material is modelled as being lossless ($\Gamma = 0$).

A Constant Wave (CW) pulse (one with an infinite sustain) was used. Once the wave had built up to its maximum amplitude and had propagated through the whole geometry,

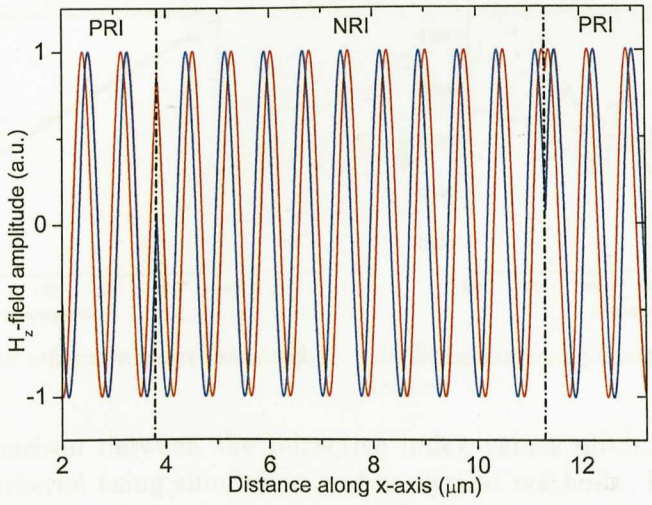

Figure 3.2: Snapshot of H_z-field component along the simulation geometry. Snapshot 2 (Blue) is taken 4.0fs after snapshot 1 (Red).

snap shots of the H_z-field component were taken. Two of the snapshots taken are shown in figure 3.2. The source is located on the left with the wave propagating to the right. As can be seen in the PRI material the phase fronts move away from the source (since in the later snap-shot they have moved to the right). However, in the NRI material the phase fronts move to the left during the time interval. This negative phase velocity is also observed in [70] and is expected in a NRI material and gives confidence that the implementation of the NRI material in the group's FDTD code is correct.

Next the refractive index extraction method was tested. To provide a more comprehensive test the NRI material was defined as having a small amount of loss, meaning the imaginary part of its refractive index would be non zero. The loss was kept small (the refractive index of the NRI material at the source's central frequency was -1+0.001i) to minimise the effect of the impedance mismatch between the lossy NRI material and the loss-less PRI material. This also reduces any reflection from the material interfaces. A pulse was used instead of a constant wave, thus testing the ability of the extraction method to find the NRI material's dispersive refractive index over a wide bandwidth.

The results are shown in figure 3.3. The measurement points are placed in the NRI material and reassuringly record it as having a refractive index of -1 at the central frequency (400 THz), figure 3.3a. The real part of the NRI material's refractive index extracted from the simulation (the points), are identical to that predicted using equation (3.33) (the line) over the central frequencies. Only at the highest and lowest frequencies is a discrepancy found due to the failure of these frequencies to be excited by the pulse.

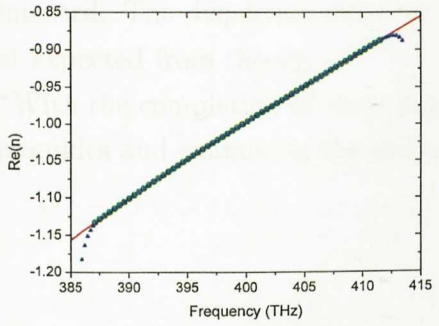

(a) Real component of refractive index extracted

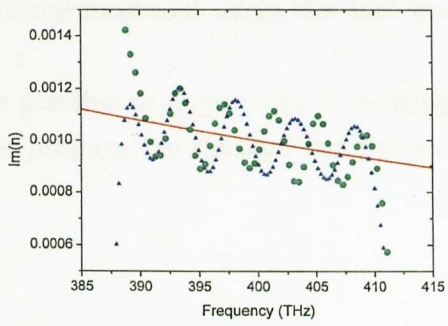

(b) Imaginary component of refractive index extracted

Figure 3.3: Comparison between the refractive index values obtained for the negative refractive index material using simulation and analytical methods. Red line - analytical calculation, Green circles - simulation results, Blue triangles- simulation results with shorter length of NRI material.

The imaginary component of the refractive index extracted is shown in figure 3.3b. The points obtained are in broad agreement with theoretical prediction, equation (3.34). However the values extracted oscillate around those predicted by theory. This oscillation is taken to be due to the fact that, in additon to the initial pulse, the pulse partially reflected from the interface is also being recorded. This partial reflection would occur due to the slight mismatch in the refractive index of the NRI and conventional material, since the NRI material is now modelled as being dispersive while the conventional material is simulated as having a refractive index of 1 at each frequency. To test if this is the cause, the length of the NRI material was shortened so that a different interference pattern would occur at the measurement points. As can be seen in figure 3.3b, changing the NRI material length does change the frequency of the oscillation. The large dip and rise in the real part of the effective refractive index at the highest and lowest frequencies in figure 3.3b are, as with the real part of the refractive index, due to these frequencies not being excited by the pulse.

3.7 Summary and conclusion

So, to summarise, the FDTD method is a well established method to explore the electrodynamics of different structures and materials. It has been used in previous work to successfully model the properties of NRI materials. The NRI material model used in this thesis, a double Drude model, has been tested and the results obtained are consistent with those expected.

In addition a complex-wavevector, refractive index extraction method has been implemented. The dispersion curve of the NRI material produced using this tool matches that expected from theory.

With the completion of these initial tests it is possible to move on to simulating NRI waveguides and examining the properties of pulse propagation through these structures.

Chapter 4

Pulse propagation

4.1 Introduction

This chapter details the investigation into pulse propagation through waveguides containing a lossless NRI material core. This investigation tests the predicted properties of the trapped rainbow concept and examines the effects of varying the refractive index of the waveguide core.

Initially, a description of the waveguide geometry is given, detailing the materials implemented, the layout and the type of simulation boundaries set. The method used to excite specific waveguide modes is then outlined. For this injection scheme the transverse profile of the desired mode is required. This is calculated using the mode's dispersion curve, the derivation for which is detailed. Following this analytic work, the effect on the simulation results of variations in both the geometry and numerical parameters is assessed. This allows the effect of these parameters to be reduced, adding confidence to the simulation results.

Following the preliminary setup, the potential use of NRI waveguides for slowing light is examined. The simulation results are compared against those obtained through analytic methods allowing both schemes to be verified. The first set of simulations examine the effect of varying the core thickness, as proposed in [17]. Following this, a different slowing method is also investigated. Here, the refractive index of the core, rather than its thickness, is reduced.

4.2 Simulation setup

The geometry used in these simulations is shown in figure 4.1.

The double Drude model is used for the core and a conventional PRI dispersionless material for the cladding. Since only symmetric modes are investigated, the size of the

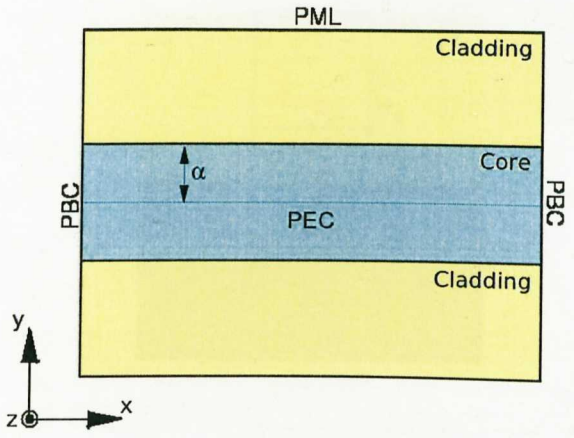

Figure 4.1: Waveguide geometry used in simulations investigating pulse propagation. NRI material core (blue), PRI material cladding (yellow).

geometry can be reduced (and the simulation run time shortened) by including a mirror boundary along the central axis of the waveguide. As a result, only half of the waveguide need be modelled. The mirror boundary is a Perfect Electric Conductor (PEC). The PEC is used to model cases where the H-field components, orientated parallel to a boundary, have the same sign on both sides (as is the case for the H-field component along the central axis of the waveguide for the symmetric TM modes examined here). The PEC boundary reverses the E-field components which are parallel to the interface. This, again, is correct for a TM mode [78].

A Perfectly Matched Layer (PML) is used for the top boundary, which is placed at the largest y-axis value and runs parallel to the central axis. The PML is meant to be a perfect absorber, preventing any wave incident upon it from being reflected back into the simulation domain. This property means that the simulation domain should behave as if it extends to infinity in the positive y direction. In practice, however, the PML does not work perfectly, especially for fields which enter it at very shallow angles.

The simulation geometry is terminated at both ends of the x-axis by boundaries with Periodic Boundary Conditions (PBC). These two boundaries are linked, so that any field which exits the domain via one will re-enter (in the next time step) through the other.

The material boundaries in the simulation domain run through the centre of the Yee cells. This means that for the TM mode which contains the field components H_z, E_x and E_y, only the E_x component need be averaged. This is due to the fact that field

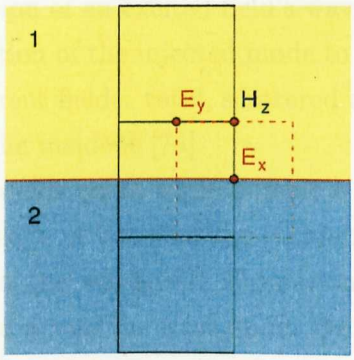

Figure 4.2: Yee cells and field components at material boundary. Dotted line shows the Yee cell region surrounding the E_x-field component. Since both materials appear in this region the current density used to calculate the E_x-field value must be averaged.

components are only affected by the material characteristics present in a Yee cell sized region surrounding them, see figure 4.2. As the E_x-field component is situated at the centre of the Yee cell, and thus exactly on the material boundary, it is the only component affected by the change in material. The E_x-field component is directed parallel to the material interface. Therefore, according to the method outlined in [80] the current density along the x-axis is halved. It is halved since there is no current density in the conventional cladding material, which is modelled as having a frequency independent refractive index of 1.

4.3 Mode injection

The aim in this chapter is to examine the propagation of a pulse along a NRI material waveguide. To be able to study in detail the behaviour of a mode, it is important that only one mode be injected at a time. This is difficult in NRI material waveguides, since one of their key features is the ability to sustain two modes of the same order, a forward and a backward, simultaneously. It is possible to have waveguides in which only forward or backward modes can exist, through careful selection of optical and geometric parameters [43]. However, since in this thesis the propagation of modes through waveguides with a wide range of geometries (i.e. waveguides with different core thickness) is examined, the ability to inject single modes, even in situations where two can exist, is required.

4.3.1 Total field scattered field (TFSF) - wave injection

In order to inject the pulse, a TFSF injection plane was used. The TFSF method was chosen as it allows the orientation of an excited field's wavevector to be pre-defined, thus enabling the propagation direction of the injected mode to be chosen. The TFSF method works by specifying three different fields: total, scattered and incident. The total field is the sum of the scattered and the incident [78].

Inside the TFSF box total fields exist, while outside it only scattered fields exist. At the spatial points around the edge of the box, the incident field has to be used in order to connect the two regions. In the waveguide simulations only one side of this box is used. The TFSF plane is placed across the waveguide. By adjusting the incident fields to match the profile of the desired mode, a wave can be injected into the simulation, which only propagates into the total field region. In practice a small but negligible portion of the wave propagates into the total field region (i.e. travels in the opposite direction along the waveguide).

To create the temporal shape of the pulse envelope, the amplitude of the source field is varied over time. In this thesis the injected pulse has a Gaussian shape, described by:

$$f(t) = e^{-P^2(t-T_{att}-T_{sus})^2}, \tag{4.1}$$

$$P = \frac{\sqrt{\ln(2)}}{\text{HWHM}}, \tag{4.2}$$

where T_{att} is the attack of the pulse, T_{sus} its sustain and HWHM its Half Width Half Maximum value. The attack gives the length of time between the source being turned on and the pulse envelope reaching its maximum amplitude. In this thesis the duration of the attack is the same as that of the decay, T_{dec} . The decay is the time taken for the amplitude to drop from its maximum value to zero. The HWHM value determines how quickly the amplitude rises to, and falls from, its maximum value. It gives the interval between the time when the pulse envelope is half its maximum value and the time it reaches its maximum value. The final parameter which can be adjusted is the sustain. This describes how long the amplitude of the pulse remains at its maximum value, before the start of the decay. Mostly in this thesis the value of the sustain is kept at zero, however, in chapter 6 a non-zero value is used. Through adjusting these parameters the envelope of the pulse is adjusted and thus the pulse's bandwidth is also altered.

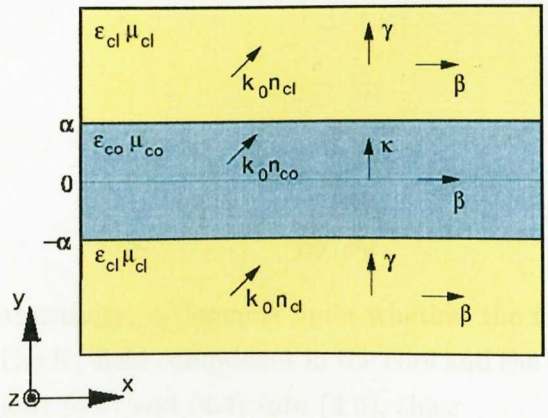

Figure 4.3: Vector components in different sections of the waveguide geometry.

4.3.2 Dispersion curves - pulse profile

The desired mode is selected by shaping the transverse profiles of the incident fields. To calculate these transverse profiles, the transverse wavevectors of the mode in both the core and cladding are required. These can be obtained through the mode's dispersion curve. Solution ansatzs for the fields in the core and the cladding, such as those found in [44, 55, 81], are used to derive the dispersion curve. In this work, bulk even bound modes are examined, which means that the solution ansätze for the TM modes in the core and cladding materials are:

$$H_z(y) = B\cos(\kappa y) \qquad -\alpha < y < \alpha, \tag{4.3}$$

$$H_z(y) = Ae^{-\gamma(|y|-\alpha)} \qquad |y| > \alpha, \tag{4.4}$$

where B and A are the maximum field amplitudes in the core and cladding respectively; κ is the transverse wavevector in the core; γ the transverse wavevector in the cladding; and α half the width of the core, see figure 4.3.

Since only even modes are investigated, a cosine term is sufficient to describe the the mode's field profile in the core. As only bound modes are of interest, the field in the cladding is described using a decaying exponential. A radiating mode has an oscillating field in the cladding, indicating energy escaping from the waveguide.

Now that the solution ansatzs for the H-field of the TM mode are obtained, the con-

version method from this to the other field components is required. Using both Faraday's and Ampere's equations, whilst also taking into account the fact that the simulations are in 2D (meaning that the fields will not vary along the z-axis and therefore $\partial/\partial z = 0$), it is possible to write:

$$\mathrm{E}_y = -\frac{\beta}{\epsilon\omega}\mathrm{H}_z, \tag{4.5}$$

$$\mathrm{E}_x = \frac{1}{\epsilon\omega}\frac{\partial \mathrm{H}_z}{\partial y}, \tag{4.6}$$

where the value of permittivity, ϵ, depends upon whether the field is taken to be in the core or the cladding. The E_x-field component in the core and the cladding can be obtained by substituting equations (4.3) and (4.4) into (4.6), thus:

$$\mathrm{E}_x = \frac{1}{\epsilon_{cl}\omega}\left[-\gamma\frac{y}{|y|}Ae^{-\gamma(|y|-\alpha)}\right], \tag{4.7}$$

$$\mathrm{E}_x = \frac{1}{\epsilon_{co}\omega}\left[-B\kappa\sin(\kappa y)\right], \tag{4.8}$$

where ϵ_{cl} refers to the permittivity of the cladding and ϵ_{co} is the permittivity of the core. The boundary equations, as in (2.37), show that the tangential E- and H-field components should be continuous across the core cladding interface. For the case of a TM mode this means that in the absence of surface charges or currents, the value of the H_z-field component in the core and cladding should be equal at the interfaces (i.e. at y=-α and y=α), as should those for the E_x-field component. In this work surface charges and currents are taken to be absent.

By equating equations (4.3) and (4.4) at either of the interfaces, i.e. substituting α or $-\alpha$ into both, the relation:

$$A = B\cos(\kappa\alpha), \tag{4.9}$$

is found, which can be substituted into equation (4.7). When this result is combined with equation (4.8) at one of the boundaries, through cancellation and manipulation, one obtains:

$$\tan(\alpha\kappa) = \frac{\epsilon_{cl}\gamma}{\epsilon_{co}\kappa}. \tag{4.10}$$

Solving this equation allows the transverse wavevectors of the bound modes to be obtained. Before it can be solved, however, it is necessary to express the transverse wavevector in the cladding, γ, in terms of the transverse wavevector in the core, κ, thus ensuring only one unknown is present. In practice, since the term $\alpha\kappa$ appears on the RHS the equation is solved for $\alpha\kappa$. To express the equation in this form the RHS was multiplied by $\frac{\alpha}{\alpha}$, so that the term $\alpha\kappa$ was common to both.

The starting point in obtaining the relation between κ and γ is equation (2.41), which describes the relation between the longitudinal,β, transverse, k_t, and total, K, wavevectors, and can be used to show that:

$$k_t^2 = K^2 - \beta^2. \tag{4.11}$$

Equation (4.11) is applicable in the waveguide core, where the longitudinal wavevector is smaller than the total wavevector. In the cladding, however, the longitudinal propagation coefficient is greater than the total wavevector and thus the transverse wavevector calculated using equation (4.11) is imaginary. An imaginary value for the transverse wavevector does not produce a decaying field when used in equation (4.4). To avoid this problem a different relation between the total wavevector and its components is used for the specific case of the wavevectors in the cladding. If the longitudinal propagation constant is larger than the total wavevector, this new equation gives a real and negative value for the transverse wavevector:

$$\gamma^2 = \beta^2 - K^2. \tag{4.12}$$

Using these new equations, equations (4.11) and (4.12), along with the relations $K^2 = \epsilon\mu k_o^2$ and $\beta^2 = n_{eff}^2 k_0^2$, allows expressions for $\alpha\kappa$ and $\alpha\gamma$ to be found, thus:

$$\alpha\kappa = \alpha\sqrt{\epsilon_{co}\mu_{co}k_0^2 - n_{eff}^2 k_0^2}, \tag{4.13}$$

$$\alpha\gamma = \alpha\sqrt{n_{eff}^2 k_0^2 - \epsilon_{cl}\mu_{cl}k_o^2}. \tag{4.14}$$

Since the longitudinal propagation constant ($\beta^2 = n_{eff}^2 k_0^2$) of each mode is indentical in the core and cladding regions, equations (4.13) and (4.14) can be combined to give:

$$\alpha\gamma = \sqrt{\alpha^2(\epsilon_{co}\mu_{co} - \epsilon_{cl}\mu_{cl})k_0^2 - (\alpha\kappa)^2}. \tag{4.15}$$

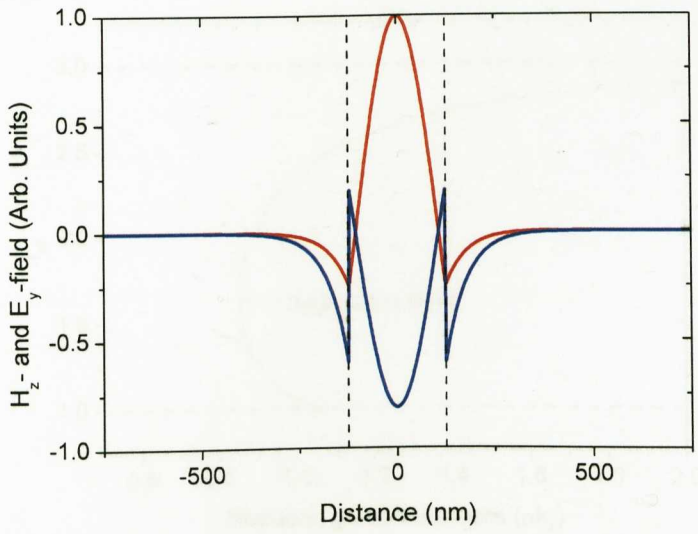

Figure 4.4: Example of the transverse field profiles of a TM_2^b mode. (red line) H_z-field and (blue line) E_y-field. Distance is measured from the central axis of the waveguide, (dashed black lines) denote the core cladding boundaries. In this instance the intrinsic refractive index of the core is -3 (for both the permittivity and the permeability), while in the cladding the intrinsic refractive index is 1.

A computer program is then written to scan through values of $\alpha\kappa$ and find which solve equation (4.10). Using equation (4.15) the transverse wavevector in the cladding can then be obtained. These values can then be inserted into the ansatz equations, (4.7) and (4.10), to obtain the profile of the pulse in both the core and cladding. A Matlab program was used to calculate the field value at each E_y and H_z field position along the injection plane. Figure 4.4 shows examples of the H_z- and E_y-field profiles calculated for a TM_2^b mode using this method.

4.4 Geometric dispersion curve

One way of displaying the dispersion curve of the allowed modes is to construct an effective index, n_{eff}, vs. reduced guide thickness,αk_0, graph, sometimes called a geometric dispersion curve, as shown in [51]. Using the reduced guide thickness value allows the effect on the mode of either varying the frequency of the propagating light (while keeping the core thickness constant), or altering the thickness of the core (for a constant frequency), to be calculated. An equation to calculate the geometric dispersion curve can be obtained by substituting equations (4.13) and (4.14) into equation (4.10), giving:

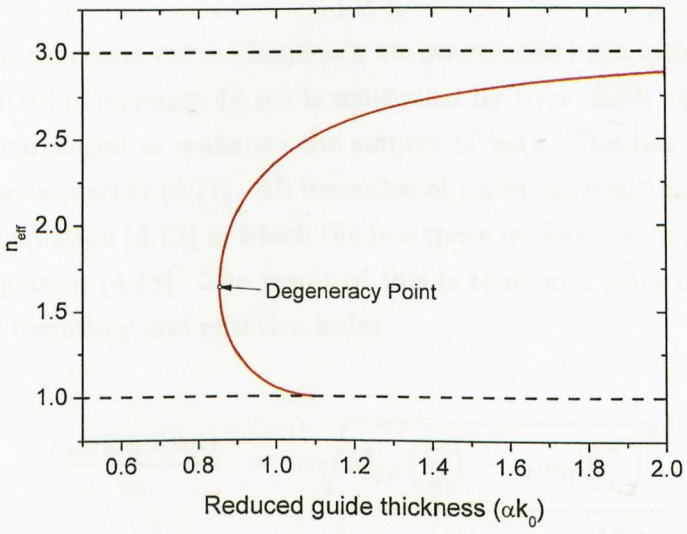

Figure 4.5: An example of a geometric dispersion curve. Absolute values of effective index are used.

$$\alpha k_o = \frac{1}{\sqrt{\epsilon_{co}\mu_{co} - n_{eff}^2}} \left[\arctan \left\{ \frac{\epsilon_{co}\sqrt{n_{eff}^2 k_0^2 - \epsilon_{cl}\mu_{cl}k_o^2}}{\epsilon_{cl}\sqrt{\epsilon_{co}\mu_{co}k_0^2 - n_{eff}^2 k_0^2}} \right\} + \mathrm{m}\pi \right], \qquad (4.16)$$

where μ_{co} and μ_{cl} are the permeability of the core and cladding materials, respectively, and m is related to the order of the mode. Since equation (4.16) is only valid for even modes, m=1 is used to calculate the mode with two nodal points. This is due to the fact that the fundamental mode can not exist in NRI waveguides.

The geometric dispersion curve is then found by plotting the reduced guide thickness values obtained for a range of effective refractive index values (ranging from the intrinsic refractive index of the core to that of the cladding).

An example of a geometric dispersion curve for a waveguide containing a core with refractive index of -3 is shown in figure 4.5. Note, it is easier in the calculation of the dispersion curve to treat the effective index extracted as a positive number. In the case where the NRI material is in the core of the waveguide the forward modes occupy the region of the dispersion curve below the degeneracy point, i.e. they have effective indices closer to the cladding material. The backward modes are located above the degeneracy point since their effective index is closer to that of the cladding material. As can be seen from figure 4.5 the sign of the effective refractive index is the same for the two modes.

4.5 Dispersion curves

The conventional dispersion curve (frequency vs. wavevector) can also be calculated. To obtain this, the RHS of equation (4.10) is multiplied by α/α. Both equations (4.10) and (4.14) are then rearranged to make $\alpha\gamma$ the subject of both. The two equations are then equated to produce equation (4.17). All instances of $\alpha\kappa$ in the resulting equation are then substituted with equation (4.13) in which the free space wavevector term is converted into frequency, see equation (4.18). The result of this is that both sides of the equation are now functions of frequency and effective index:

$$\frac{\epsilon_{co}\alpha\kappa\tan(\alpha\kappa)}{\epsilon_{cl}} = \alpha\sqrt{n_{eff}^2\left(\frac{\omega}{c}\right)^2 - \epsilon_{cl}\mu_{cl}\left(\frac{\omega}{c}\right)^2}, \tag{4.17}$$

$$\alpha\kappa = \alpha\sqrt{\epsilon_{co}\mu_{co}\left(\frac{\omega}{c}\right)^2 - n_{eff}\left(\frac{\omega}{c}\right)^2}. \tag{4.18}$$

The equation can then be rearranged into its final form, equation (4.19). To calculate the frequency and effective refractive index values belonging to bound modes a range of frequencies is cycled through. The dispersion of the core material is accounted for by using the Drude model to re-calculate the core material's permittivity and permeability at each frequency.

At each frequency, the range of possible effective refractive index values (ranging from the absolute value of the core's refractive index, to the absolute value of the cladding's refractive index) is scanned through, to find if there is a value which solves equation (4.19):

$$\tan\left[\alpha\sqrt{\epsilon_{co}\mu_{co}\left(\frac{\omega}{c}\right)^2 - n_{eff}\left(\frac{\omega}{c}\right)^2}\right] = \frac{\epsilon_{cl}\alpha\sqrt{n_{eff}^2\left(\frac{\omega}{c}\right)^2 - \epsilon_{cl}\mu_{cl}\left(\frac{\omega}{c}\right)^2}}{\epsilon_{co}\alpha\sqrt{\epsilon_{co}\mu_{co}\left(\frac{\omega}{c}\right)^2 - n_{eff}^2\left(\frac{\omega}{c}\right)^2}}. \tag{4.19}$$

4.6 Preliminary simulations

Preliminary simulations were conducted, both to check that pulses could be generated in the waveguide and, if so, to examine the effect on the pulse of varying different simulation parameters, such as the Courant value, the width of the cladding material, and the resolution. In the simulations conducted, the central frequency of the pulse was set at 400THz with a free space wavelength of 750nm. The core width was set to 225nm, and the intrinsic refractive index of the NRI material (used in the waveguide core) was -3 at the central frequency. The pulse injected had an attack/decay time of 265fs and a

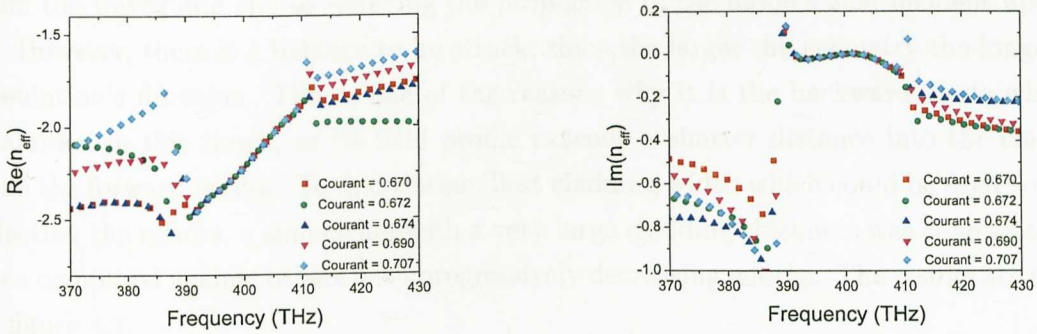

(a) (b)

Figure 4.6: Effect of varying the Courant value on the extracted effective refractive index

HWHM of 67.7fs. This gave the pulse a bandwidth of (390-410)THz.

4.6.1 Effect of Courant value

To see if the Courant value had any effect on the propagating pulse a set of simulations were conducted, using values ranging from 0.670 to 0.707. The maximum Courant value is calculated through the equation $1/\sqrt{N}$, where N is the dimension of the simulation. Since this is a 2D simulation, the maximum possible Courant value is 0.707.

The width of the cladding (i.e. the distance from the core to the PML is set to 500nm). The results are shown in figure 4.6 and, as with figure 3.3, meaningful results are only produced within the range of frequencies excited by the pulse. In the case of both the real and imaginary components of the effective index, the Courant value seems to make no difference to the results produced within the bandwidth excited by the pulse. The NRI material modelled in these simulations does not contain loss, as reflected by the imaginary part of the effective refractive index being located around zero. These results are shown in figure 4.6b.

For the simulations conducted in this chapter a Courant value of 0.706 was used.

4.6.2 Effect of cladding width

As mentioned earlier, the boundary used to terminate the cladding region along the y-axis is a PML. This type of boundary is designed to absorb any radiation incident upon it, at any frequency or angle. In practice, however, the boundary does not work well for radiation incident upon it at very shallow angles (i.e. propagating almost parallel to the boundary). Unfortunately, since the waveguide is orientated parallel to the boundary, this is the angle at which a large proportion of the fields are incident. To overcome this

issue, the width of the cladding region is increased, moving the PML boundary away from the waveguide and so reducing the proportion of the mode's field incident upon it.

However, there is a balance to be struck, since the larger the geometry the longer the simulation's duration. This is one of the reasons why it is the backward mode which is examined in this thesis, as its field profile extends a shorter distance into the cladding than the forward modes. To find the smallest cladding width which could be used without affecting the results, a simulation with a very large cladding thickness was conducted and then compared against others with progressively decreasing widths. The results are shown in figure 4.7.

As can be seen, reducing the cladding width has no effect on the real part of the extracted effective refractive index, figure 4.7a. There is only a small variation in the imaginary part of the effective refractive index, figure 4.7b, but there appears no systematic change due to the varying width, especially at the frequencies excited by the pulse.

Another method of judging the effect of varying the cladding width is by examining the time signal recorded at a point on the waveguide's central axis. The signal from simulations with different cladding thicknesses are shown in figure 4.8. The simulations were run for approximately 3ps , long enough for the propagating pulse to pass over the measurement point three times, which occurs due to the periodic boundaries at either end of the simulated waveguide. As seen in figure 4.7 when thinner widths of cladding are used the H_z-field undergoes a drastic increase in amplitude, i.e. it "blows up". This is a consequence of the evanescent field of the propagating mode intersecting at a very shallow angle with the PML placed on the outer edge of the cladding. To reduce the proportion of the evanescent field which intersects with the PML, the width of the cladding is increased. By doing this the unphysical increase in the amplitude occurs at a later time. When a cladding width of 1250nm is used the simulation remains stable for the entire run time. The change in the shape undergone by the pulse between its returns to the measurement points is due to a combination of the waveguide and material dispersion.

To obtain the effective refractive index results presented in figure 4.7 the time signal between 0-0.56ps was used, i.e. the signal from the pulse's first pass over the measurement point. This means the results should be obtained before standing waves can be created, since with the periodic boundaries there is the potential for the waveguide to behave as a circular resonator. Looking at the time signal just after the first pulse has passed over, around the 0.5ps point, there seem to be some additional pulses. These additional pulses do not affect the effective index extracted. However, they might have some other effects. Increasing the cladding width reduces the amplitude of these pulses. For this reason, the following waveguide simulations will have the larger cladding width.

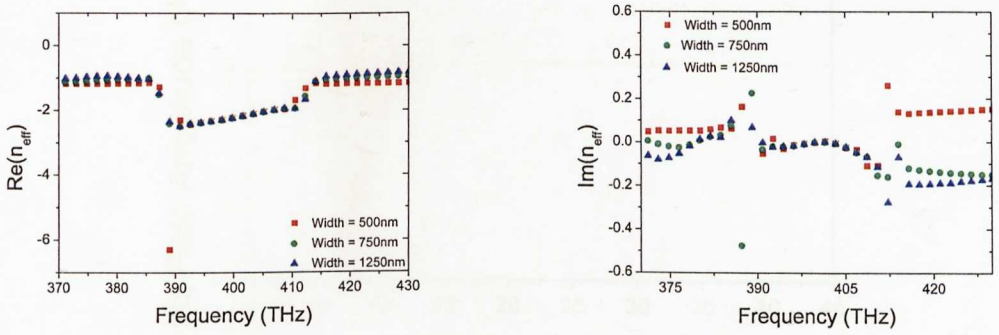

(a) (b)

Figure 4.7: The effect of varying the width of the cladding material on the extracted effective refractive index.

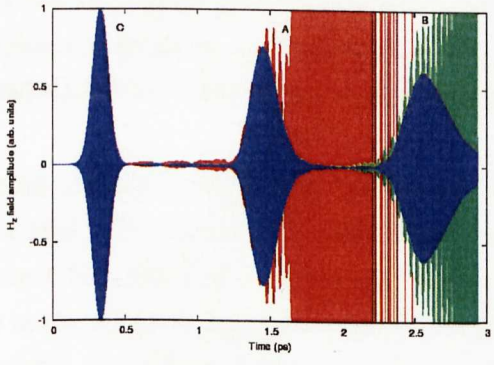

Figure 4.8: The H_z-field time signal observed for different thicknesses of cladding material: A) 500nm, B) 750nm and C) 1250nm.

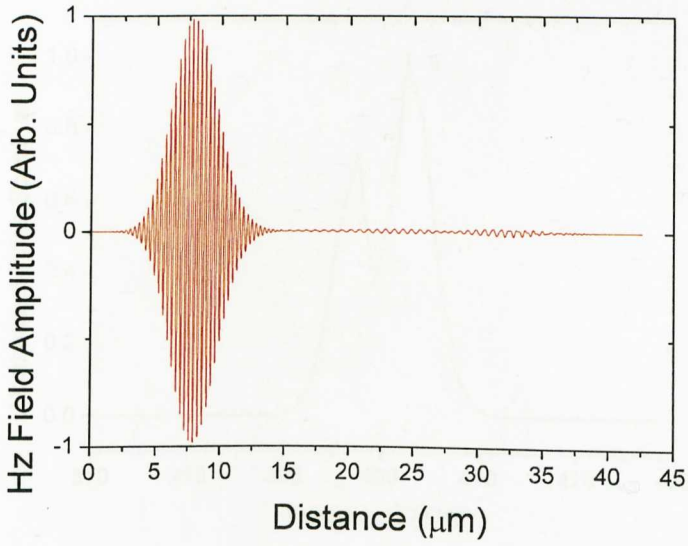

Figure 4.9: H_z-field along the center of the waveguide. The anomalous double peaked pulse can be seen on the right of the plot.

4.6.3 Presence of counter propagating pulse

In the waveguide simulations conducted, an anomalous double peaked pulse is observed, figure 4.9. The pulse is generated at the source plane, but propagates in the counter direction to the main pulse. Due to the periodic boundaries, this anomalous pulse then leaves the geometry on the far left and re-enters the waveguide on the right.

The phase fronts of the anomalous pulse travel in the same direction as its envelope, figure 4.11. This suggests the anomalous pulse is a forward mode. The pulse's spectrum is shown in figure 4.10. From the figure it can be seen that the frequencies present in the pulse are in the range (390-410)THz. This is the same range as that in the main pulse excited.

The amplitude of the anomalous pulse is seen to increase as the core width used is decreased (figures 4.14, 4.16a). The reason for this can be ascertained by examining the dispersion curve (figure 4.13). Even though the same frequency range is used in each simulation, the difference in the effective index between the highest and lowest frequencies excited increases as the width of the core is reduced. This is due to the gradient of the dispersion curve becoming more shallow over the frequency range excited. As the range of effective index becomes larger there is greater disparity between the transverse profile of the central frequency (used to inject the pulse) and the profiles belonging to the highest and lowest frequencies. The coupling of the highest and lowest frequencies to the main backward mode thus becomes poorer. Instead these frequencies couple more to the

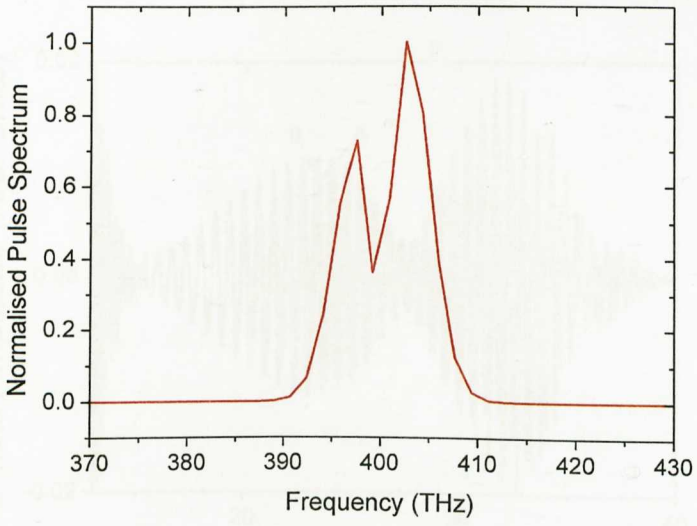

Figure 4.10: Frequency components excited in anomalous pulse

forward mode (i.e. the anomalous pulse) causing an increase its initial amplitude.

The data in figure 4.10 supports this reasoning. Extracting the frequency components comprising the anomalous pulse shows it to be largely composed of frequencies either higher or lower than the central frequency. Compared to that of the higher and lower frequencies the magnitude of the central frequency component contained within the anomalous pulse is reduced. This is due to the transverse profile of this frequency matching that used to inject the mode. That the frequency distribution of the anomalous pulse contains peaks at high and low frequencies suggests the reason why the spatial distribution of the anomalous pulse has two peaks (figures 4.9 and 4.11). One peak containing the higher frequency components and the other the lower frequency components.

4.6.4 Effect of resolution

The final test conducted was to check the effect of varying the resolution used in the simulations. In the previous waveguide simulations the resolution used was $\lambda_0/300$. Therefore, in free space the central wavelength was 300 Yee cells long. As a consequence in the waveguide core, where the refractive index at the central frequency is -3, the central wavelength would be resolved with 100 Yee cells. To check if this is sufficient, simulations with resolutions of $\lambda_0/360$ and $\lambda_0/420$ were conducted. In these simulations, the width of the cladding was set to 1250nm. The comparision between the real part of the propagating pulse's effective index extracted from these simulations is shown in figure 4.12.

For each resolution, the dimensions of the simulations (when expressed in SI units)

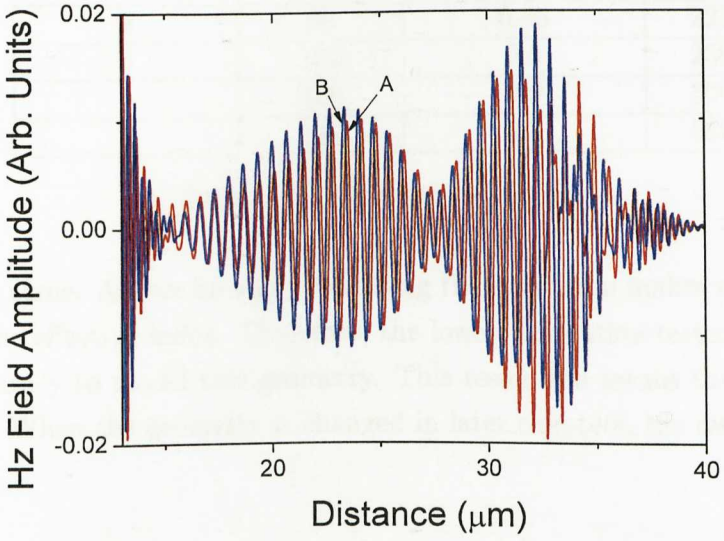

Figure 4.11: Zoom in on the anomalous pulse, (red line, A) pulse after 519fs, (blue line, B) field 0.577 fs later.

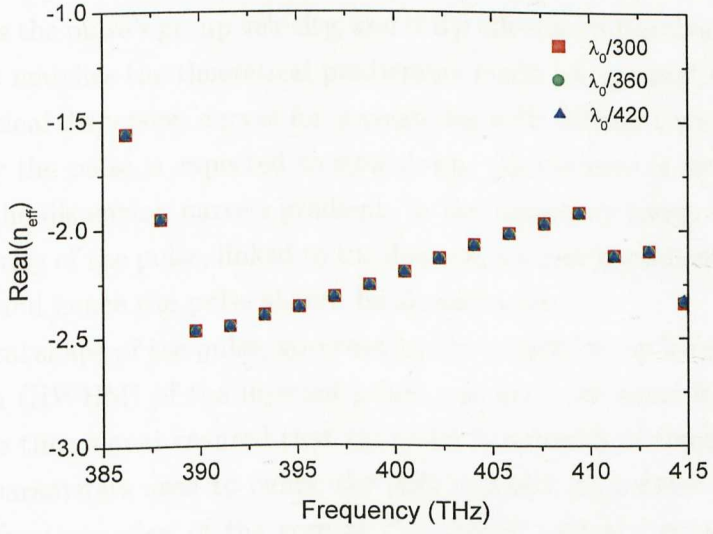

Figure 4.12: Effect of resolution on the real component of the extracted effective refractive index.

	Core Width		
Simulation No.	Cells (Δx)	Wavelength (λ_0)	SI (nm)
1	82	0.41	205
2	90	0.45	225
3	100	0.5	250
4	120	0.6	300
5	140	0.7	350

Table 4.1: Core widths examined

were kept the same. As can be seen, increasing the resolution makes no difference to the real part of the effective index. Therefore, the lowest resolution tested, $\lambda_0/300$, provides sufficient accuracy to model this geometry. This resolution means the length of the Yee cell is 2.5nm. When the geometry is changed in later chapters, the resolution required is re-calculated.

4.7 Core width

Now that the factors which affect the simulation results have been examined, numerical experiments can be conducted to test some of the predictions made about NRI material waveguides. One of the most interesting features is the effect of the waveguide's core thickness on the speed of a propagating pulse. A set of simulations of pulse propagation through waveguides with different core widths was conducted to check whether thinning the core reduces the pulse's group velocity, and if the effective refractive index experienced by these pulses matches the theoretical predictions made using equation (4.16).

The theoretical dispersion curves for waveguides with different widths of core, figure 4.13, show why the pulse is expected to slow down. As the core is reduced, the average magnitude of the dispersion curve's gradient, in the frequency range excited, decreases. The group velocity of the pulse, linked to the dispersion curve's gradient through $v_g = \frac{\partial \omega}{\partial k}$, also decreases and hence the pulse should be slowed down.

The temporal shape of the pulse, governed by the attack/decay length and Half Width Half Maximum (HWHM) of the injected pulse, was kept the same for each simulation. Using the same time signal ensured that the same bandwidth of frequencies was always excited. The parameters used to define the NRI material properties were also kept the same. The refractive index of the core at the pulse's central frequency was set to -3 through careful selection of the plasma frequency. For these simulations, the NRI material was modelled as being loss-less, i.e. the collision frequency was set to 0 ($\Gamma = 0$). As with the preliminary simulations, the cladding material was modelled as being dispersion less with a refractive index of 1. The core thicknesses examined are listed in table 4.1.

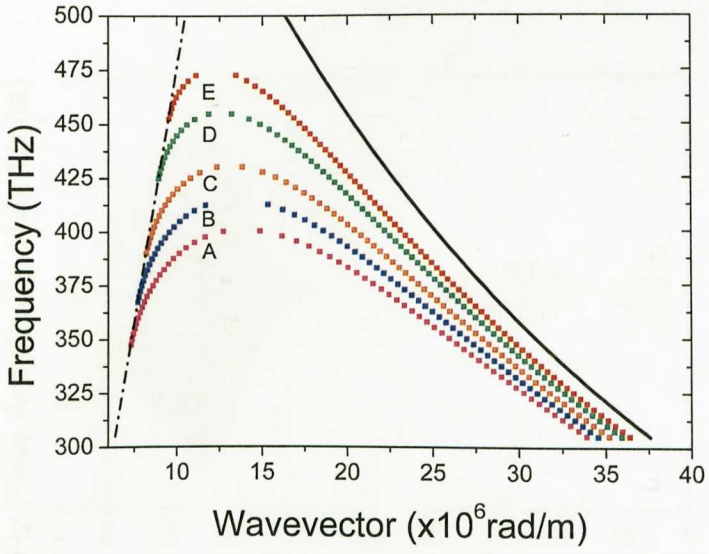

Figure 4.13: Dispersion curves calculated for the TM_2^b mode using the analytic method. The dispersion curves are for waveguides with core widths of: 205nm (A,pink), 225nm (B,blue), 250nm (C,orange), 300nm (D,green) and 350nm (E,red). The dot-dash line is the dispersion of the light in the cladding and the thick black line is the dispersion of the light in the NRI material.

When the thinnest core was simulated, the anomalous pulse was observed to be very large and the main excitation lost its Gaussian shape. Instead of the amplitude of the envelope returning to 0, in a symmetrical manner to its build up, it decayed very slowly, as can be seen in figure 4.14. These effects are due to the high proximity of the frequencies excited to the degeneracy/cutoff point. Overlaying the dispersion curve for the TM_2^b mode in a waveguide of width 205nm, onto the spectrum of the main pulse excited in the simulation, shows that the pulse's central frequency (400THz) is very close to the degeneracy point and that higher frequencies are sharply cut off, see figure 4.15.

Figure 4.13 shows that there is a larger variation in effective index with frequency in waveguides with thinner cores. This is taken to be the reason for the increasing size of the anomalous pulse with decreasing core thickness. The larger the variation in effective index with frequency, the greater the change in the transverse profile with frequency. As a consequence, decreasing the core width increases the discrepancy between the shape of the central frequency's transverse profile (used for the excitation), and the profiles of the surrounding frequencies. This increases the coupling of frequencies to the forward mode.

Fortunately, it is only for the thinnest core modelled that the anomalous pulse is very large. For thicker cores, it is small enough to not affect the main pulse to such a degree.

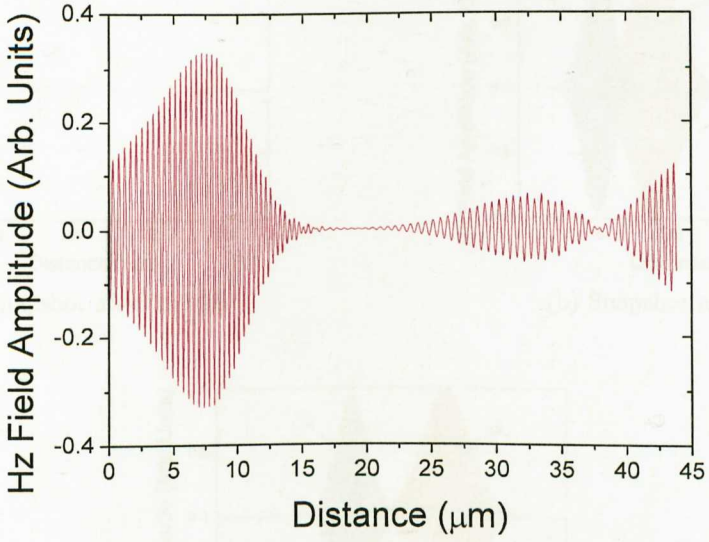

Figure 4.14: Plot of H_z-field along central axis of waveguide. Width of waveguide is 205nm and snap shot is taken after a time interval of 82.4 ps

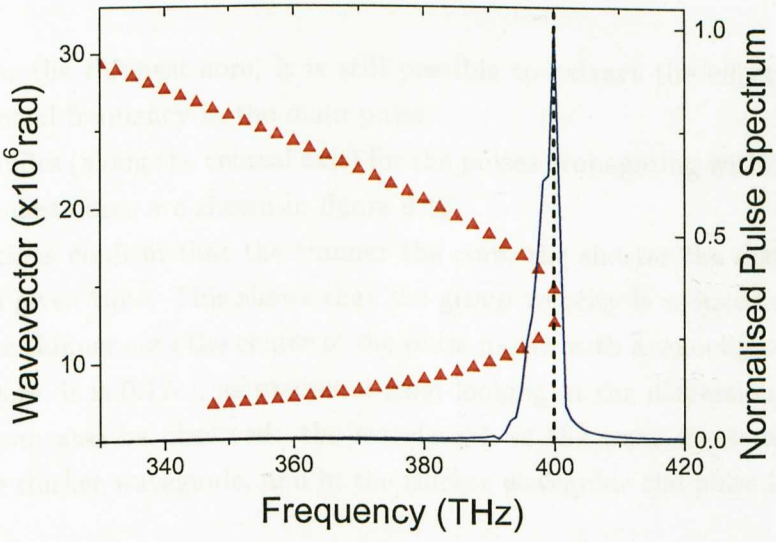

Figure 4.15: Comparison between the dispersion curve for the TM_2^b mode in a waveguide with core width 205nm (red triangles) and the spectrum of the main propagating pulse (blue line).

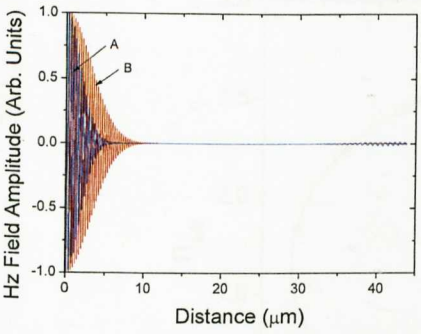

(a) Snapshot after 264.9fs

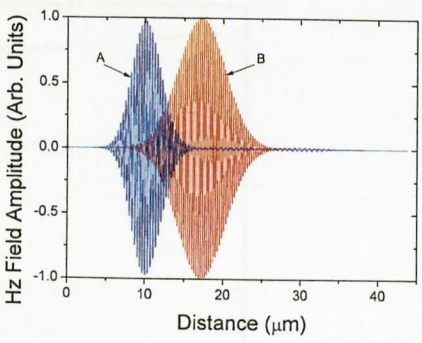

(b) Snapshot after 588.7fs

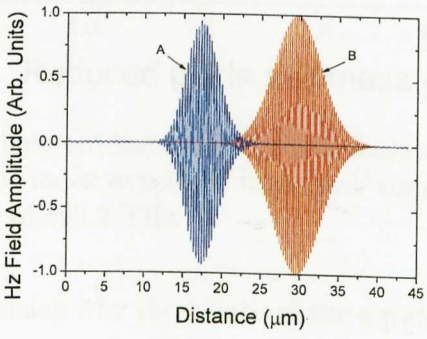

(c) Snapshot after 824.2fs

Figure 4.16: Pulse propagation in waveguides with core thickness 225nm (blue, A) and 350nm (red, B)

In fact, even for the thinnest core, it is still possible to extract the effective refractive index of the central frequency in the main pulse.

The field profiles (along the central axis) for the pulses propagating within the thickest and second thinnest cores are shown in figure 4.16.

The simulations confirm that the thinner the core, the shorter the distance a pulse propagates in a given time. This shows that the group velocity is reduced with the core thickness (in the thinner core the center of the pulse moves with a velocity of 0.07c, while in the thicker core, it is 0.12c), as predicted from looking at the dispersion curves. Two other features can also be observed: the wavelength of the wave fronts are shorter in the pulse in the thicker waveguide, and in the thicker waveguide the pulse has a broader envelope.

The existence of the shorter wavelength is explained by looking at the dispersion curve, figure 4.13. The larger the core thickness, the larger the wavevector, and so the shorter the wavelength. The dispersion curve also shows that, in a thicker core, for a given range of frequencies, a narrower range of wavevectors will be excited due to the gradient of the

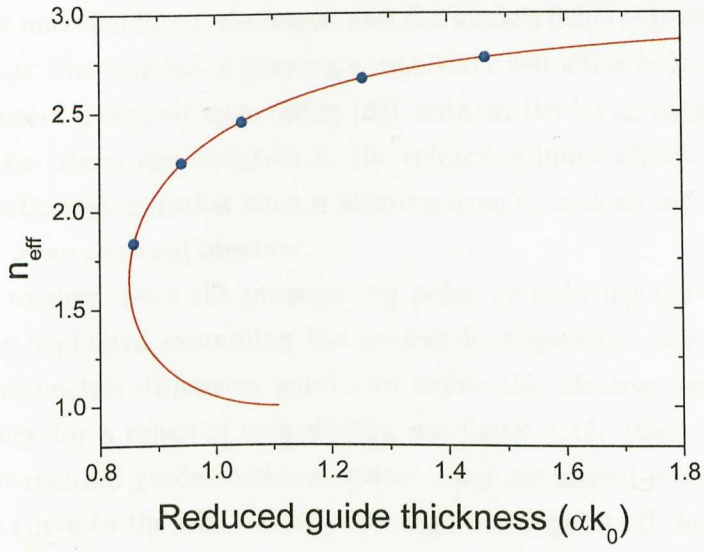

Figure 4.17: Comparison between the analytically calculated geometric dispersion curve (red, line) and the effective index extracted from each simulation (blue, dots). Both are calculated for a frequency of 399.2 THz

dispersion curve. This explains why the length of the envelope has increased. If taken to the extreme of only exciting a single wavevector then the length of the envelope would be infinite, since a CW would be generated.

As with the preliminary simulations, the effective refractive index of the propagating pulses were recorded in the different core widths. The values extracted were compared against the theoretical predictions made using equation (4.16). In practice, since discrete time steps were used, only discrete frequencies could be extracted. The dispersion curve was calculated for 399.2 THz, the closest frequency extract to the central frequency 400 THz. At this frequency the core refractive index is -3.01136 not -3. As can be seen from figure 4.17, there is an exact match between the prediction and the simulation results. This shows that the behaviour of the pulse in different thicknesses of waveguides is as predicted.

4.8 Varying the refractive index of the core

One way of slowing down a light pulse in a waveguide is to vary the width of the core material, as shown in section 4.7. For a backward mode if the core width is reduced, the proportion of the pulse's field in the cladding increases. This equals out the energy flow in the core and cladding, and so reduces the group velocity of the pulse. An alternative method is to vary the intrinsic refractive index of the waveguide's core material. By

reducing the intrinsic refractive index of the core, the difference between the refractive index of the core and cladding is decreased and the mode's fields extend a greater distance into the cladding. The concept of varying a material's refractive index has recently been discussed in terms of transformation optics [82], with particular focus on its use for optical invisibility cloaks. Here, the variation in the refractive index allows light to be guided around a particular region, rather than scattering from it, making any object within that region invisible to an external observer.

The ability to slow down the propagating pulse by reducing the refractive index of the core can be explained examining the geometric dispersion curves of modes in the waveguide. A geometric dispersion curve can define the effective index experienced by a single frequency for a range of core widths, see figure 4.17. Reducing the core width (2α) causes the reduced guide thickness value (αk_0) associated with that frequency to move along the curve to the left, towards the degeneracy point. If the core width is kept constant, the reduced guide thickness (αk_0) at a particular frequency is also constant. This reduced guide thickness value remains constant even if the refractive index of the core material is changed. Varying the core refractive index of the waveguide does, however, alter the mode's geometric dispersion curve. If the core refractive index is reduced the dispersion curve is shifted to higher values of reduced guide thickness. This property enables light to be slowed through the variation of the core refractive index. For example, if the frequency and waveguide core width values give a reduced guide thickness of 3.5 (dotted line figure 4.18a), and the intrinsic refractive index of the core is -2, the mode will be able to propagate. Increasing the core refractive index shifts the dispersion curve to higher values of reduced core thickness and moves the degeneracy point of the curve closer to the reduced thickness value of the propagating frequency. If the core refractive index is increased to -1.3, the reduced guide thickness of the frequency would coincide with the degeneracy point and the frequency would be halted.

The variation in the effective index of the mode with core refractive index, for an αk_0 value of 3.5, is shown in figure 4.18b. As with varying the core thickness, there is a point in the taper (here taper refers to changing core refractive index, rather than width) where both forward mode and backward modes exist. At a smaller core refractive index, the modes meet at the degeneracy point. It should be noted that the gap between the forward and backward branches in figure 4.18b, at the degeneracy point, is an artifact of the method used to calculate the curve. In reality, for a lossless core material, the two join.

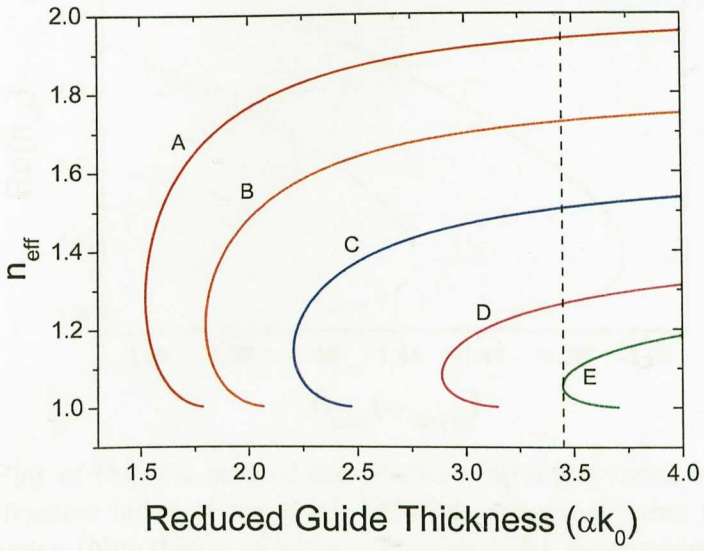

(a) Geometric Dispersion curves for waveguides with core refractive index at the central frequency, of -2 (A,red), -1.8 (B,orange), -1.6 (C,blue), -1.4 (D,pink) and -1.3 (E,green).

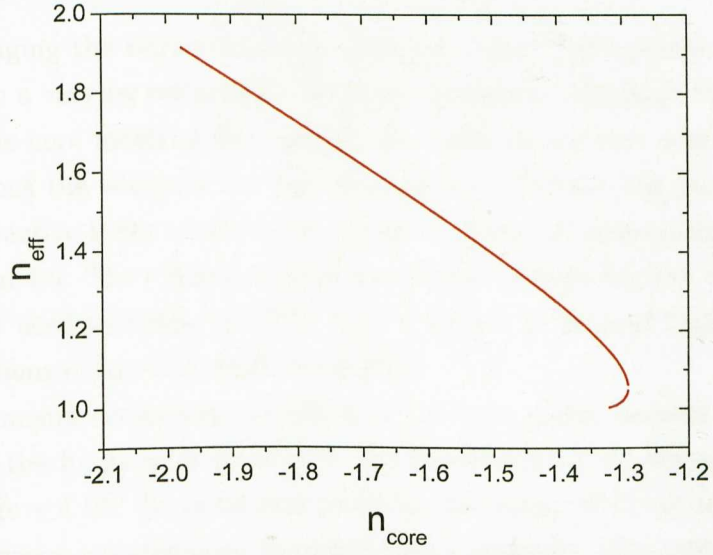

(b) Variation of the effective index with refractive index of core, as experienced by the central frequency of the pulse, for a constant width of core.

Figure 4.18: Effect of varying the refractive index of the core material

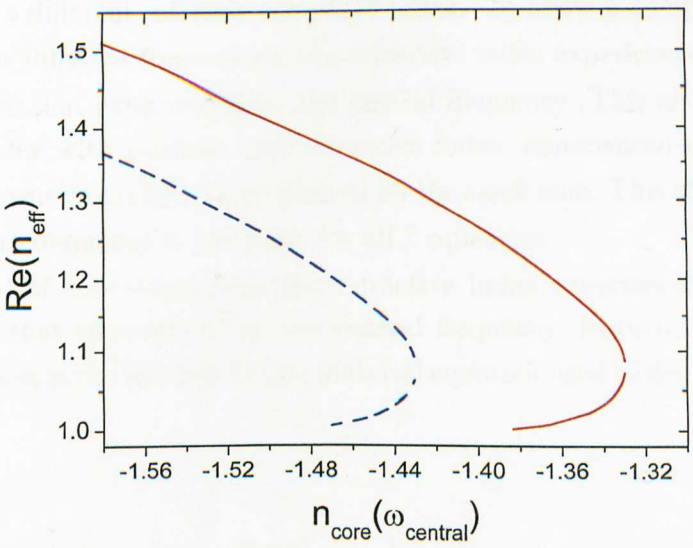

Figure 4.19: Plot of the real part of the effective refractive index vs. the real part of the intrinsic refractive index of the core. Effective refractive index experienced by the minimum frequency (blue dash), effective refractive index experienced by the maximum frequency (red solid). Both curves are plotted against the core refractive index experienced by the pulse's central frequency.

4.8.1 Varying core index - simulations

To test if changing the refractive index does slow down light pulses, a simulation of a waveguide with a varying refractive index was conducted. Although the intrinsic refractive index of the core material was varied, the width of the core was kept constant. In these simulations the width of the core was 712nm. To slow the pulse, the magnitude of the core refractive index needs to be increased along the propagation direction, as detailed in section 4.8. The refractive index was varied by reducing the value of the plasma frequency (ω_p) used to define the NRI core material; a method that has been used in FDTD simulations of metamaterial cloaks [83].

The experiments examining the effect of the core width became harder to analyse when some of the frequencies present in the pulse were at, or beyond, the degeneracy point, as in figure 4.14. To avoid this problem, the range of frequencies comprising the injected pulse was calculated prior to running the simulation. The refractive index values, over which the NRI core was varied, were chosen to ensure that these frequencies would always be able to propagate. In the simulation conducted, the intrinsic refractive index of the core material varied from -1.44 to -1.5, as measured at the central frequency of the pulse.

When determining the range of core refractive indices to use it must be remembered

that the core NRI material is dispersive. Therefore, each frequency will experience the core as having a different intrinsic refractive index. To allow a comparison between the behaviour of the different frequencies, the refractive index experienced by each frequency is converted into that experienced by the central frequency. This allows the variation of the effective index with intrinsic core refractive index, experienced by both the highest and lowest frequencies excited, to be plotted on the same axis. This conversion is possible since the plasma frequency is the same for all frequencies.

The method of converting from the refractive index experienced by one frequency, $\mathrm{Re}(\mathrm{n}_1(\omega_1))$, to that experienced by the central frequency, $\mathrm{Re}(\mathrm{n}_2(\omega_2))$, is shown below. The starting point is the loss-less Drude material equation used to define the NRI material core:

$$\begin{aligned} \mathrm{Re(n)} &= 1 - \frac{\omega_p^2}{\omega^2}, \\ \omega_p &= \sqrt{1 - \mathrm{Re(n)}}\omega, \\ \sqrt{1 - \mathrm{Re(n_1)}}\omega_1 &= \sqrt{1 - \mathrm{Re(n_2)}}\omega_2, \\ \mathrm{Re(n_1)} &= 1 - \frac{(1 - \mathrm{Re(n_2)})\omega_2^2}{\omega_1^2}. \end{aligned} \tag{4.20}$$

A pulse with a longer temporal duration was used in these simulations than that used to analyse the effect of the core width. The attack/decay time is increased from 265fs to 794.8fs and the HWHM is increased from 67.7fs to 159fs. As a result the pulse has a narrower bandwidth (395-405THz as opposed to 390-410THz). This allows the taper to reach a smaller value of core refractive index, whilst still allowing the highest and lowest frequencies present to propagate.

In figure 4.19 it can be seen that as the refractive index of the core is increased, the degeneracy point of the highest frequency is arrived at first. Therefore, as long as the refractive index in the core is always less than -1.44, all the frequencies present in the pulse should be able to propagate and the pulse should retain its Gaussian shape, unlike in figure 4.14.

To allow for the taper to be as gradual as possible (to avoid coupling to other modes) the wavelength used in the simulation was reduced from $300\Delta x$ to $200\Delta x$. However, since the maximum (absolute) value of the core refractive index experienced by any of the frequencies in the pulse is 1.57, there are still sufficient grid cells per wavelength to allow for wavelength resolution.

The variation in the core refractive index along the central axis of the waveguide is shown in figure 4.21. Mirror boundaries are used at the two ends of the x-axis. Periodic

boundaries can no longer be used since the intinsic core refractive index is no longer the same at the two ends of the waveguide (the refractive index jumps from -1.44 to -1.5).

Snapshots of the propagating pulse's H_z-field component along the central axis of the waveguide are shown in figures 4.20a and 4.20b. To allow the effect of the varying refractive index to be determined, a separate simulation was run using a geometry with no variation in the core refractive index. Here, the whole length of the core was defined with a refractive index of -1.5 (as experienced by the central frequency of the pulse).

Figures 4.20a and 4.20b show that the peak of the pulse, in the tapered core waveguide, has propagated a shorter distance at the points the snapshots are taken than the pulse in the core of constant refractive index. In addition, the maximum amplitude of the pulse in the tapered waveguide has increased to a value greater than 1, i.e. a value greater than its initial value. This is a result of the front of the pulse propagating more slowly than the rear, as is observed in other studies where the width of the core is varied [51, 52].

The effective index experienced by the central frequency of the propagating pulse at different positions along the waveguide was extracted. These results were obtained by placing pairs of measurement points along the waveguide. The results are then plotted, along with those calculated analytically, against the intrinsic refractive index of the core material, see figure 4.22

Like the previous set of simulations, the frequency extracted was actually 399.7 THz, slightly different from the central frequency of 400THz. To account for this, equation (4.20) is used to change the refractive index of the core at the position of each measurement point, to the intrinsic refractive index experienced by the frequency actually measured (ω_m).

Good agreement is seen between the theoretical prediction and the results extracted from the simulation.

4.9 Summary and conclusions

Through FDTD simulations the behaviour of light in NRI waveguides with different core widths has been analysed. A method was implemented which enabled the extraction of the propagating pulse's effective refractive index. This has allowed for the quantitative comparison between simulation and analytic results. The slowing of the light pulses in waveguides with thinner cores, predicted in [17], has been confirmed and the effective indices extracted from the simulations are found to match those obtained from analytic theory.

A novel alternative to reducing the width of the core, that of increasing the core's refractive index, has also been examined. This method leads to many of the same features

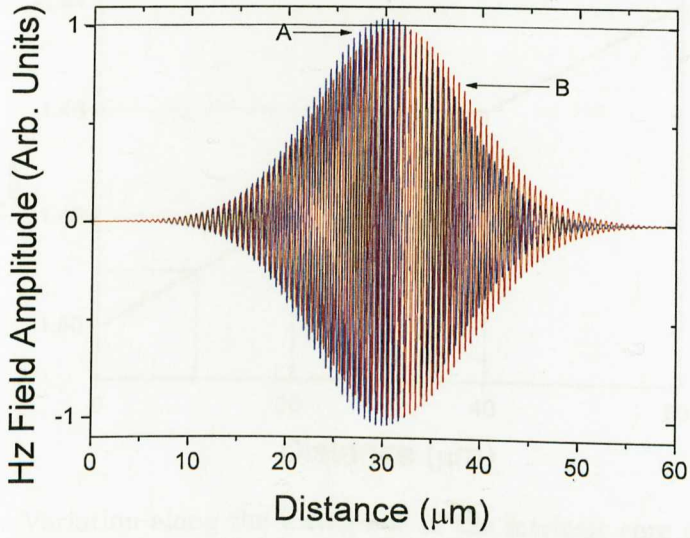

(a) Snapshot after 1236fs.

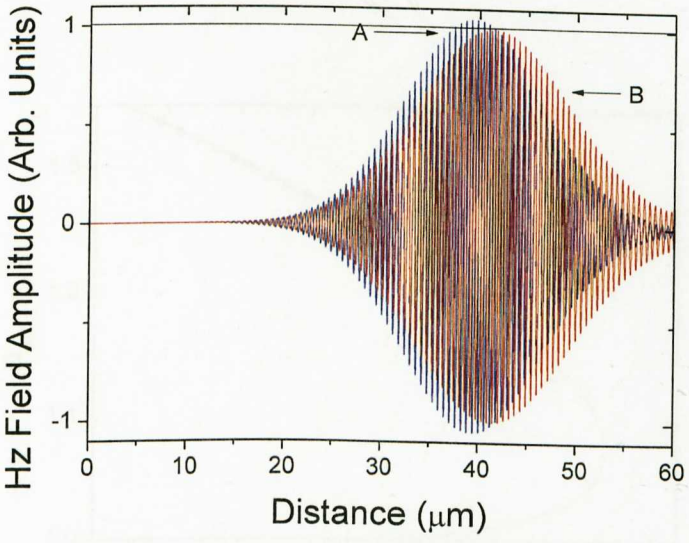

(b) Snapshot after 1401fs.

Figure 4.20: Comparison between H_z-field distributions along the waveguide's central axis for cases where the core's intrinsic refractive index varies, pulse (A, blue), and remains constant, pulse (B,red).

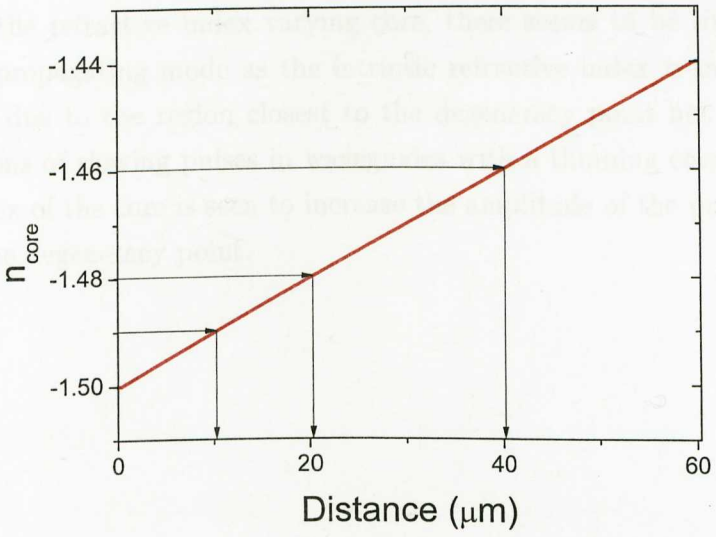

Figure 4.21: Variation along the waveguide of the intrinsic core refractive index

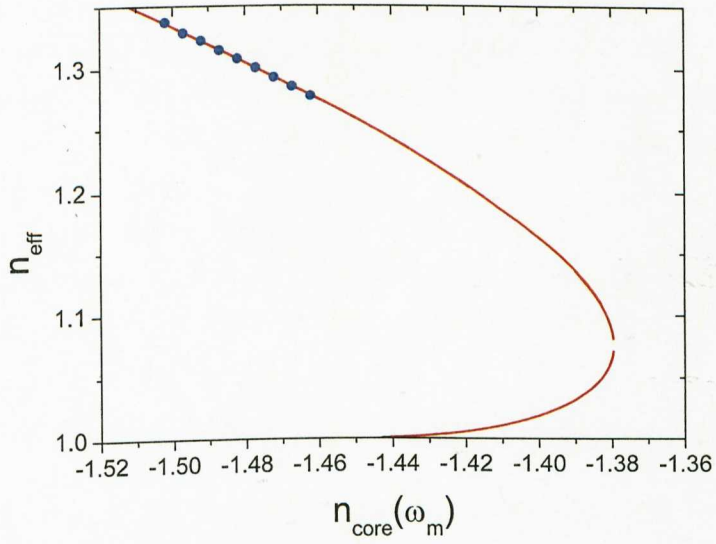

Figure 4.22: Comparison between effective refractive index extracted and intrinsic refractive index of core. Analytic calculation (red line) and effective index extracted from the simulation (blue dots). Both sets of results calculated for a frequency of 399.7 THz.

found in simulations of waveguides with thinning cores, i.e. the presence of a degeneracy point and the ability to slow the light pulse. Again, effective refractive index values extracted from the simulations agree with analytic predictions. From observing the pulse profile along the refractive index varying core, there seems to be little or no coupling to a counter propagating mode as the intrinsic refractive index is increased. However, this could be due to the region closest to the degeneracy point not being probed. As in investigations of slowing pulses in waveguides with a thinning core [51], reducing the refractive index of the core is seen to increase the amplitude of the pulse envelope as the pulse nears the degeneracy point.

Chapter 5

Loss compensation

5.1 Introduction

In this chapter, the effect of including loss in the NRI core material is examined and the use of a gain material to compensate for this loss is investigated. The consequences of positioning the gain material at varying distances from the core, of increasing the thickness of the gain material strip, and of altering the dispersion of the gain material, are also looked at.

As before, the effective index of the propagating pulse is extracted. In this case this is to determine what effect, if any, the inclusion of gain material has on the pulse. In addition to extracting the effective refractive index by recording the change in the pulse between two points along the waveguide, the alteration of the height of the pulse with time is also observed. This allows the temporal loss experienced by the pulse to be obtained. These results are then compared against analytic results, produced by another member of my research group.

Finally, the loss in energy of the pulse as a whole (rather than the energy loss of individual frequencies) is determined. The loss/ gain observed using these three different methods (spatial, temporal and total energy) are then compared.

5.2 Drude (with loss) and Lorentz material model

To create a more realistic model of a NRI material, loss in the core needs to be included. This is because of the high levels of loss present metamaterials have. Loss is included through having a non zero value for the collision frequency (Γ) in the Drude model. However, as can be seen from equations (3.33) and (3.34), the collision frequency appears in the definition of both the real and imaginary parts of the NRI material's refractive index. This means that for the real part of the refractive index to be kept constant while

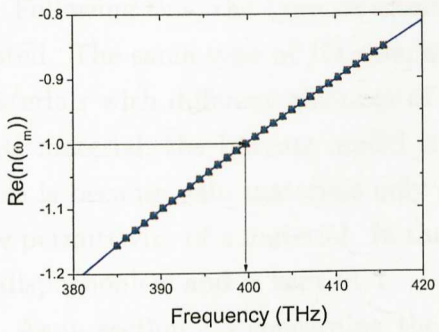

(a) Real component of refractive index

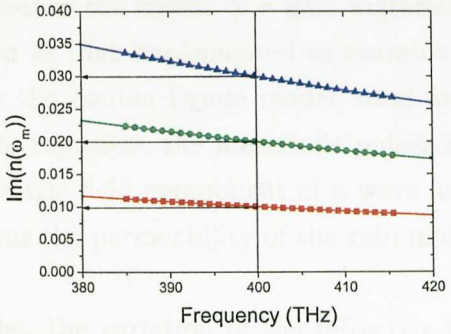

(b) Imaginary component of refractive index

Figure 5.1: Comparison between the refractive index calculated through simulation (points) and analytic (lines) methods for materials with a refractive index of -1+i0.01 (red,square), -1+i0.02 (green,circle) and -1+i0.03 (blue,triangle)

different values of the imaginary component are tested, the plasma frequency would have to be varied as well as the collision frequency.

The plasma and collision frequency values required to generate a specific complex refractive index for a certain frequency were calculated by making the square of the plasma frequency (ω_p^2) the subject of the equations for both the NRI material's real and imaginary components, equations (3.33) and (3.34), and then equating the two. This produces an equation in which only the collision frequency is unknown:

$$(1 - \mathrm{Re(n)})(\omega^2 + \Gamma^2) = \frac{\mathrm{Im(n)}(\omega^3 + \omega\Gamma)}{\Gamma}. \tag{5.1}$$

To find the collision frequency required to produce any refractive index value, it is simply a matter of inserting the required real and imaginary components of the refractive index into equation (5.1) and then searching through the range of possible collision frequencies until the equation is solved. The value obtained for the collision frequency can then be used in equation (3.33) to find the required plasma frequency.

To test the implementation of different NRI materials, with the same real part of refractive index but different imaginary components, a 1D simulation setup was used, similar to that detailed in section 3.6. Here, however, only a single material was used, preventing the creation of a reflected pulse and the interference problems this causes. Periodic boundaries were implemented at both ends of the NRI material. Three separate simulations were run with refractive index values of -1+i0.01, -1+i0.02 and -1+i0.03. The values of the plasma and collision frequencies were found using equation (5.1). The results are shown in figures 5.1a and 5.1b.

Good agreement is found between the simulation and theoretical data.

Following this, the Lorentz model used to produce the effects of a gain material was tested. The same type of 1D simulation was used as that implemented to examine NRI materials with different amounts of loss. Unlike the double Drude model, used for the NRI material, the Lorentz model is only used to represent the material's polarisation. This is because gain materials only affect the electric field component of a wave and so the permittivity of a material. In these simulations the permeability of the gain material is dispersionless and is kept at 1.

As in section 3.3 concerning the Drude model, the variation of the refractive index of the Lorentz material with frequency can be found from the Lorentz model's material equation (3.15). However, as the Lorentz material only acts upon the electric component of the field the Lorentz material equation gives the variation in the permittivity with frequency:

$$\mathrm{Re}(\epsilon(\omega)) = \epsilon_\infty + \frac{(\omega_p^4 - \omega_p^2\omega^2)\Delta\epsilon}{\omega_p^4 - 2\omega^2\omega_p^2 + 4\Gamma_e^2\omega^2 + \omega^4}, \tag{5.2}$$

$$\mathrm{Im}(\epsilon(\omega)) = \frac{2\Gamma_e\omega\Delta\epsilon\omega_p^2}{\omega_p^4 - 2\omega^2\omega_p^2 + 4\Gamma_e^2\omega^2 + \omega^4}. \tag{5.3}$$

The real and imaginary components of a material's refractive index can easily be found from its complex permittivity (assuming the material's permeability is 1) by taking the square root of the permittivity: $\mathrm{n}(\omega) = \sqrt{\epsilon(\omega)}$. The square root of this complex number is calculated by converting the quantities into exponential form:

$$\begin{aligned}
\mathrm{Re}(\epsilon(\omega)) + i\mathrm{Im}(\epsilon(\omega)) &= Ae^{i\theta}, \\
A &= \sqrt{\mathrm{Re}(\epsilon(\omega))^2 + \mathrm{Im}(\epsilon(\omega))^2}, \\
\theta &= \mathrm{atan}\left[\frac{\mathrm{Im}(\epsilon(\omega))}{\mathrm{Re}(\epsilon(\omega))}\right], \\
\mathrm{Re}(\mathrm{n}(\omega)) + i\mathrm{Im}(\mathrm{n}(\omega)) &= \sqrt{A}e^{i\frac{\theta}{2}}, \\
\mathrm{Re}(\mathrm{n}(\omega)) + i\mathrm{Im}(\mathrm{n}(\omega)) &= \sqrt{A}\left[\cos\left(\frac{\theta}{2}\right) + i\sin\left(\frac{\theta}{2}\right)\right].
\end{aligned}$$

The positive square root is taken since the gain materials permeability is 1 for all frequencies and in the frequency region used the real part of the gain material's permittivity is always greater than 1. Thus, the real part of the refractive index of the gain material must also be positive.

The values used to define the Lorentz material used in this test are, ϵ_∞=1, ω_p =

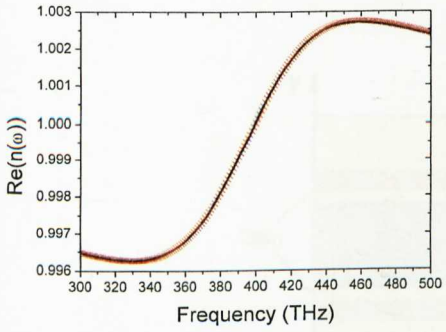

(a) Real component of refractive index

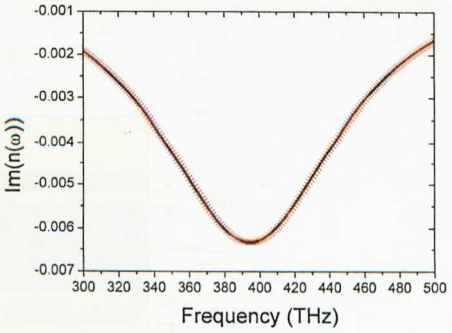

(b) Imaginary component of refractive index

Figure 5.2: Comparison between results from simulation (red,cross) and analytic (black,line) methods for a Lorentzian material

$2\pi \times 400$THz, $\Gamma = 400$THz and $\Delta\epsilon$= -0.004. The comparison between the simulation and theoretical results is shown in figures 5.2a and 5.2b.

Again there is good agreement between the simulation and analytic methods. Notice that in this preliminary test, the Lorentz material is modelled as having gain since the imaginary component of its refractive index is negative.

5.3 Incorporating gain into the waveguide.

Having tested the material equations for both the gain and the lossy NRI material, both the gain and the lossy NRI material can be added into the waveguide geometry examined in chapter 4. The choice was taken to include the gain material in a strip placed next to the waveguide core, as shown in figure 5.3. This is referred to as evanescent pumping since it is the evanescent field of the mode which overlaps with the gain material. Having the gain material outside the core avoids any consideration of how a gain material would interact with the microscopic structure of a NRI material. This simplifies the situation, since large variations in field strength at a microscopic level are expected in a NRI metamaterial which would affect the gain delivered [34, 35].

In the first set of simulations the effect of the gain material was analysed and a lossless NRI material i.e. one in which the collision frequency was set to 0, was used. This was done in order to allow the effect the gain material had on the propagating pulse to be isolated. The parameters of the gain material used in subsequent simulations are shown in figure 5.4a and 5.4b. The values used in the Lorentz model (equations (5.2) and (5.3)) to produce the gain material are $\epsilon_\infty = 1.00108$, $\omega_p = 2\pi \times 375.34$THz, $\Gamma = 100$THz and $\Delta\epsilon = -0.0043$. The peak of the gain was located close to the minimum frequency excited,

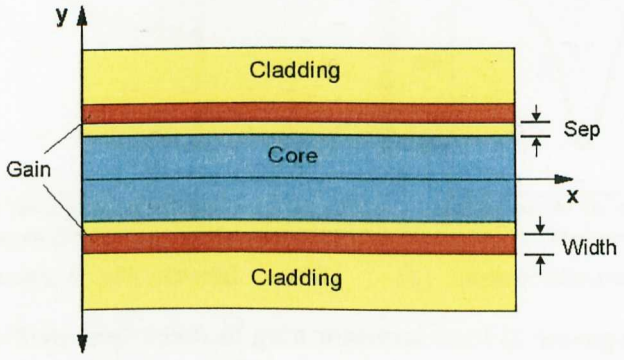

Figure 5.3: Waveguide geometry with gain strips included. In simulations the separation (Sep) and width of each strip is varied.

figure 5.4b. This produces a simple shape for the gain versus frequency curve over the bandwidth investigated. Having the peak of the gain located at the minimum frequency also ensures that the real part of the gain material's refractive index will be greater than 1 at each frequency excited in the pulse, figure 5.4a. The real part of the refractive index of the gain material is kept close to 1 to minimise the effect of the boundary between the gain material and the cladding (which, as before, is modelled as having a dispersionless refractive index of 1). Keeping the real part of the gain material's refractive index close to 1 also reduces the difference between the simulations with, and without, a gain material present in the waveguide.

The gain is expressed in terms of absorption coefficient (α_{abs}). This is calculated from the imaginary component of the refractive index through:

$$\alpha_{abs}(\omega) = \frac{2\omega \mathrm{Im}(n(\omega))}{\mathrm{c}}. \tag{5.4}$$

The absorption coefficient is defined in units of cm^{-1}. The intrinsic dispersion curve for the gain material in these first simulations is shown in figure 5.4a and 5.4b. Since the absorption coefficient is directly proportional to the imaginary component of the effective index, a negative value for the absorption coefficient refers to gain.

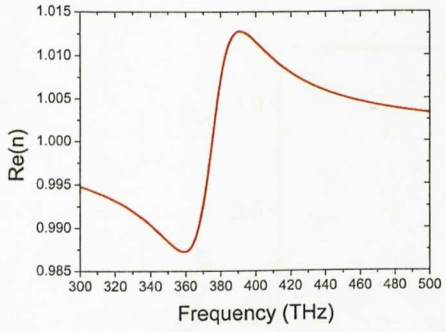

(a) Intrinsic dispersion of gain material

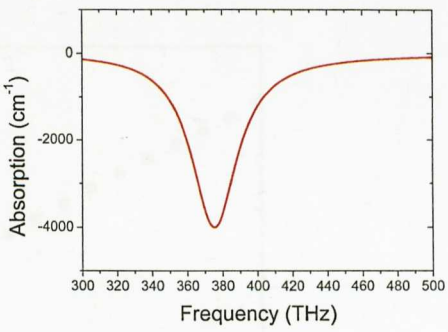

(b) Intrinsic absorption of gain material

Figure 5.4: Intrinsic dispersion of gain material used in waveguide simulations

5.4 Varying the dimensions of the gain material

In this section, the gain material described in section 5.3 is placed in a strip next to the core. The width of the core is set to 262.5nm, and is composed of a NRI with an intrinsic refractive index of -4 at the central frequency of the pulse (400THz). The cladding material, which has an intrinsic dispersionless refractive index of 1, extends for a distance of 937.5nm from the edge of the gain material to the top PML. The pulse injected has an attack/decay time of 183.9fs and a HWHM of 24.5fs. These values mean it has a bandwidth of (370-430)THz. A set of simulations were conducted which examine the effect on the propagating pulse of varying, first, the separation between the core and the gain material, and, second, the width of the gain material.

In both cases presence of the gain material is found to have no effect on the real part of the propagating pulse's effective refractive index. This is shown, for the case of varying core and gain material separation, in figure 5.5. The relation between the real part of the effective refractive index and frequency shown in this figure is exactly the same as that found when the width of the gain material is increased. The fact that varying these geometric parameters has no effect on the real part of the effective index is unsurprising, since the real part of the gain material's intrinsic refractive index is very close to that of the rest of the cladding at the central frequency of the pulse.

The gain material does, however, affect the absorption coefficient found for each frequency comprising the pulse. The presence of the gain material causes the dispersion of the pulse's absorption coefficient to take the same shape as that of the gain material. This is observed through comparing the shape of the curves in figure 5.4b with those in 5.6.

The effect the gain material has on the propagating pulse can be shown more clearly by using the confinement factor. This is the ratio of the effective gain (α_{eff}) experienced by

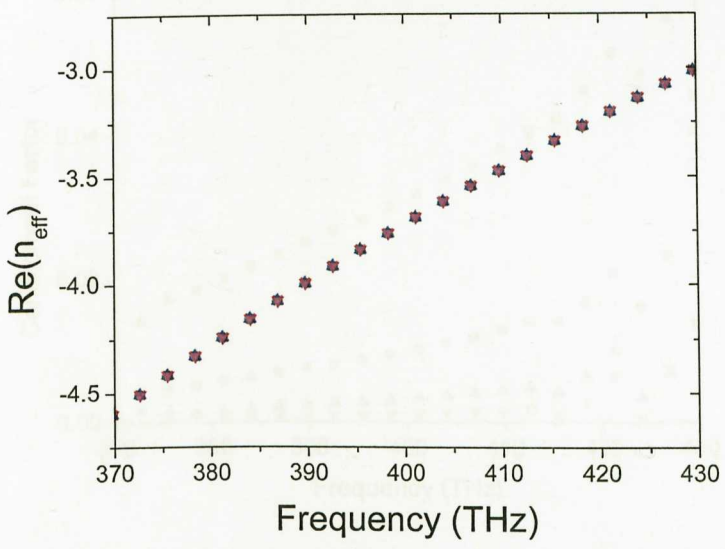

Figure 5.5: Effect of varying the separation between the core and the gain material on the real part of the effective refractive index experienced by the propagating pulse. The separations used are: (red, squares) 18.75nm, (green, circles) 37.5nm, (blue, up triangle) 56.25nm and (purple, down triangle) 75nm.

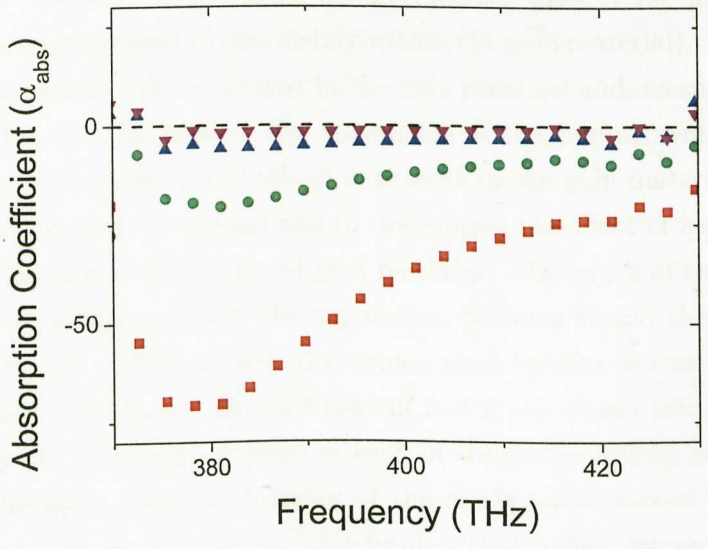

Figure 5.6: The effect on the absorption coefficient experienced by the propagation pulse of increasing the separation between the core and the gain material. The separation used are: (red, squares) 18.75nm, (green, circles) 37.5nm, (blue, up triangle) 56.25nm and (purple, down triangle) 75nm.

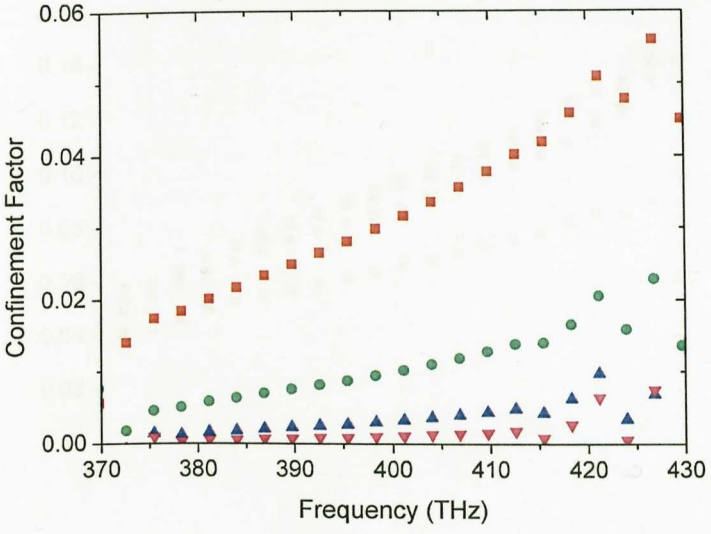

Figure 5.7: Effect of varying separation between core and gain material on confinement factor. The separation distances used are: (red, squares) 18.75nm, (green, circles) 37.5nm, (blue, up triangle) 56.25nm and (purple, down triangle) 75nm.

the propagating pulse and the gain material's intrinsic gain (α_{int}) [84]. The confinement factor gives a measure of the proportion of the field of the propagating pulse which intersects with the gain material (a confinement factor of 1 means the effective gain experienced by the pulse is the same as the intrinsic gain of the gain material, which implies that the pulse is located completely within the gain material). In these simulations only part of the pulse's field is located in the gain material and, as such, the confinement factor is less than 1. The smaller the magnitude of the confinement factor, the smaller the proportion of the pulse's field which is present in the gain material.

The first experiment conducted was to investigate the effect of increasing the separation between the core and the strip of gain material. The width of the gain material was kept constant at 187.5nm, whilst the separation between it and the core was increased in constant steps of 18.75nm, with the values used for the separation being 18.75nm, 37.5nm, 56.25nm and 75nm. The confinement factor calculated using the effective index experienced by the propagating pulse in each of these simulations is presented in figure 5.7. One of the most apparent features of the confinement factors extracted is that it increases with increasing frequency. This implies that higher frequencies extend further out from the core and thus further into the gain material than lower frequencies. This feature is a consequence of the intrinsic dispersion of the core material. The real part of the intrinsic refractive index has a smaller magnitude at higher frequencies, which means the higher the frequency the smaller the difference between the refractive index of the

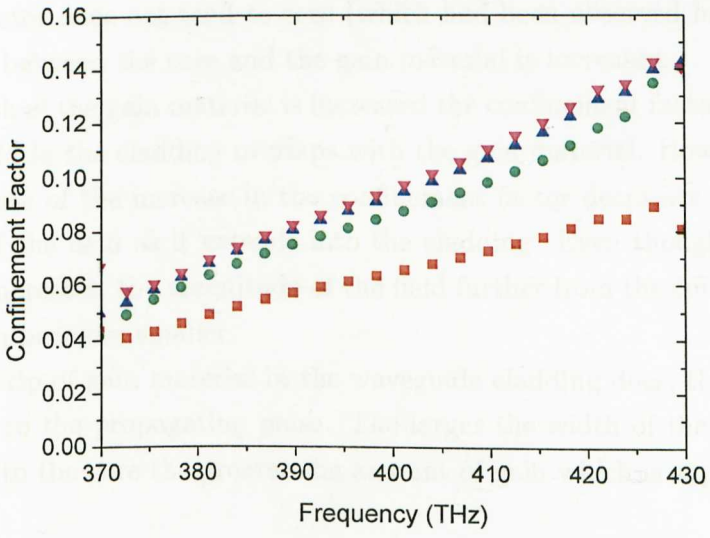

Figure 5.8: Effect of gain width on confinement factor. The widths of gain material used are: (red, squares) 18.75nm, (green, circles) 37.5nm, (blue, up triangle) 56.25nm and (purple, down triangle) 75nm.

core and cladding material. As seen in section 4.8, this causes the field at that frequency to extend further into the cladding.

The second point to notice from figure 5.7 is that the confinement factor decreases as the separation between the core and the gain material increases. This is due to the exponential decay of the pulse's field into the cladding. So, as the gain material is moved further away from the core, the magnitude of the field which intersects with it is reduced and the gain delivered to the pulse is decreased. That the field in the cladding is strongest at the core interface is apparently due to the greatest decrease in the confinement factor occurring between the first two positions of the gain material. As the field extends further from the cladding, its rate of decrease in strength is reduced and so the rate of change in the confinement factor also decreases.

At the furthest separation tested the confinement factor is almost zero, showing that at a distance of 75nm the mode's field has decayed almost to 0.

The next set of simulations investigates the effect of increasing the width of the gain material strip. Values used for the width of the strip are 18.75nm, 37.5nm, 56.25nm and 75nm. In each case the separation between the gain material and the core is 0nm.

The confinement factors obtained from these simulations are shown in figure 5.8. Many of the same features observed in figure 5.7 are present here. At higher frequencies the field extends further into the cladding and the confinement factor increases. Since the gain material is always placed next to the core, the strongest part of the field in

the cladding always intersects with the gain material. As a consequence of this the confinement factor does not tend to zero (which had been observed in figure 5.7), when the separation between the core and the gain material is increased.

As the width of the gain material is increased the confinement factor also increases, as more of the field in the cladding overlaps with the gain material. However, as the width increases the rate of the increase in the confinement factor decreases. Again this is due to the decay of the field as it extends into the cladding. Even though the width of the gain material increases, the magnitude of the field further from the core is less and so the increase in gain becomes smaller.

Placing a strip of gain material in the waveguide cladding does, therefore, allow gain to be supplied to the propagating pulse. The larger the width of the gain material and the closer it is to the core the greater the amount of gain which is supplied.

5.5 Including gain and loss

Before conducting experiments with simulations containing both loss and gain, the effect of varying the resolution and Courant value used in these types of simulations was investigated.

5.5.1 Effect of resolution

The resolution used for the simulations in this chapter is $\lambda_0/200$, i.e. the free space wavelength of the pulse's central frequency is 200 Yee cells long. To check if this is high enough to produce accurate results, a simulation with an even higher resolution ($\lambda_0/400$) was conducted for comparison.

The core width used in each was 300nm, the width of the cladding 937.5nm and the width of the gain material 187.5nm. The real part of the intrinsic core refractive index was -4 and its imaginary part 0.0016. The parameters of the gain material used for both simulations was ϵ_∞= 0.9946, $\omega_p = 2\pi \times 239.834$THz , $\Gamma = 7994.466$THz and $\Delta\epsilon$ = -1.

Both the real part of the effective index and the absorption coefficient extracted from the simulations, figure 5.9, show very little difference, indicating that the lower resolution is sufficient to model the effects which produce these parameters, e.g. the evanescent tail extending into the cladding material.

5.5.2 Effect of Courant value

As in chapter 4 the effect of varying the Courant value was analysed. A set of four simulations were conducted with Courant values of 0.7, 0.702, 0.704 and 0.706 implemented.

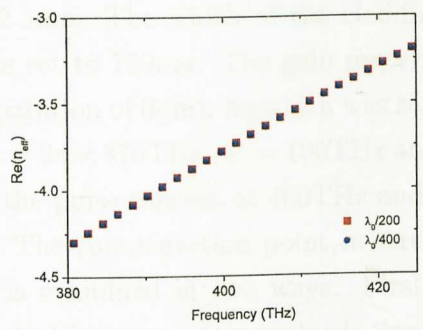

(a) Real part of effective index

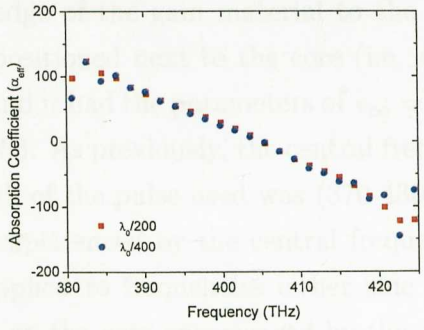

(b) Absorption coefficient

Figure 5.9: Resolution check with gain and loss implemented. Yee cell lengths of $\lambda_0/200$ (red, square) and $\lambda_0/400$ (blue,circle) are investigated

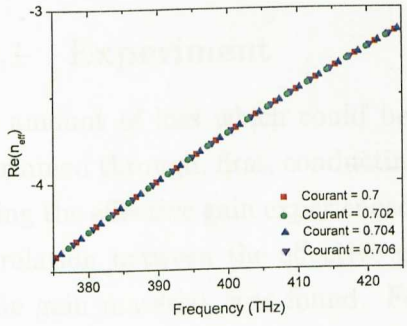

(a) Real part of effective refractive index

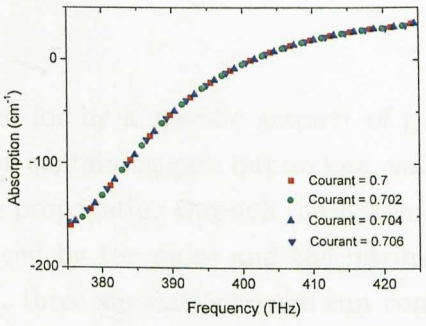

(b) Imaginary part of effective refractive index

Figure 5.10: Effect of Courant value

In each simulation the core width was set to 262.5nm, the width of the gain material to 187.5nm and the width of the cladding to 750nm. The real part of the intrinsic refractive index of the core NRI material was -4 and its imaginary component 0.0545. The parameters of the gain material used in each simulation were $\epsilon_\infty = 1.001$, $\omega_p = 2\pi \times 370\text{THz}$, $\Gamma = 100\text{THz}$ and $\Delta\epsilon = -0.0053$.

No differences in either the real or imaginary effective refractive index extracted were found, see figure 5.10. As a consequence of this, a Courant value of 0.7 was deemed to be sufficient in subsequent simulations.

5.6 Loss compensation

Now that the use of evanescent pumping has been shown to produce gain in a propagating pulse, the next step is to introduce loss into the NRI core and to see the effect of using

gain to compensate for this loss. Again, the width of the waveguide's core was set to 262.5nm. The width of the cladding, from the edge of the gain material to the PML, was set to 750nm. The gain material itself was positioned next to the core (i.e. with a separation of 0nm), its width was set to 187.5nm and it had the parameters of $\epsilon_\infty = 1.001$, $\omega_p = 2\pi \times 370\text{THz}$, $\Gamma = 100\text{THz}$ and $\Delta\epsilon = -0.0053$. As previously, the central frequency of the pulse was set at 400THz and the bandwidth of the pulse used was (370-430)THz.

The compensation point, where the net loss experienced by the central frequency is 0, is examined in two ways. First, the gain supplied to frequencies either side of the central frequency is examined. Second, the effect on the gain experienced by the central frequency when the width of the waveguide core is varied from its value when the central frequency is compensated. Varying the waveguide's core thickness is thought to have an effect on the gain supplied to the pulse since this varies the distribution of the pulse's field in the core and cladding regions.

5.6.1 Experiment

The amount of loss which could be compensated for by a specific amount of gain was determined through, first, conducting a simulation containing gain but no loss, and, then, finding the effective gain experienced by the pulse propagating through the system. Thus, the relation between the effective gain experienced by the pulse and the intrinsic gain of the gain material, was found. Following this, three simulations were run containing different amounts of loss, but without any gain. By finding the relation between the effective loss experienced by the pulse and the intrinsic loss of the core material, it is possible to calculate what magnitude of intrinsic loss in the core material would be compensated for by a specific gain material. It should be noted that in these experiments it is the basic principle of using a gain material to compensate for loss in a NRI waveguide which is of interest, rather than using realistic values either for the loss or the gain material. The real part of the refractive index of the NRI material used for the core is -4 and its absorption is 92.353cm^{-1} at the central frequency of the pulse.

From the intrinsic absorption curves of the NRI core and gain materials it can be seen that in this instance, gain with a magnitude of around 10 times that of the intrinsic loss was required to compensate for the loss. This is a result of the relatively small extension of the backward mode's fields into the cladding, and thus into the gain material. A forward mode, which has fields which extend much further into the cladding, would need a smaller amount of gain relative to the loss of the core. Despite this advantage in using a forward mode, a backward mode was chosen. This allowed both a smaller width of cladding to be used and a larger range of core thicknesses to be investigated, since the backward mode does not have a low frequency cutoff like the forward mode.

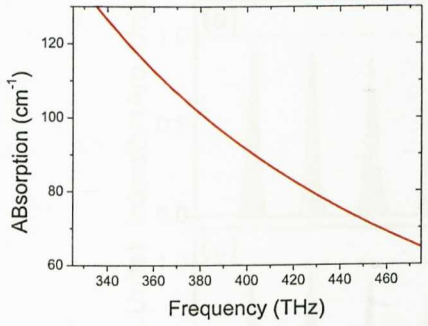

(a) The intrinsic absorption of NRI core material

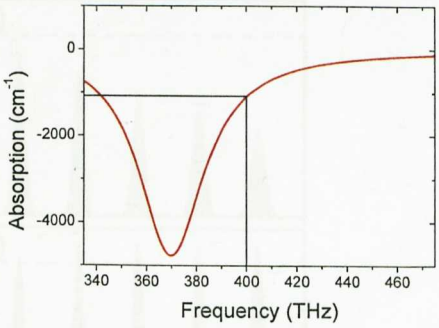

(b) The intrinsic absorption of gain material

Figure 5.11: Intrinsic absorption of the negative refractive index material used for the core and the gain material

Simulation	Loss Included	Gain Included
Case A	No	No
Case B	Yes	No
Case C	Yes	Yes
Case D	No	Yes

Table 5.1: Descriptions of simulations conducted

Using numerical simulations, it is possible to remove certain effects, i.e. the gain or loss. Four different simulations were conducted, denoted as A, B, C and D. Case A was the bench mark simulation, containing neither loss nor a gain material. Case B only contained loss and no gain. Case C included both loss and gain, and Case D had a lossless NRI core material, but a strip of gain material was included. The simulation parameters are summarised in table 5.1.

Snapshots, showing the envelope of the pulse's intensity when propagating through the different geometries, are shown in figure 5.12. The intensity is used in order to make the change in amplitude of the pulse easier to see. Figure 5.12(a) shows snapshots of the pulse intensity when neither loss nor gain is present (case A). A decrease in the maximum amplitude of the pulse is observed in this case. This seems strange considering that the NRI material is lossless and so no absorption takes place. The energy contained within the pulse therefore remains constant. The decrease in the pulse's maximum amplitude is thus not due to any loss in energy, but to the dispersion of the pulse as it travels along the waveguide. This dispersion should be present in each of the simulations. The dispersion experienced by the pulse varies slightly between each simulation due to the dispersion present in the gain material, and the change in the dispersion of the core material as a result of the introduction of the loss. As can be seen, however, from the variation

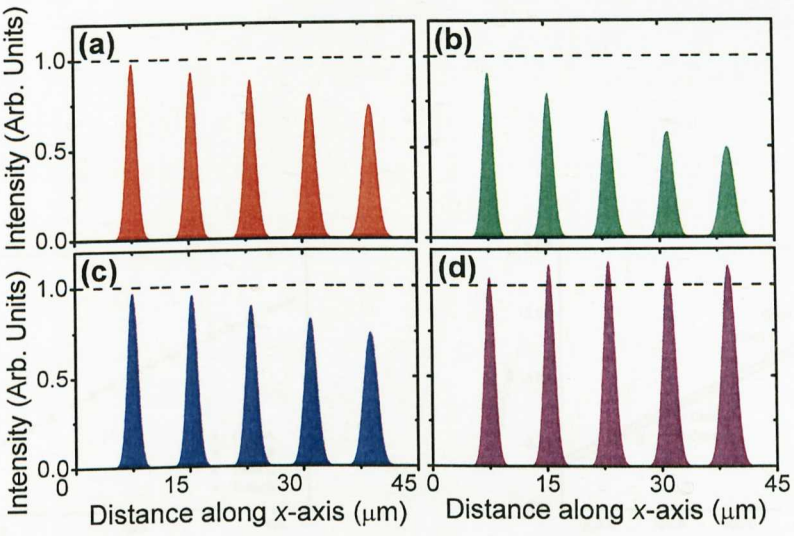

Figure 5.12: Snapshots of pulse intensity at different time points for a) case A, no loss or gain present, b) case B, loss present but no gain, c) case C, both loss and gain present and d) case D, only gain present. The pulse is propagating from left to right in all the pictures.

in the real part of the effective index with frequency for each case, figure 5.13a, these effects seem to be negligible since the curves are all very similar. Therefore the simulation without any loss or gain can be used as a reference.

When loss is introduced (case B), figure 5.12(b), the decrease in the pulse's amplitude is much greater than that seen with case A. This shows that an additional mechanism apart from the dispersion is at work, namely the absorption due to the intrinsic loss of the core material.

When both loss and gain are introduced (case C), figure 5.12(c), the decrease in the amplitude matches that observed in the bench mark simulation (case A), which does not contain either gain or loss. This shows that in case C the absorption of the core material has been compensated for.

Finally, a simulation is conducted with only gain material added to the geometry (case D), figure 5.12(d), i.e. the core contains no loss. Here, it is seen that the amplitude of the pulse's intensity rises to a value greater than its initial value. This increase in amplitude seems to stop once the pulse has propagated a certain distance; a result of the decrease in amplitude, (due to the dispersion) counteracting the increase in amplitude (due to the gain).

Using the same method as in the previous sections, the effective refractive index of the propagating pulses in the difference simulations was extracted. The variation of the

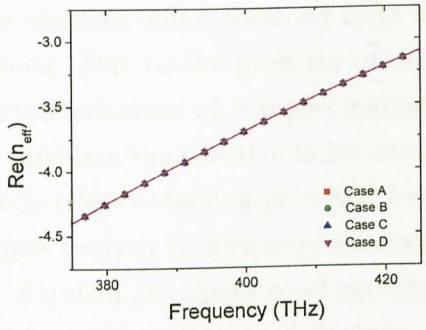

(a) Effect on the real part of effective index of different combinations of gain and loss.

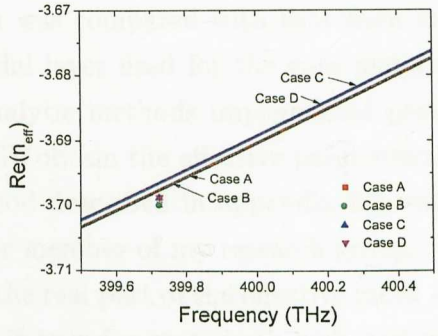

(b) Effect on the real part of effective index of different combinations of gain and loss.

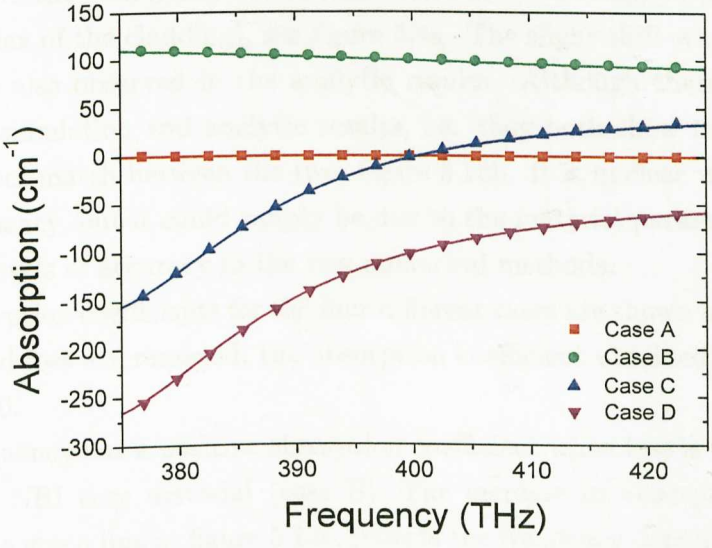

(c) Effect on absorption of different combinations of gain and loss

Figure 5.13: Effect on the real part of the effective index and the absorption of different combinations of gain and loss. Points are from simulation and lines are from the mode solver (calculated by Tim Pickering).

effective refractive index with frequency, the cause of the pulse's dispersion, can be seen in figure 5.13a. As mentioned in section 5.2, in order for the real part of the intrinsic refractive index of the core material to be the same in the situations with and without loss, both the plasma frequency as well as the collision frequency used to define the NRI material were altered when loss was introduced. In these simulations, the intrinsic refractive index of the core at the central frequency is kept as close as possible to -4. As before, the effective index obtained from the simulation was compared with that from analytic results. Due to the presence of the extra material layer used for the gain material and the introduction of complex parameters, the analytic methods implemented previously to calculate the effective index cannot be used. To obtain the effective parameters of the geometries containing gain and loss a new method described in appendix 8.2 was used. These analytic results were generated by another member of my research group.

Figure 5.13a shows good agreement between the real part of the effective index extracted from simulations and analytic results. This is true for cases both with and without loss. As can be seen in figure 5.13b, which focuses on a section of figure 5.13a, there is a small difference between the cases with and without the gain material. This is due to the real part of the gain material's intrinsic refractive index differing slightly from 1 (the refractive index of the cladding), see figure 5.4a. The slight shift when the gain material is inserted is also observed in the analytic results. Although there is good agreement between the simulation and analytic results, i.e. they both show the same trend, there is not a perfect match between the two, figure 5.13b. It is unclear what causes this very slight discrepancy, but it could simply be due to the material parameters being specified to different levels of accuracy in the two numerical methods.

The absorption coefficients for the four different cases are shown in figure 5.13c. When both gain and loss are removed, the absorption coefficient obtained for each constituent frequency is 0.

Each frequency has a positive absorption coefficient when loss is included in the modelling of the NRI core material (case B). The increase in absorption with decreasing frequency, the green line in figure 5.13c, reflects the frequency dependence of the intrinsic absorption of the NRI core material, see figure 5.11a. The fact that the field at lower frequencies is more confined to the core, as shown in figure 5.7, would also enhance the increase of the effective absorption with decreasing frequency.

The most significant simulation is case C, where a gain material is added to compensate for the loss observed in case B. Looking at the profiles of the pulse intensity shows that, when gain is included, the variation in amplitude is very similar to case A (where neither loss nor gain are included). By looking at the absorption spectrum, it can be seen that it is only at the central frequency that the loss is completely compensated

for. At other frequencies there is either a net gain or a net loss. However, since the frequency spectrum for the pulse is peaked at the central frequency, by compensating at this point (and having only small amounts of net loss, or gain, for the frequencies immediately adjacent to it) the intensity profile for the compensated pulse looks similar to the case where no loss or gain is present.

Finally in case D, each frequency contained in the pulse is seen to experience a negative absorption coefficient.

The absorption coefficients calculated using the mode solver for each of the cases are plotted as lines in figure 5.13c. The results found from this method match up precisely with those from the simulations. This agreement gives more confidence in the results obtained using both methods. Figure 5.13c shows one way of passing from the loss to gain regime, which is to vary the frequency of the propagating wave through the waveguide. When both gain and loss are included, case C, a net loss is observed at high frequencies, while at lower frequencies a net gain is observed. The increase in the net gain is due to the increase of the gain material's intrinsic gain. The increase in the intrinsic gain overcompensates for both the increase in the intrinsic loss of the core material and the fact that the field, at lower frequencies, is more confined to the core. Interestingly, as we go from one regime to the other, the negative effective refractive index is maintained, figure 5.13a. This is of note since the ability for a material to have a NRI, whilst having low or complete loss compensation at the same frequency, has been a subject of much discussion [85, 86].

5.7 Extraction of refractive index (complex-frequency)

The effective index values in this and previous chapters have been obtained assuming a complex wavevector, i.e. the change in phase and amplitude of each frequency in the pulse is accounted for by having a complex wavevector. This means that both the phase and amplitude of each frequency component are taken to vary with distance. Obtaining the complex wavevector is a consequence of the extraction method used, i.e. recording the alteration in each frequency component between two separate points along the waveguide.

An alternative method would be to account for the change in phase and amplitude by having a complex frequency. Defining the change in phase and amplitude through this method means these quantities are taken to vary with time rather than distance. Instead of recording the H_z-field at two different spatial points, results are obtained by recording it at two different times. In practice, this means recording the field distribution along the

centre of the waveguide, i.e. at all the points along the central axis at two different times. By Fourier transforming the spatial signal of the pulse, one obtains all the wavevectors present within it. This is opposed to finding all its frequency constituents, as is achieved by Fourier transforming the time signal.

The derivations for the equations that obtain the real and imaginary components of the frequency begin in a similar manner to equation (3.18), except that the temporal variation in the wave is used to relate the two spatial Fourier transformations. Thus:

$$F(k,t_2) = e^{-i\omega t}F(k,t_1). \tag{5.5}$$

A minus sign is used in the relation $e^{-i\omega t}$, in order for it to link with the e^{ikd} term used in equation (3.18). The arguments of the Fourier transformations show that they give the transformations for each wavevector at times t_1 and t_2. As before, it is possible to express the Fourier transformations using the amplitude and phase, though, in this case, it is the amplitude and phase of each wavevector rather than each frequency:

$$A_2e^{i\theta_2} = e^{-i\omega t}A_1e^{i\theta_1}, \tag{5.6}$$

$$\ln(A_2)+i\theta_2 = -i\omega t+\ln(A_1)+i\theta_1, \tag{5.7}$$

$$\ln(A_2)+i\theta_2 = -i(\mathrm{Re}(\omega)+i\mathrm{Im}(\omega))t+\ln(A_1)+i\theta_1, \tag{5.8}$$

$$\ln(A_2)+i\theta_2 = -i\mathrm{Re}(\omega)t+\mathrm{Im}(\omega)t+\ln(A_1)+i\theta_1. \tag{5.9}$$

As previously, the real and imaginary parts can be split up. This gives, for the real component of the frequency:

$$i\theta_2 = -i\mathrm{Re}(\omega)t+i\theta_1, \tag{5.10}$$

$$\frac{\theta_1-\theta_2}{t} = \mathrm{Re}(\omega), \tag{5.11}$$

and, for the imaginary component:

$$\ln(A_2)-\ln(A_1) = \mathrm{Im}(\omega)t, \tag{5.12}$$

$$\frac{\ln(A_2)-\ln(A_1)}{t} = \mathrm{Im}(\omega). \tag{5.13}$$

As with the complex wavevector a computer program was created which used these

equations to extract the complex frequency of the pulse propagating through the waveguide.

5.8 Varying core width

As mentioned in the previous section, varying the central frequency of the pulse is one method of moving from the loss into the gain regime. In this case it is due to the change, with regard to frequency, of the intrinsic loss and gain of the NRI and gain materials.

A second method is to focus on a single frequency, but to vary the width of the waveguide's core. In this case, the intrinsic absorption coefficient of both the NRI core and the gain material remain constant. However, the transverse profile of the mode propagating along the waveguide will vary. The proportion of the field in the two regions, the core and the cladding material, directly relates to the relative amounts of loss and gain experienced by the pulse. In this experiment, as well as calculating the imaginary part of the refractive index through the complex frequency and complex wavevector methods described previously, the energy of the pulse is also recorded.

5.9 Energy box test

An additional output module added to the FDTD code allowed the energy within the simulation to be observed. This module allows a box to be positioned within the simulation. The net amount of energy that enters, leaves and is stored in the EM fields and materials within the box, is then recorded. This diagnostic module is based upon Poynting's theorem, which is the energy conservation law for electromagnetism:

$$\frac{\partial U}{\partial t} + \nabla \cdot S = -Q. \tag{5.14}$$

Here, U is the energy contained in the electromagnetic field within the region, S is the Poynting vector defining the rate of energy transfer into the region, and Q is the amount of work done on charges within the region. The implementation of this module is described in more detail in appendix 8.3.

As with the Drude and Lorentz material models, a 1D simulation was conducted to test the performance of the energy box module. Three different 1D simulations were conducted with the energy box placed close to the injection point in each. The first modelled a pulse propagating through a conventional material, with a refractive index of 4 and no loss present. In the second, a NRI material was used with a refractive index of

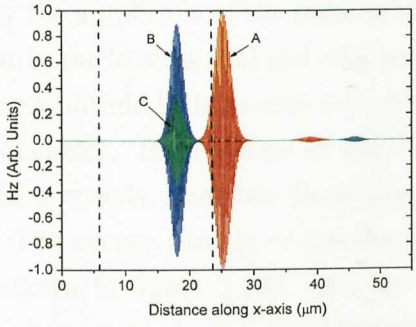

(a) H_z-field amplitude along simulation after 0.475ps. The largest three pulses (A,B and C) are propagating from left to right, the dashed lines denote the edges of the energy box.

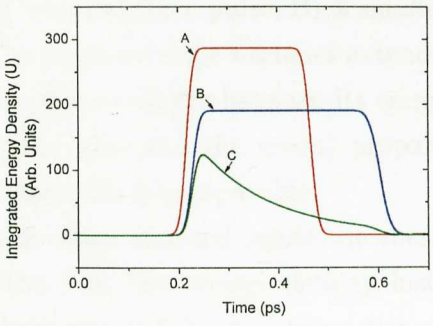

(b) The energy stored in the electromagnetic fields within the energy box

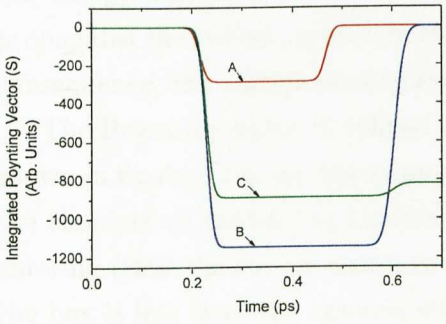

(c) The net Poynting vector directed out of the energy box

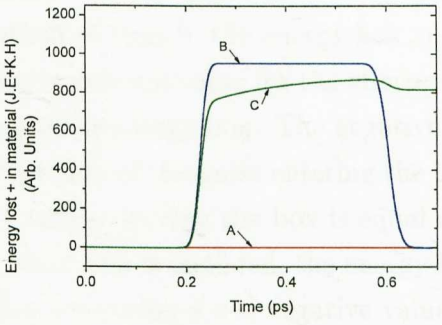

(d) The total energy stored and absorbed by the material situated within the energy box

Figure 5.14: Extraction of parameters using energy boxes. Three different simulations are used containing different materials: (red line, A) A conventional dispersionless material with refractive index 4, (blue line, B) a lossless NRI material with refractive index -4 at the central frequency and (green line, C) a NRI material with loss and a refractive index of -4 at the central frequency.

-4, again, without any loss. In the third case, loss was added to the NRI material. The results are shown in figure 5.14

A snapshot of the propagating plane wave pulses is shown in figure 5.14a. The three larger pulses are propagating from left to right. Since a NRI material is used in two of the simulations, periodic boundaries are implemented at the highest and lowest x-axis points. As the main pulses were injected, smaller pulses were found to be created which propagated in the opposite direction to the main pulse. Due to the periodic boundary these pulses are observed on the right of figure 5.14a and propagate from left to right.

The pulse created in the conventional PRI material was be observed to propagate faster than pulses in the NRI, see figure 5.14a. This is due to the presence of dispersion in

the NRI material, while the PRI material used is dispersionless. Dispersion also explains why the amplitude of the pulse in the lossless NRI material (blue pulse, B) is smaller than that in the lossless PRI material (red pulse, A). The pulse envelope becomes extended and the amplitude is decreased due to the variation in phase velocity between its component frequencies. Both pulses in the NRI materials (the blue and the green) propagate at similar speeds, since the dispersion of these two materials is comparable.

The energy density of the electromagnetic fields when situated inside the energy box is shown in figure 5.14b. As the pulse enters the box, the energy density inside the box increases. In the simulations where a lossless material is used once, the pulse is completely contained within the box and the energy density stays constant. In the case of the material containing loss the energy density in the field decreases, even while the pulse is still fully inside the box. When the pulse leaves the energy box, reassuringly, the energy density within the energy box decreases. As the pulse in the PRI material propagates the fastest, it spends the shortest amount of time in the energy box and, as a consequence, the energy density extracted is at its maximum value for the shortest time.

The Poynting vector is defined as pointing out of the energy box. The negative values shown in figure 5.14c are therefore due to the energy flux of the pulse entering the box. In the simulations containing lossless materials, the energy leaving the box is equal to that entering (thus the curves return to 0). However, when loss is included, the energy leaving the box is less than the amount which enters, thus producing a net negative value.

The energy absorption calculated using the J·E and K·H terms (see appendix 8.3) is shown in the final figure 5.14d. This should show the energy which goes into doing work on the material and is therefore lost from the pulse. However, since in the FDTD code the response of the NRI materials is implemented by using the electric and magnetic current densities, the terms J·E and K·H account for energy both stored in the NRI material, as well as lost to it. This is demonstrated by the fact that these terms are non-zero when a lossless NRI material is modelled (blue curve - figure 5.14d). However, in the case of the PRI material, neither the electric nor magnetic current densities are used and so in this lossless situation, the zero energy lost is actually recorded as being zero.

In summary, the parameters extracted using the energy balance module seem to behave as expected in the test simulations. It should be noted that in the calculation of the energy loss and the energy velocity, the absolute magnitude of the energy density is not required. Therefore, the value of the energy density has been kept in arbitrary units.

Following this successful test this module was used in the investigation of the effect of varying the width of the waveguide's core.

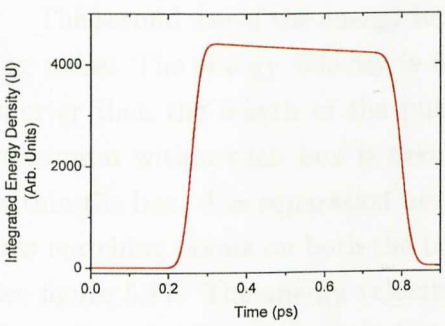

(a) Change in energy density of pulse in waveguide with core width 300nm

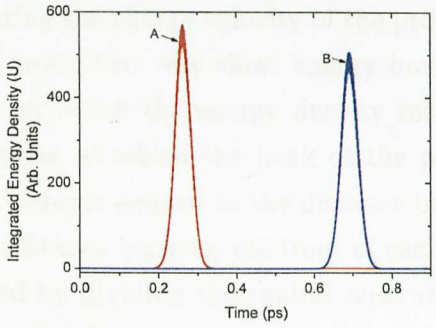

(b) Energy density recorded in two short energy boxes. Box 1 (red line) is positioned approx 0.14μm in front of box 2 (blue line).

Figure 5.15: The methods used to extract the energy loss and energy velocity from the waveguide simulations.

5.10 Using the energy box

In this work the energy box is used in two different ways. The first is to calculate the energy loss of the pulse. This is done by defining a very large box which can encompass the whole of the propagating pulse. It is then possible to see the energy loss experienced by the pulse by observing the change in energy contained in the electromagnetic fields. Note, care needs to be taken, since in the present version of this energy module the energy lost to the NRI material and the energy stored in the NRI material cannot be distinguished. However, once the pulse has completely entered the energy box any change in the energy content of the box while the pulse is still completely enclosed can be defined as being due to material loss, see figure 5.15a. The significant advantage of using this module is that it allows the energy lost from all the frequencies comprising the pulse to be recorded; not just that of the central frequency.

The decay constant of the pulse is extracted by recording the energy density at two time points, U_1 and U_2, during the time when the pulse is fully inside the energy box. Thus, by taking the difference in the energy density of the pulse at those two points, and their time separation, Δt, the decay constant can be found using the equation:

$$U_2 = U_1 e^{-g\Delta t}, \tag{5.15}$$

$$\ln(U_2) = \ln(U_1) - g\Delta t, \tag{5.16}$$

$$g = \frac{\ln(U_1) - \ln(U_1)}{\Delta t}. \tag{5.17}$$

In the simulations the length of this large box is 18.375μm.

The second use of the energy box is in calculating the energy velocity of the propagating pulse. The energy velocity is found through using two very short energy boxes, i.e. shorter then the length of the pulse. The time at which the energy density reaches a maximum within each box is taken to be the point at which the peak of the pulse is within the box. The separation between the two boxes is defined as the distance between two matching points on both the boxes (i.e. the distance between the front of each box), see figure 5.17. The energy velocity is then found by dividing the spatial separation by the temporal delay. In the simulations the length of each of these two boxes is 206.25nm.

5.11 Varying core width - simulations

To produce the FDTD results for the effect of core thickness, a set of simulations were conducted with a range of thicknesses from 202.2nm up to 300nm. All these thicknesses are larger than that which is predicted to stop the pulse. This limitation was made, since, in order to obtain results for the complex wavevector and energy velocity, it is necessary for the pulse to be propagating (so that it can pass over the measurement points and through the energy boxes). In addition, a propagating pulse is necessary since the same injection method is used for these simulations as in section 4.3, i.e. using a TFSF plane and shaping the transverse distribution of the fields to match that of the desired mode. As a consequence, if the pulse was stationary it would never leave the vicinity of the injection plane.

5.12 Varying core width - results

The effect of the core width on the decay of the pulse is calculated through five different methods. The first three are the complex wavevector, the complex frequency and the total energy decay found using the FDTD method. The other two, are the complex wavevector and complex frequency, found using the analytic approach, see appendix 8.2. To enable the results of these different methods to be compared, the absorption found from each is converted into units of s^{-1}. In practice this means that the complex wavevector results are multiplied by the group velocity. In the case of the FDTD results, the energy velocity was used in the conversion. For the analytic results, the group velocity, calculated using the complex wavevector, was used. The results are shown in figures 5.16a , 5.16b and 5.17. Due to the difficulties described earlier, FDTD simulations are only conducted for core thicknesses larger than that at the stopped light point. For thicknesses closer to the stopped light point only the results from the analytic method are available.

Figure 5.16a displays the results from the 5 different methods at the larger core thicknesses, at which all 5 methods are implemented. To make it easier to plot the results, the absolute value of absorption is used. The black dashed line positioned at a core thickness of 262.9 nm denotes the boundary between the loss and gain regimes. Encouragingly, there is good agreement between the complex frequency and wavevector results for the pulses' central frequency, calculated using both the analytic and FDTD methods. This acts as a good check for both methods. As mentioned previously, both methods show that when the thickness of the core is reduced below 262.9nm, the central frequency experiences gain rather than loss. As predicted, this is due to the excited backward mode excited having a greater proportion of its field in the cladding and gain material, as opposed to the core, where the loss is situated.

The one set of results which show a slight discrepancy from the others is that denoting the change in energy of the pulse as a whole, the purple triangles in figure 5.16a. These results show that the thickness at which the pulse as a whole starts to experience gain is slightly greater than that at which the pulse's central frequency does. This is due to the fact that the different frequencies which comprise the pulse experience total loss compensation at different core thicknesses. This is a result of the variation with frequency of both the proportion of the mode in the different regions of the waveguide, and the intrinsic gain and loss experienced by each frequency in the gain and the NRI core materials. The change in energy of the pulse is thus found by summing the loss and gain experienced by all the frequencies in the pulse.

The analytic results were extended by another member of my group to the core thicknesses at which the pulse's central frequency is expected to be stopped, figure 5.16b. As can be seen, up until close to this degeneracy point the absorption coefficients (calculated using both the complex frequency and complex wavevector methods) agree. However, at very small values of group velocity the two sets of results diverge. As seen in figure 5.17, when the group velocity at the central frequency is plotted, this divergence seems to be due to the use of the group velocity calculated using the complex wavevector results to convert between the two. Whereas with the complex frequency the group velocity goes to zero, the group velocity calculated using the complex wavevector reaches a minimum of 0.0216c.

The group velocity is calculated from the complex frequency and complex wavevector results using the relation:

$$\nu_g = \frac{\partial \omega}{\partial k}, \tag{5.18}$$

with the real frequency component and the real wavevector component used in each case.

These results agree with the claims made in [65, 64] and [37] that, when loss or gain is included, the zero group velocity point calculated using the complex wavevector disappears. As shown in [65], if complex frequency is used to analyse the results, then the degeneracy point remains despite the presence of loss or gain in the geometry.

The method of using the two energy boxes to calculate the energy velocity of the pulse is found, as can be seen in figure 5.17, to give the same value as the group velocities found using the complex frequency and wavevector of the analytic methods.

5.13 Varying intrinsic gain of gain material

Although loss compensation was achieved in the previous sections due to the shape of the intrinsic loss and gain material, this compensation only occured at a single frequency. As a final piece of work on loss compensation, the feasibility of adjusting the shape of the effective loss/gain distribution experienced by the pulse through altering the intrinsic gain distribution of the gain material was investigated. The aim was to create a flat loss distribution with each frequency experiencing the same amount of loss or gain. The method of achieving this was to first calculate the effective loss at each frequency, and then to use the confinement ratio to calculate the intrinsic gain required at each frequency to compensate for this loss.

In these simulations the core width was set to 225nm, the width of the gain material to 187.5nm and the distance between the outer edge of the gain material and the PML to 750nm. As before, the central frequency of the pulse is 400THz and the length of the pulse is set so as to excite a bandwidth of (370-430)THz. In this section slightly different gain and loss parameters were used. Initially, the parameters of the gain material were set as $\epsilon_\infty = 1.001290$, $\omega_p = 2\pi \times 370.342$THz, $\Gamma_e = 100$THz and $\Delta\epsilon = -5.154634 \times 10^{-3}$. The collision frequency in the NRI material was set as $0.000458\omega_p$, giving an intrinsic refractive index at the central frequency of $\mathrm{Re}(n) = -3.9999$ and $\mathrm{Im(n)} = 0.00425$. The confinement ratio was calculated by conducting a simulation containing only the gain material and, then, as in section 5.4, taking the ratio between the effective and intrinsic gain.

The effective gain produced using the initial gain material parameters is shown in figure 5.18(C). Also shown in figure 5.18 is the effective loss experienced by the pulse when the gain material is omitted (A), and the effective gain it experiences when the loss and gain material are present (B). When both the gain and the loss are present there is a large variation in the absorption coefficient experienced by frequencies comprising the pulse.

Using the confinement factor calculated from the simulation of the waveguide contain-

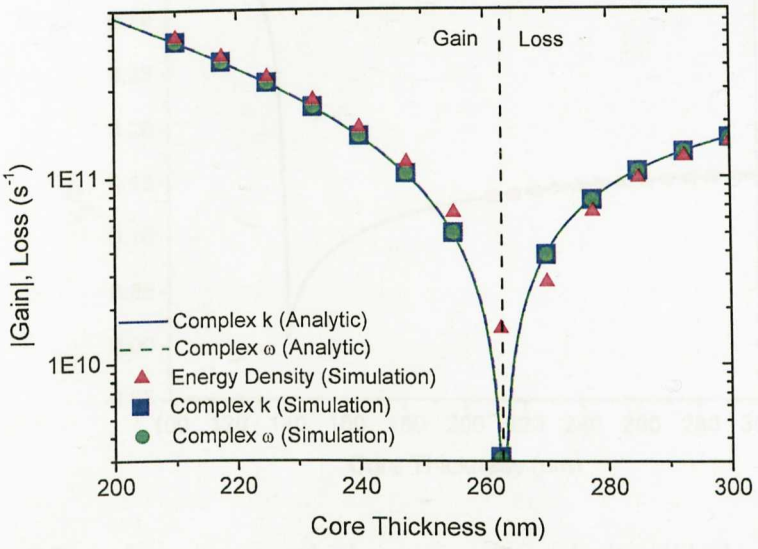

(a) Effect on gain and loss of varying core thickness. Analytic mode solver results (obtained by Tim Pickering) are shown as lines: complex wavevector (green line), complex frequency (blue dashed line). The FDTD simulation results are given as points; complex wavevector (blue squares), complex wavevector (green circles) and energy density (pink triangles).

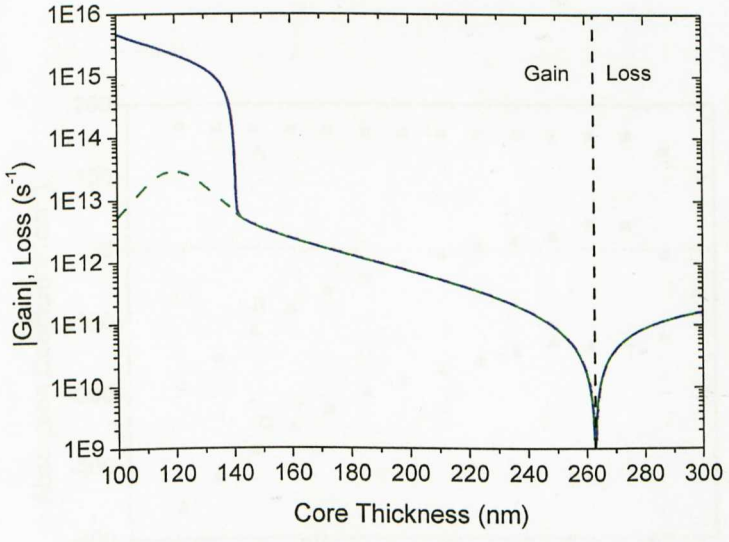

(b) Effect of thickness on gain and loss extracted. Results (obtained by Tim Pickering) calculated using analytic mode solver are shown; complex wavevector (Blue solid line) and complex frequency (Green dashed line).

Figure 5.16: Effect of varying core thickness on gain and loss

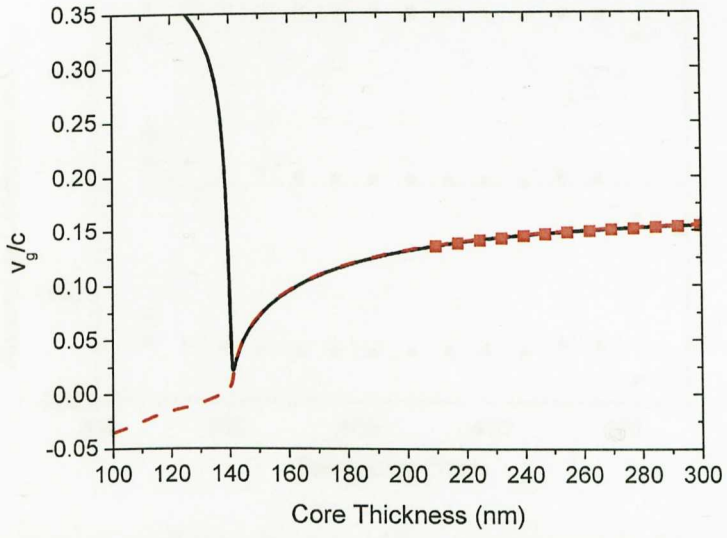

Figure 5.17: Effect of varying core thickness on group velocity. (black solid line) group velocity calculated using complex wavevector analytic mode solver results, (red dashed line) group velocity calculated using complex frequency analytic mode solver results (mode solver results obtained by Tim Pickering) and (red squares) the energy velocity found from the simulations.

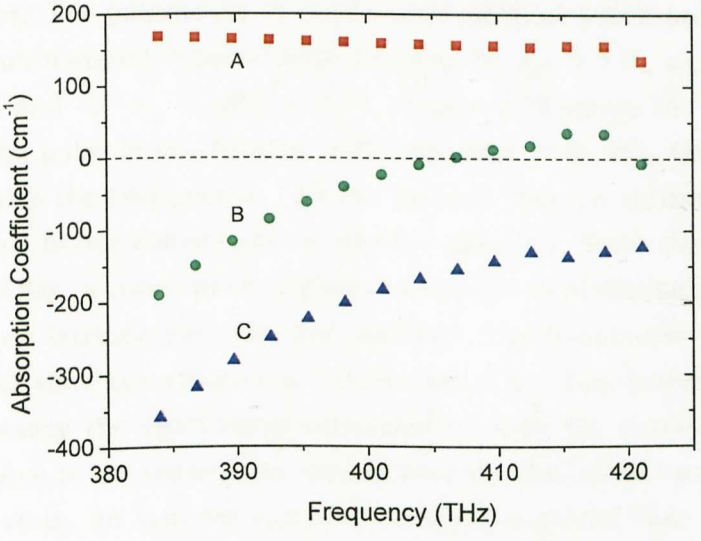

Figure 5.18: Initial absorption coefficients: A) only loss is present, B) loss and gain are present and C) only gain is present

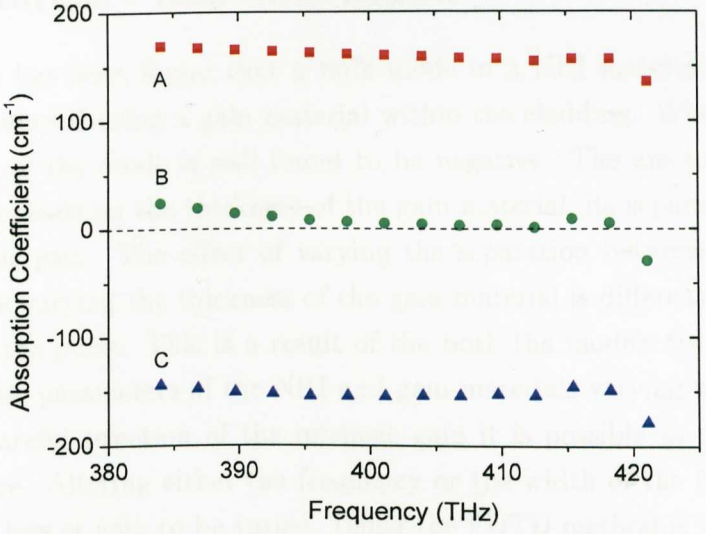

Figure 5.19: Absorption coefficient with modified gain material: A) only loss is present, B) loss and modified gain are present and C) only modified gain is present.

ing the gain material and no loss, figure 5.18(C), the relationship between the intrinsic gain of the gain material and the effective gain experienced by the pulse can be found. To compensate the pulse, the value of the effective gain must be the inverse of the effective loss. Once the effective gain required is obtained, the confinement factor can be used to find the intrinsic gain needed to produce that effective gain. The parameters of the Lorentz material which produced the required intrinsic gain was calculated using a numerical solver. The parameters of the Lorentz material which produce the best fit to the intrinsic gain material required were found to be $\epsilon_\infty = 1.0$, $\omega_p = 2\pi \times 376.56\text{THz}$, $\Gamma = 265.5\text{THz}$ and $\Delta\epsilon = -3.4866 \times 10^{-3}$. Figure 5.19 shows the effective absorption coefficient of the pulse in simulations; with only loss; with only the new gain material present; and with the two present. As can be seen the new intrinsic gain distribution produces a much flatter distribution of effective gain (C). Since the effective loss distribution is quite flat, a much more uniform absorption distribution is created when the loss and this new intrinsic gain are used together. The frequencies were not completely compensated for since the absorption distribution of the gain material implemented did not match precisely the distribution calculated in order for complete compensation to occur. This is due to the parameters used to describe the Lorentz material having limits imposed upon them, for instance ϵ_∞has to be equal or greater than 1.

Even though complete loss compensation was not achieved, this section does show how varying the frequency dependence of the gain material can allow the frequency dependence of the absorption experienced by the pulse to be varied.

5.14 Summary and conclusion

In summary it has been found that a bulk mode in a NRI material waveguide can be evanescently pumped using a gain material within the cladding. When this is done, the effective index of the mode is still found to be negative. The amount of gain supplied to the mode depends on the thickness of the gain material, its separation from the core, and its intrinsic gain. The effect of varying the separation between the core and gain material and of varying the thickness of the gain material is different for each frequency component of the pulse. This is a result of the both the mode's transverse field profile and the intrinsic parameters of the NRI and gain materials varying with frequency.

Through careful selection of the intrinsic gain it is possible to compensate for loss in the NRI core. Altering either the frequency or the width of the NRI waveguide core allows the net loss or gain to be varied. Using the FDTD method it is possible to obtain complex-frequency results in addition to the complex-wavevector. It was found for pulses travelling at the group velocities investigated that the results produced, using the complex wavevector method which are displayed in units of one over meter, could be converted into units of one over second using the energy velocity calculated from the simulations. Good agreement was found between these converted complex wavevector results and the complex frequency results (obtained directly from the simulation). The FDTD results also agreed well with those produced using an analytic method.

When the total energy of the pulse was recorded, the core thickness at which total loss compensation occurs did not match that found for the central frequency. This is a result of the total gain experienced by frequencies below that of the central frequency being greater than the total loss experienced by frequencies above the central frequency.

In conclusion, it seems, that, provided a gain material with sufficiently high intrinsic gain can be obtained, it should be possible to compensate for the loss in a NRI waveguide, whilst retaining the negative phase velocity of modes propagating through that structure. The maximum effective gain can be achieved by placing the gain material as close to the core as possible, and using as wide a strip of material as possible.

Chapter 6

Prism coupling

6.1 Introduction

In this chapter the stopped light mode is analysed. This is different to previous chapters where slow light modes are examined. The stopped light mode can be probed through the use of a prism to couple light into the NRI waveguide which allows the stopped light mode to be excited directly. This is in contrast to the tapered waveguide structure where a slow light mode is initially injected and then is gradually slowed as it propagates along the taper.

The geometry simulated is that investigated in [50]. Using additional methods to analyse the pulse in this geometry new features of the pulse's behaviour are discovered. The wavelengths examined are much longer than those used in previous chapters, in order to allow direct comparison with the results of [50]. The results obtained, however, should still be applicable when scaled down to the optical regime.

This chapter is set out as follows. First, the mechanism behind prism coupling is discussed. Second, the geometry implemented and the parameters used for the injection beam are detailed. Third, the resolution and Courant values required for the simulations are identified, as in chapters 4and 5. Fourth, effects of removing the prism from the simulation geometry are analysed. Fifth, different methods are used to examine the effects of varying the angle of the source beam. Last, an attempt is made to excite the stopped light mode.

6.2 Prism coupling

Light is confined inside a dielectric waveguide when its longitudinal wavevector in the waveguide is greater than its total wavevector in the cladding material. This is achieved if the refractive index of the core is larger than that of the cladding. As a consequence of

this, the light's transverse wavevector in the cladding is imaginary and hence the light's EM-field evanescently decays as it extends away from the waveguide core. In addition to confining the light, this condition prevents light beams which are propagating in the cladding material from exciting bound modes in the waveguide. However, bound modes can be excited using a prism composed of a high refractive index material placed next to the waveguide. This coupling is achieved by totally internally reflecting the light beam off the edge of the prism which lies parallel to the waveguide. An evanescent field is generated extending from the prism and intersecting with the waveguide, see figure 6.1. The longitudinal propagation constant of this evanescent wave can be made to match that of the desired bound mode with the correct choice of: the source beam's frequency; the angle of incidence; and the prism's refractive index. These three factors are related to the longitudinal propagation constant through the equation:

$$\beta = \mathrm{n}_p k_0 \cos(\theta), \tag{6.1}$$

where n_p is the refractive index of the prism and the angle θ is defined in figure 6.1.

Using a prism to excite the stopped light mode has advantages over the tapered waveguide geometry. The most apparent improvement is that it shortens the length of waveguide required as a gradual taper is not needed. Prism coupling also makes it easier to excite the mode desired. The choice of mode is no longer limited to those which have profiles and impedances which allow them to be launched into the NRI waveguide from a conventional PRI waveguide [17]. Perhaps most importantly, using a prism coupling method negates the back coupling issues highlighted in [49]. By coupling directly to the stopped light mode the pulse excited should remain stationary, unlike that observed in tapered waveguides [38, 52].

The use of prism coupling in separating forward and backwards modes was mentioned in [47]. Once excited in the waveguide, the forward and backward modes will travel in opposite directions (provided the direction of the propagation vector is the same in both). Prism coupling into the stopped light mode was extensively investigated by Bai *et al* [50]. They demonstrate the possibility of coupling to a forward, backward and stopped mode using FDTD simulations. The need for the prism to be removed once light has been injected into the waveguide is also shown. This prevents light from coupling out of the waveguide and radiating into the cladding.

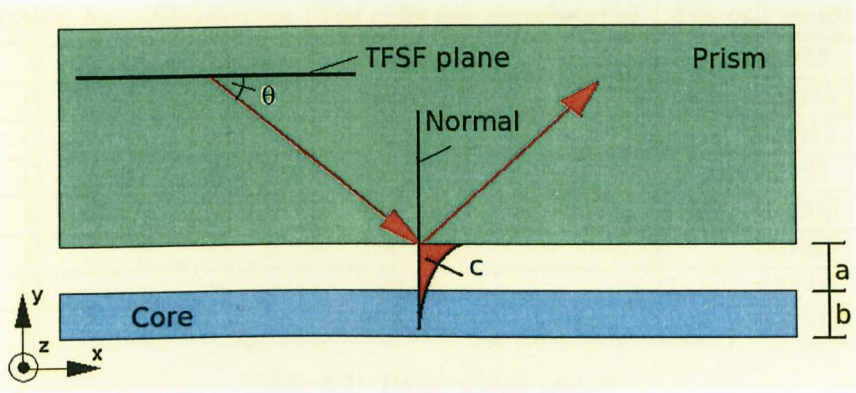

Figure 6.1: Geometry modelled, consisting of a prism composed of a conventional PRI material (green) situated next to a waveguide with core composed of a NRI material (blue). Both are embedded in air (yellow). The thickness of both the gap between the prism and the waveguide (a) and the width of the waveguide (b) is 3cm. A representation of the evanescent field used to couple the light to the prism is also shown (c).

6.3 Prism geometry and source

As stated in section 6.1, the geometry simulated is similar to that implemented by Bai *et al.* As in [50], the width of the waveguide core is 3cm, as is the separation between the prism and the core, see figure 6.1. The two ends of the waveguide are terminated by a NRI material / air interface. The whole geometry is surrounded with a PML boundary to absorb any radiation incident upon it. The NRI material comprising the core is simulated using a double Drude, lossless model, with the plasma frequency set to 10GHz; identical to that used by Bai *et al.* The refractive index of the prism is 2.235 and this material is modelled as being dispersionless. A TFSF plane, positioned inside the prism is used to generate the source beam. By using the TFSF plane it is possible to select the angle at which the beam propagates away from the injection plane θ. In this work the TM_4 mode is excited. The transverse profile of this mode has four nodes in the core. Both the source frequency and the angle θ are varied and are specified later.

6.4 Source profile

For each mode the stop light point exists for a single value of wavevector and frequency only. To reduce the excitation of wavevectors and frequencies around the stopped light point (which have a non-zero group velocity) the source should have as narrow a bandwidth and as small a range of wavevectors as possible. In addition, the pulse excited in the waveguide should have as short atableial extension along the x-axis as possible. Having a small spatial extension allows any movement of the pulse along the waveguide

Simulation No.	Resolution (Yee cells per wavelength)	Yee cell length (m)
A	34.18	0.002
B	45.57	0.0015
C	56.96	0.0012
D	68.35	0.001
E	113.92	0.0006
F	136.70	0.0005
G	170.88	0.0004
H	227.84	0.0003

Table 6.1: Resolutions tested

to be clearly observed and would increase the time taken for the pulse to reach the end of the waveguide (if it was found to move).

To reduce the bandwidth, a sustain was used in the source beam. The source beam's attack/decay was set to 3ns and its HWHM to 0.6ns. Once the amplitude had reached its maximum value (defined as 1) the amplitude was sustained at this value for 30ns. Following this the amplitude was then slowly reduced to 0 over a period of 3ns (the decay), in a symmetrical manner to its attack.

To minimise the spread of wavevectors, the variation in the beam's angle of incidence had to be kept as small as possible. To ensure the ends of the TFSF plane did not act as point sources and so excite circular waves (propagating along a large range of angles and thus containing a large range of wavevectors), the profile of the beam's phase fronts was made non-uniform. By using a Gaussian shape for the transverse profile, the field at the ends of the injection plane could be made very small.

Following this, the optimum width of the Gaussian curve used for the transverse profile had to be determined. The narrower the Gaussian distribution the greater the phase front resembled a point source, see figure 6.2a. This would both increase the range of wavevectors contained in the excited pulse and produce an asymmetric distribution, as shown in figure 6.2b. However, by widening the profile of the source the spatial extent of the pulse is increased, as shown in figures 6.3a and 6.3b. After testing, a value of 0.1472m was chosen for the HWHM value. This produced a good balance between the two rival effects.

6.5 Effect of resolution

As in previous chapters, the effect the resolution used has on the simulation results was examined. The resolutions tested and the lengths of the Yee cells these produce are detailed in table 6.1.

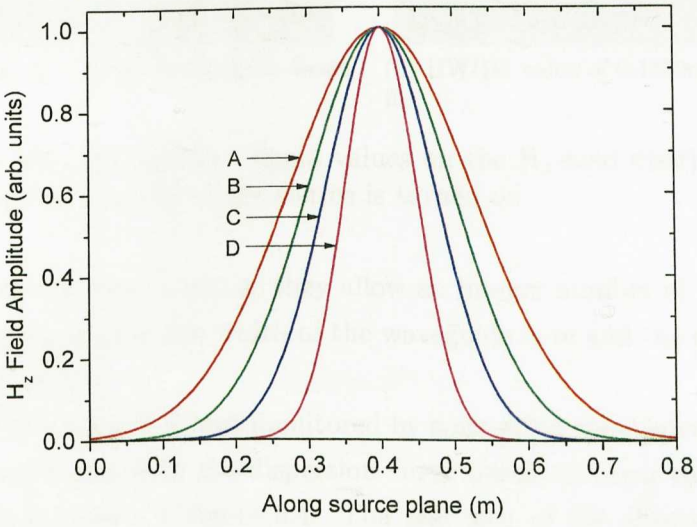

(a) Variation of H_z-field profile of source with sigma value.

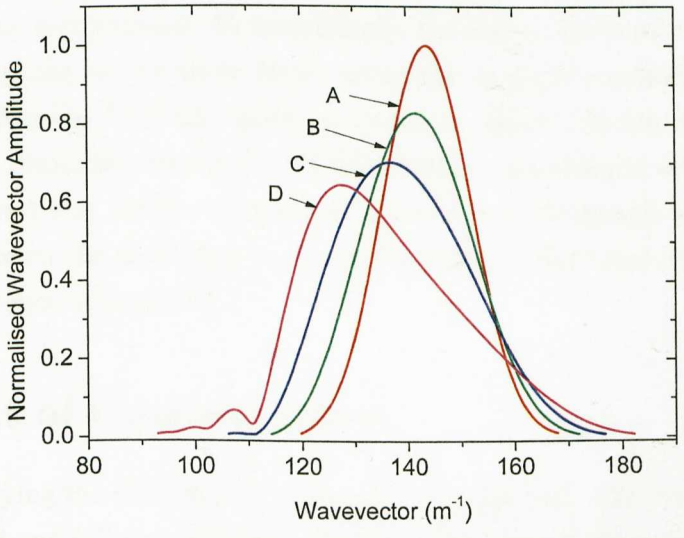

(b) Variation in wavevector distribution of excited pulse with different sigma values.

Figure 6.2: Effect on H_z-field profile and wavevector distribution of using HWHM values of A) 0.1472m B) 0.1177m C) 0.0883m and D) 0.0589m

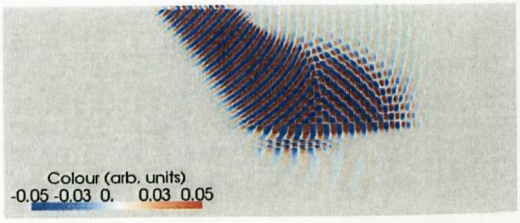

(a) HWHM value of 0.0589m is used for beam profile.

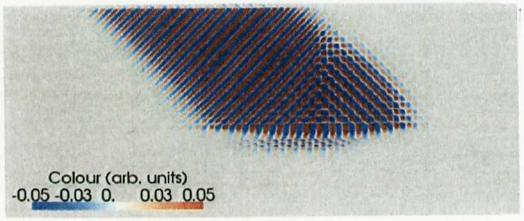

(b) HWHM value of 0.1472m used for beam profile.

Figure 6.3: The effect of different sigma values on the H_z-field distribution in both the prism and waveguide 2.1ns after the source is turned on.

These resolutions were chosen as they allow an integer number of Yee cells to fit into a 3cm length, which is both the width of the waveguide core and the separation between the core and the prism.

The effect of the resolution was monitored by comparing the dispersion curves extracted from the simulations with the dispersion curve obtained using the analytic method. This comparison is shown in figure 6.4. The real part of the effective refractive index was obtained using the temporal extraction method, see section 5.7. The delay between the two snap-shots used is smaller than the period of the central frequency. As figure 6.4 demonstrates, the resolution does have an impact on both the position and the shape of the dispersion curve calculated. Unsurprisingly, the higher the resolution used the closer the simulation results are to those found using the analytic method. The resolution is also found to affect the H_z-field values, as shown in figure 6.5a and 6.5b. As a result of this, the highest resolution tested (227.84 Yee cells per wavelength, which gives a Yee cell length of 0.0003m) was used in subsequent simulations. Although there is still a slight discrepancy between the dispersion curve produced using this resolution and the analytic results the difference is negligible.

6.6 Effect of Courant value

The effect of varying the Courant value was also investigated. The results produced using values of 0.5, 0.6 and 0.7 were assessed. Unlike in the case of the resolution, the Courant value has a very small effect on the simulation results, as demonstrated in figure 6.6. In subsequent simulations, the Courant value was set to 0.7.

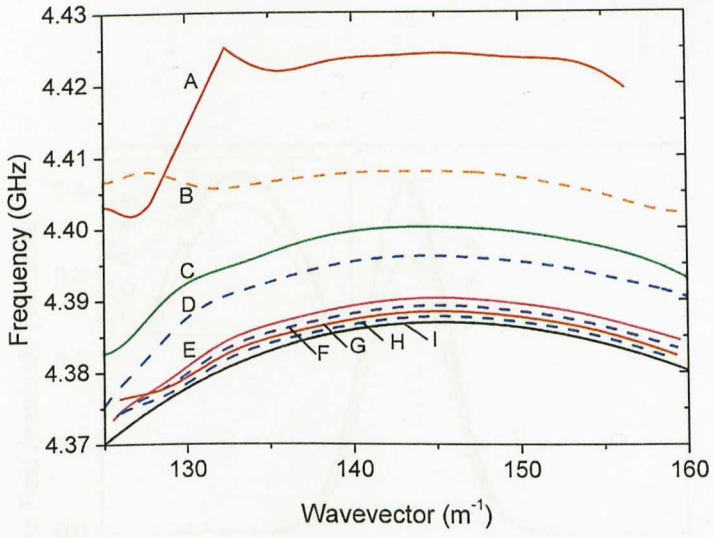

Figure 6.4: Effect of resolution on dispersion curve. Yee cells of length A) 0.002m, B) 0.0015m, C) 0.0012m, D) 0.001m, E) 0.0006m, F) 0.0005m, G) 0.0006, and H) 0.0003 were used. The dispersion curve calculated using the analytic method is also included, I).

6.7 Removing the prism

Placing a prism next to the waveguide not only allows light to couple into the waveguide, but also enables light in the waveguide to radiate into the surroundings. Therefore, to ensure the light is confined inside the waveguide the prism has to be removed once the light has been injected [50]. When modelling the removal of the prism, two simulations were conducted. The geometry of the first contained the prism and simulated the injection of the light into the waveguide. This simulation was then stopped and the final E- and H-field values, along with the polarisation and magnetisation values at each point within it, were recorded. These values were then used for the initial parameters in the second simulation. However, in this second simulation, the refractive index of the prism was changed to 1 (i.e. the same as the rest of the cladding) and the source was turned off. Running this simulation thus showed the behaviour of light in a geometry with no prism close to the waveguide.

To avoid a large field intensity being present in the prism when it is removed, the source was switched off before the end of the first simulation. In total, the source is active for 36ns (including the attack and decay periods). However, before removing the prism, sufficient time must be allowed for the end of the source beam to be reflected off the lower edge of the prism and then exit the simulation geometry at the upper PML.

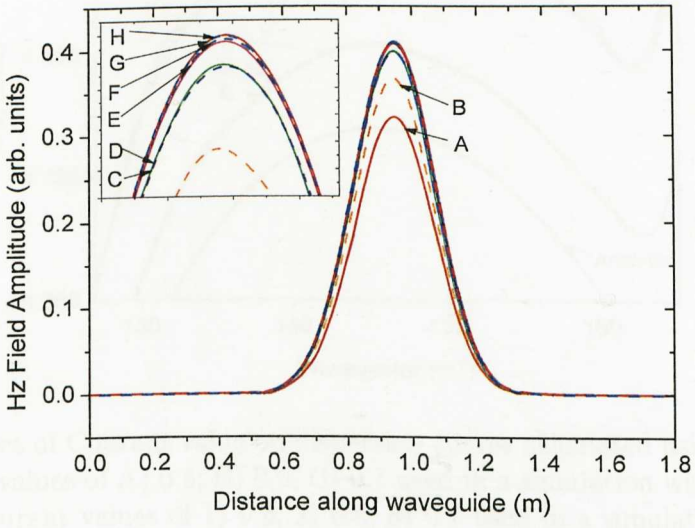

(a) 15ns after start of simulation

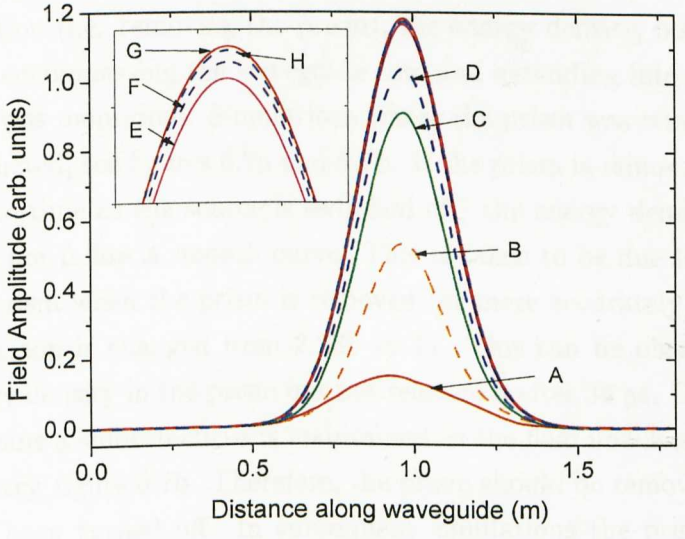

(b) 39.99ns after start of simulation

Figure 6.5: Pulse envelopes calculated using the H_z-field obtained from simulations using Yee cells of length A) 0.002m, B) 0.0015m, C) 0.0012m, D) 0.001m, E) 0.0006m, F) 0.0005m, G) 0.0004m, and H) 0.0003.

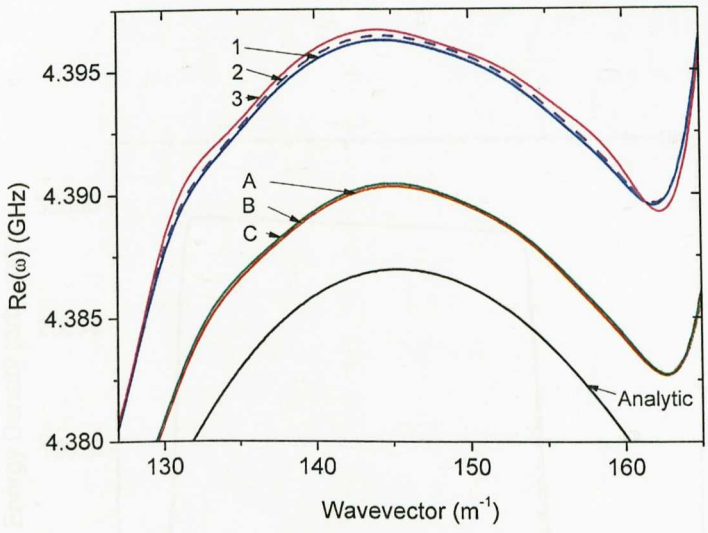

Figure 6.6: Effect of Courant value on dispersion curves calculated using different resolutions. Courant values of A) 0.5, B) 0.6, C) 0.7 used in a simulation with a Yee cell length of 0.0006m. Courant values of 1) 0.5, 2) 0.6, 3) 0.7 used in a simulation with a Yee cell length of 0.001m

To determine the minimum delay required between turning off the source and ending the first simulation (i.e. removing the prism), the energy density, both within the prism and in a region encompassing the waveguide core and extending into the air immediately surrounding it, was monitored. Simulations where the prism was removed after 36ns and 38ns were conducted, see figures 6.7a and 6.7b. If the prism is removed after 36ns (i.e. at exactly the same time as the source is switched off) the energy density in the two areas monitored does not follow a smooth curve. This is taken to be due to an EM-field being present in the prism when the prism is removed (or more accurately when the refractive index of that region is changed from 2.235 to 1). This can be observed in figure 6.7a, where the energy density in the prism has not reached 0 after 36 ns. Delaying the removal of the prism means a smooth curve is maintained as the field now has time to completely leave the geometry, figure 6.7b. Therefore, the prism should be removed at least 2ns after the source has been turned off. In subsequent simulations the prism is removed after 50ns.

It should be noted that in these simulations the removal of the prism happens instantaneously. This is impossible in any experimental realisation, where the separation between the prism and the waveguide would increase during a finite period. However, since only a negligible amount of the field is left in the prism when it is removed the unphysical nature of its removal should make little difference.

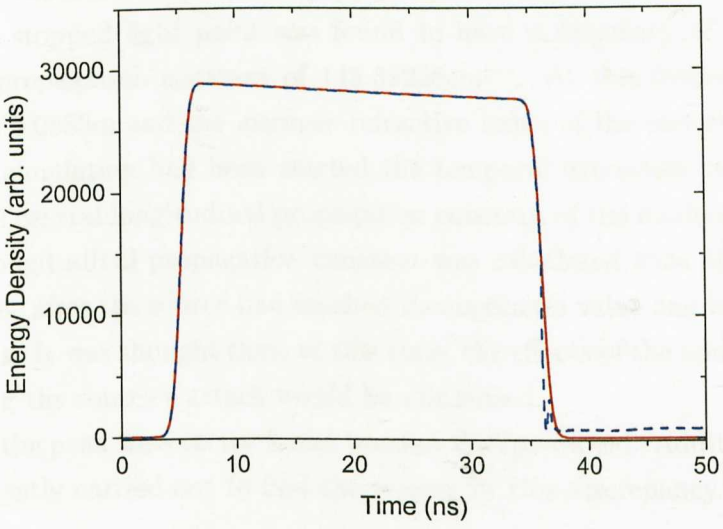

(a) Variation in energy density within prism.

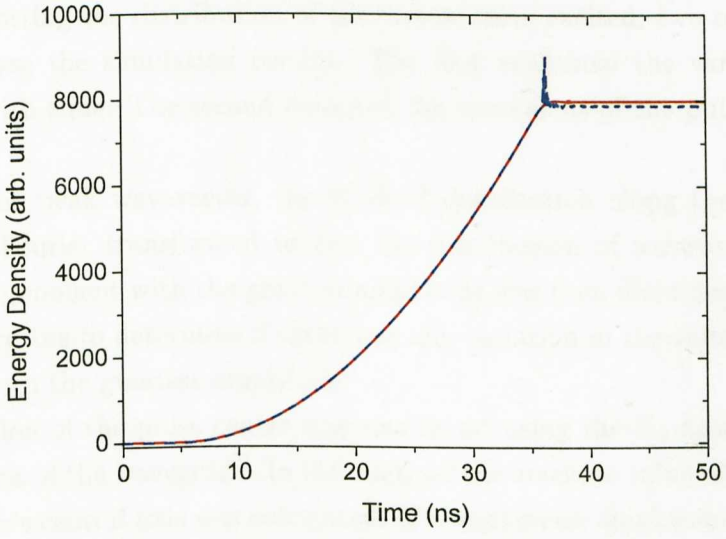

(b) Variation in energy density in and around waveguide core.

Figure 6.7: Effect on the energy density in the prism and the waveguide of removing the prism at a later time. Prism removed after 36ns (dashed line), prism removed after 38ns (solid line).

6.8 Exciting stopped light mode

Analytic results show that the presence of the prism affects the waveguide's dispersion curves. In the first simulation conducted, the frequency and wavevector values chosen for the source matched those of the stopped light mode in the core when the prism was present. The stopped light point was found to have a frequency of 4.38697GHz and a longitudinal propagation constant of 145.38226cm^{-1}. At this frequency the free space wavelength is 0.0683m and the intrinsic refractive index of the core material is -4.19602.

Once the simulation had been started the temporal extraction method was used to determine the central longitudinal propagation constant of the mode excited in the waveguide. The longitudinal propagation constant was calculated 15ns after the start of the simulation, i.e. after the source had reached its maximum value and had a constant amplitude for 12ns. It was thought that, at this time, the effects of the additional wavevectors excited during the source's attack would be minimised.

However, the peak wavevector found was not that predicted. Additional investigations were subsequently carried out to find the reason for this discrepancy.

6.9 Analysing results

As well as plotting the distribution of the wavevectors excited, two other methods were used to analyse the simulation results. The first examined the variation of the peak wavevector with time. The second recorded the movement of the pulse centre along the waveguide.

To find the peak wavevector, the H_z-field distribution along the waveguide's central axis was Fourier transformed to give the distribution of wavevectors present. The wavevector component with the greatest amplitude was then identified. This process was repeated every 1ns to determine if there was any variation in the value of the wavevector component with the greatest amplitude.

The position of the pulse centre was also found using the H_z-field distribution along the central axis of the waveguide. In this method the absolute value of each H_z-field along the waveguide's central axis was calculated. The maximum amplitude of each phase front was then found. A line could then be fitted between these points to produce the pulse envelope. The position of the envelope's maximum value was taken to be the centre of the pulse.

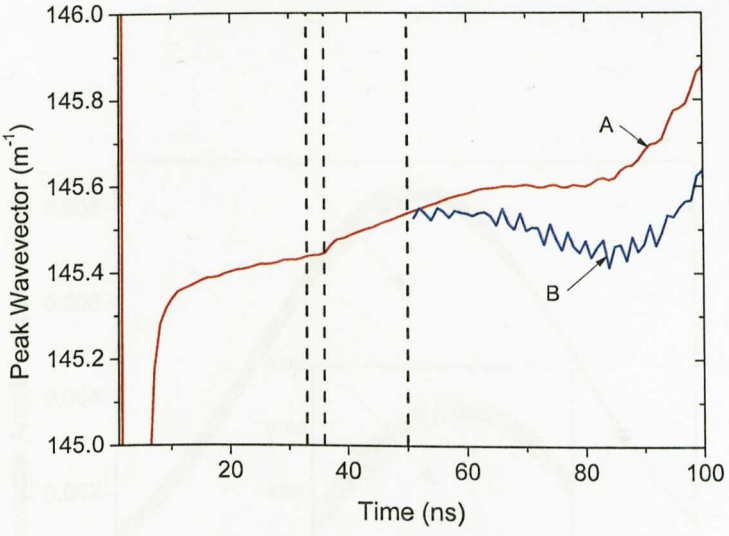

Figure 6.8: Variation of the excited pulse's peak wavevector with time. Red line (A) shows the situation where the prism is not removed and the Blue line (B) shows the situation where it is removed. The dashed lines are placed at 36ns, 38ns and 50ns after the start of the simulation.

6.10 Wavevector variation

By plotting the peak wavevector as a function of time, the reason for the discrepancy between the wavevector desired and that extracted after 15ns is found. It is due to the value of the peak wavevector varying with time.

This variation is shown in figure 6.8, and has some interesting features. The value of the peak wavevector varies the most just after the source is turned on. This is because in this period the pulse has not yet been properly formed within the waveguide.

Once the pulse has been established, the value of its peak wavevector is seen to gradually increase. An explanation for this is found by looking at the temporal evolution of the wavevector distribution which comprises the pulse, see figures 6.9a and 6.9b. When the prism is present, the magnitude of the lower value wavevectors decreases faster than that of the higher value wavevectors. This asymmetric decay causes the peak of the wavevector distribution to shift to higher values, as shown in figure 6.9a and 6.10. This behaviour is due to the ability of the light to radiate away from the waveguide when the prism is present. Since the lower wavevectors excite forward modes, the evanescent fields belonging to them extend further away from the waveguide core. As a consequence there is better coupling between these modes and the prism. This leads to the amplitude of the low value wavevectors in the waveguide decreasing faster than the higher value

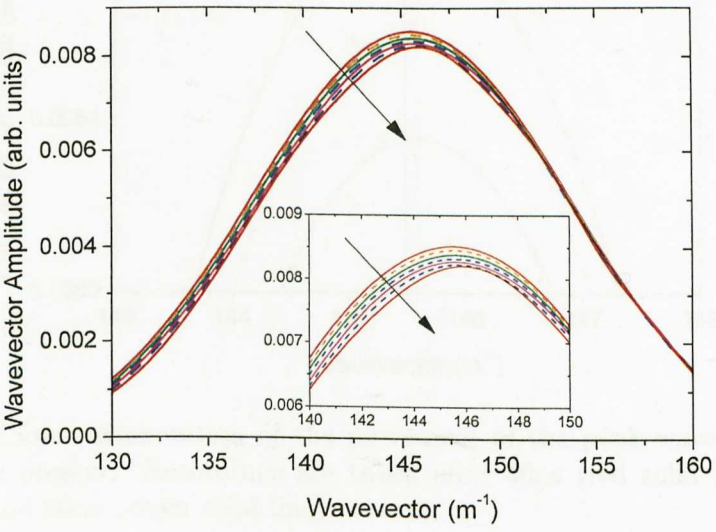

(a) Prism is present. Results obtained after 40, 50, 60, 70, 80, 90 and 100ns. Arrows show direction of increasing time.

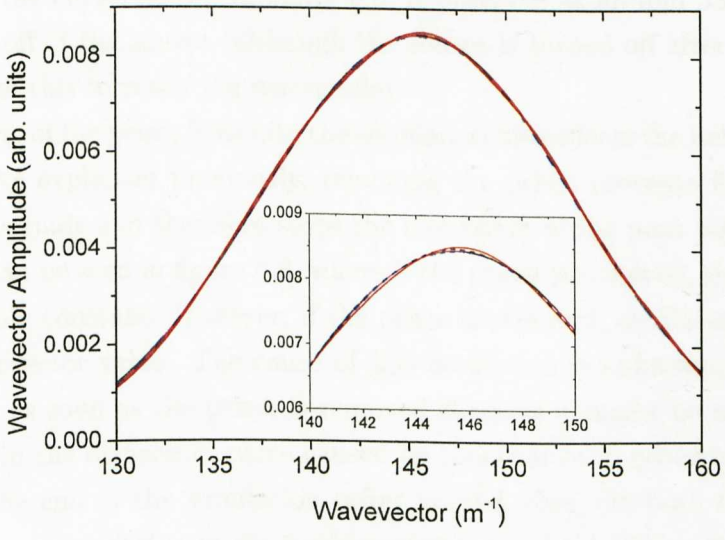

(b) Prism is not present. Results obtained after 50, 60, 70, 80 90 and 100ns

Figure 6.9: Effect of the presence of the prism on the wavevector distribution over time

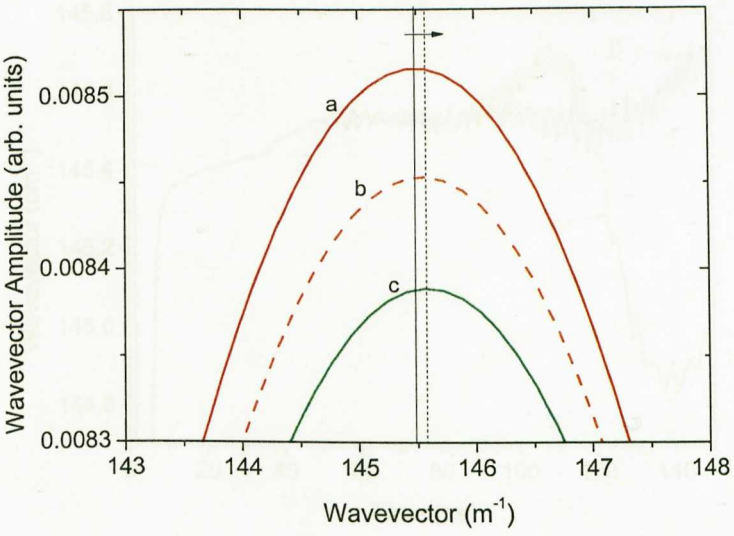

Figure 6.10: Closer examination of the movement of the peak wavevector distribution when prism is present. Recordings are taken after 40ns (red solid line), 50ns (orange dashed line) and 60ns (green solid line).

wavevectors. When the prism is not present the magnitude of the wavevectors comprising the pulse remains constant.

A kink in the curve, shown in figure 6.8, is observed at around 38ns. This is due to the switching off of the source (although the source is turned off after 36ns, it takes 2ns for the effect of this to reach the waveguide).

The removal of the prism 50ns into the simulation also affects the behaviour of the peak wavevector. As explained previously, removing the prism prevents light from coupling out of the waveguide and therefore stops the movement of the peak wavevector to higher values. This can be seen in figure 6.8, where if the prism is removed, the peak wavevector stays reasonably constant. However, if the prism is removed, oscillations are observed in the peak wavevector value. The cause of this oscillation is unknown, although the fact that it begins as soon as the prism is removed suggests it might be associated with the slight change in the dispersion curve caused by this change in geometry.

Towards the end of the simulation (after around 70ns), in both the cases with and without a prism, a variation in the peak wavevector is seen. When the prism is present, the peak wavevector previously observed to be rising seems to reach a constant value and, then, after 80ns, it starts to rise again. When the prism is not present the value of the peak wavevector first decreases and, then, as in the case when the prism is present, increases after 80ns. This increase in the value of the peak wavevector after 80ns simulation is due to the reflection of the pulse's edge at the ends of the waveguide. Increasing the length of

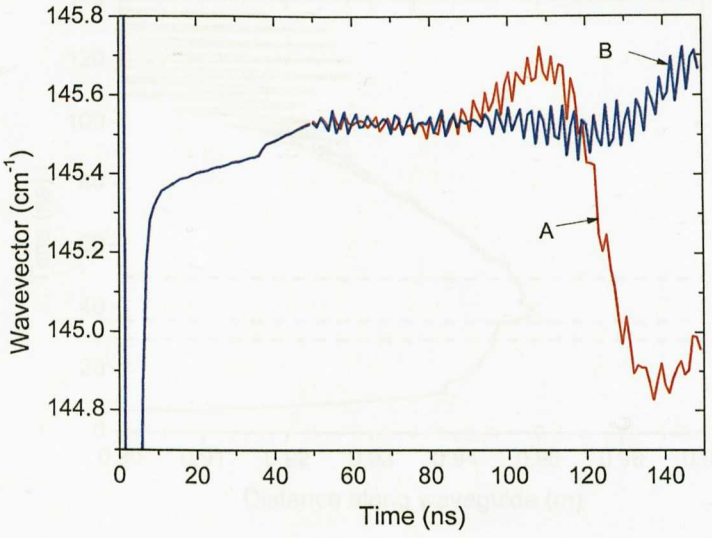

Figure 6.11: Effect of the waveguide length on the peak wavevector variation over time. A) Length of waveguide is 2.3m, B) Length of waveguide is 3.05m

the waveguide from 2.3m to 3.05m delays the onset of this behaviour, as shown in figure 6.11. As this figure shows, once the prism is removed the value of the peak wavevector remains constant. This happens for a greater amount of time, the longer the waveguide.

6.11 Centre of the pulse

The movement of the centre of the pulse is shown in figure 6.12. As with the peak wavevector, the greatest amount of movement occurs just after the source has been switched on. As can be seen in figure 6.12, the centre of the pulse is initially located on the left side of the waveguide and then quickly moves to the middle. It starts on the left since the source beam in the prism travels from left to right. This means it is the left side of the source beam which first hits the prism edge and generates the evanescent waves. As the rest of the beam front hits the prism edge, the centre of the pulse moves towards the middle of the waveguide.

When the source is switched off, the centre of the pulse jumps suddenly to the right. This is possibly due to the right side of the source beam being the last part of the beam to hit the prism edge, causing the evanescent field generated on the prism edge to move to the right. It should also be noted that additional frequencies are generated at this time point due to the decay of the source amplitude.

Once the source has been turned off, the centre of the pulse moves to the left along the waveguide. This is a consequence of the central wavevector of the pulse being larger

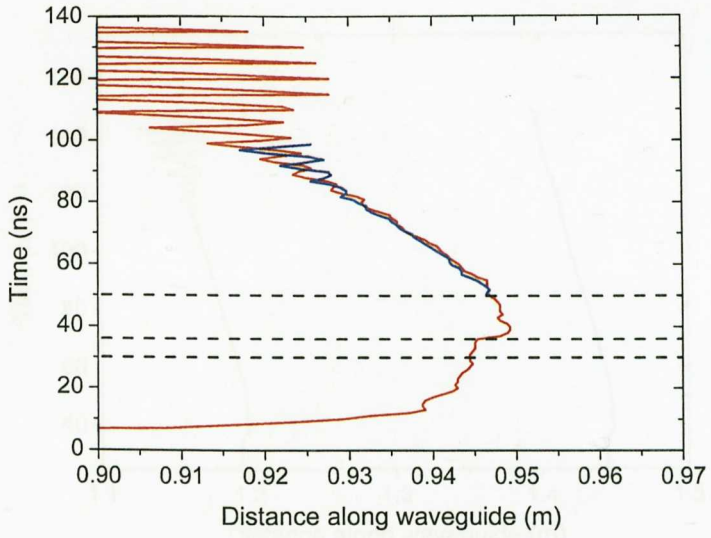

Figure 6.12: Variation in the centre of the pulse over time. Red line shows results from simulation with prism present (simulation ended after 150ns) , Blue line shows results from simulations with the prism removed (simulation ended after 100ns). The dashed lines are positioned at times of 36ns, 38ns and 50ns.

than that of the stopped light mode. The pulse excited is therefore a backward mode. The direction of the backward mode's group velocity is along the negative x-direction as a result of its phase velocity being in the positive x-direction (to the right along the waveguide). The phase velocity is in the positive x-direction since the injected source travels from left to right in the prism. As the prism is composed of a conventional material, the phase velocity of the beam must also travel from left to right and, therefore, its phase velocity component along the x-axis is directed in the positive direction.

Interestingly, there is not much difference in the movement of the pulse centres in the simulations with and without the prism present. This implies that there is only a small change in the dispersion curve, and hence the group velocity at the central wavevector, due to the presence of the prism.

Near the end of the simulations oscillations occur in the position of the pulse centre. This is due to interference with the edge of the pulse reflected from the end of the waveguide, as has been mentioned in the previous section. These oscillations are seen to be reduced if the waveguide is extended. Figure 6.13 shows that when the length of the waveguide is increased from 2.3m to 3.05m, these oscillations are drastically reduced. Note that the offset in the position of the pulse centres shown in figure 6.13 is a consequence of the fact that, since the waveguides are extended, the two pulses are injected into the waveguides at different distances from the ends.

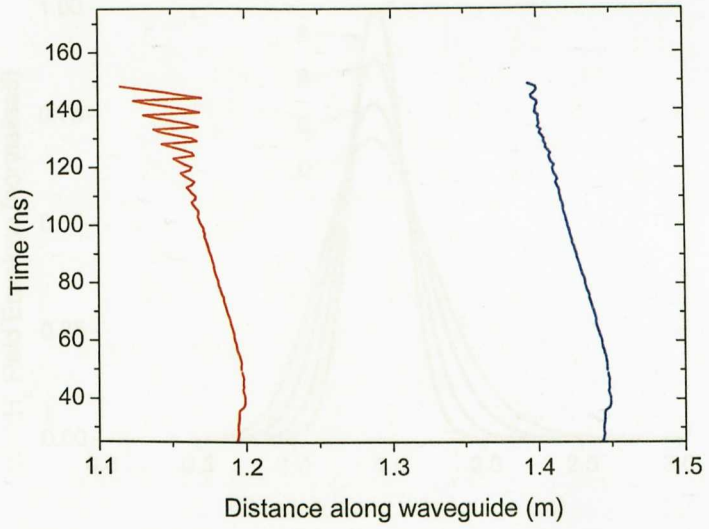

Figure 6.13: Effect of waveguide length on the movement of the pulse centre: (red left) length of waveguide is 2.3m; (blue right) length of waveguide is 3.05m

6.12 Pulse dispersion

The dispersion experienced by the pulse can be observed by plotting the pulse envelope over time, as in figure 6.14. The dispersion observed is due to the excitation of wavevectors either side of the stopped light point. The pulse is seen to extend faster along the waveguide in the positive x-direction than the negative. This is due to the steeper gradient of the dispersion curve at the lower wavevectors (the forward mode) than at the higher wavevectors (the backward mode).

In order to reduce the dispersion it would be necessary either to reduce the range of wavevectors excited, or to flatten the dispersion curve around the degeneracy point. The latter could be achieved via adjusting the geometry of the system.

6.13 Producing the stopped light mode

From the results shown previously, it can be seen that a crucial difficulty with exciting a specific mode in the prism geometry is that the central wavevector of the mode excited varies with time. Therefore, it is necessary to remove the prism not only to ensure light cannot radiate away from the waveguide, but also to ensure that the central wavevector of the pulse remains constant.

In an attempt to excite the stopped light mode the frequency of the source beam was changed to 4.38719GHz. This is the frequency of the degeneracy point when no prism is

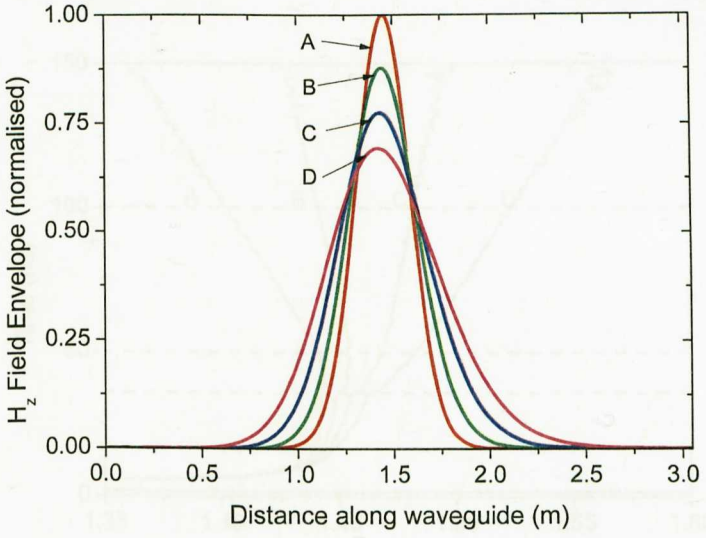

Figure 6.14: H_z-field distribution of the excited pulse along the waveguide's central axis at different times. In this simulation the prism was removed. Snapshots are taken at A) 40ns B) 60ns C) 80ns and D) 100ns

present and was found using the analytic method. The choice of which wavevector to use for the injected source beam was more difficult, since the peak wavevector value of the pulse will vary until the prism is removed.

In order to find the correct choice of source wavevector a range of angles for the source (corresponding to different wavevectors) was tested. The values for the angle θ used were 43.5 °, 44.0 °, 44.5 ° and 45.0 °. The movement of the pulse centre in simulations where these angles are used is shown in figure 6.15. As can be seen, by using the different angles it is possible to excite forward modes (propagating in the positive x-direction) and backward modes (propagating in the negative x-direction).To quantify the effect of the angle, the distance travelled by the pulse centre between 50ns and 100ns was recorded and is plotted in figure 6.16. The pulse's position after 100ns was used since this is before the interference due to pulse reflection becomes very large. Interpolation was then used to calculate the angle required in order for the movement of the pulse centre to be 0m. This was found to be 44.2345 °.

The displacement of the pulse centre when an angle of 44.2345° is used is seen in figure 6.17. The movement of the pulse centre was found to be 0.0003m (corresponding to 1 Yee cell), not 0 as predicted. Although this pulse is obviously not stopped, it is very slow. Its group velocity is 0.00002c and there should be no reason why, if more accurate parameters are chosen, stopped light could not be achieved. The reduction in the displacement of the pulse centre, relative to that found with the other angles, can

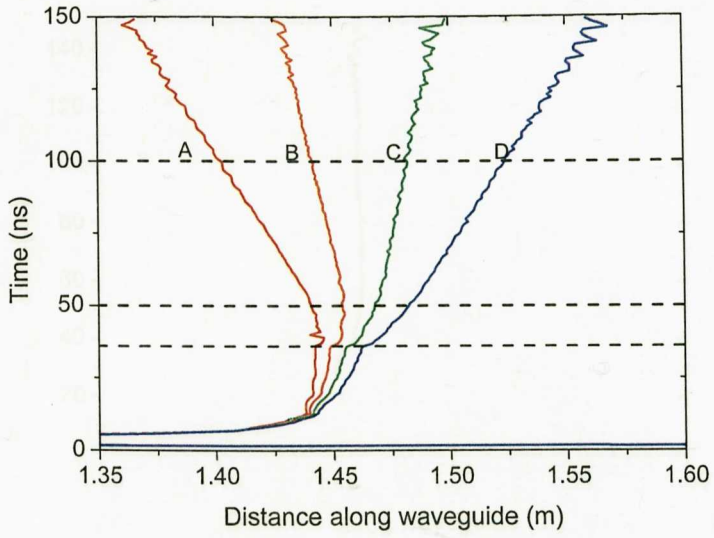

Figure 6.15: Movement of the centre of pulse when the source beam is injected at varying angles. Angle of the source beam used: A) 43.5° B) 44.0° C) 44.5° D) 45.0°. The prism is removed after 50ns in each simulation.

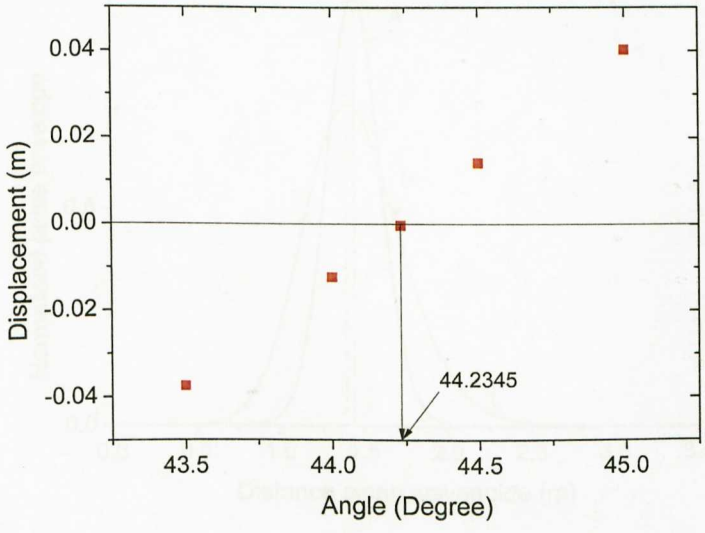

Figure 6.16: Displacement of the pulse centre between 50ns and 100ns as a function of injection angle.

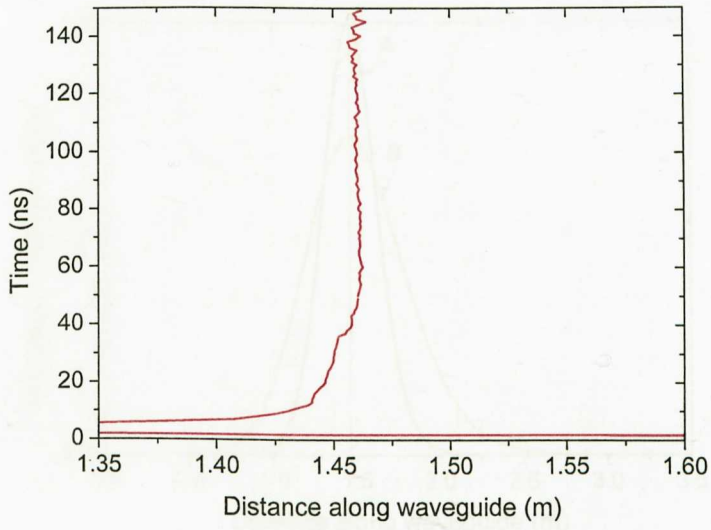

Figure 6.17: Movement of the pulse centre over time when the injection beam is angled at 44.2345°

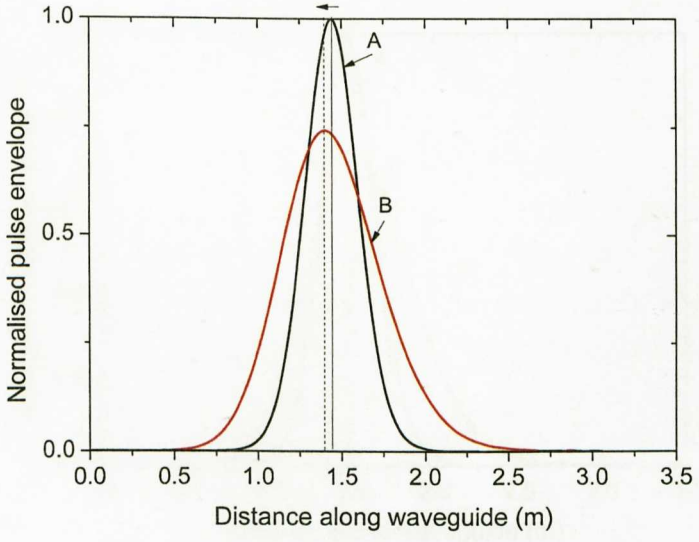

Figure 6.18: Evolution of pulse envelope when injection beam is set to an angle of 43.5°. Envelope after 50ns (Black), envelope after 100ns (Red)

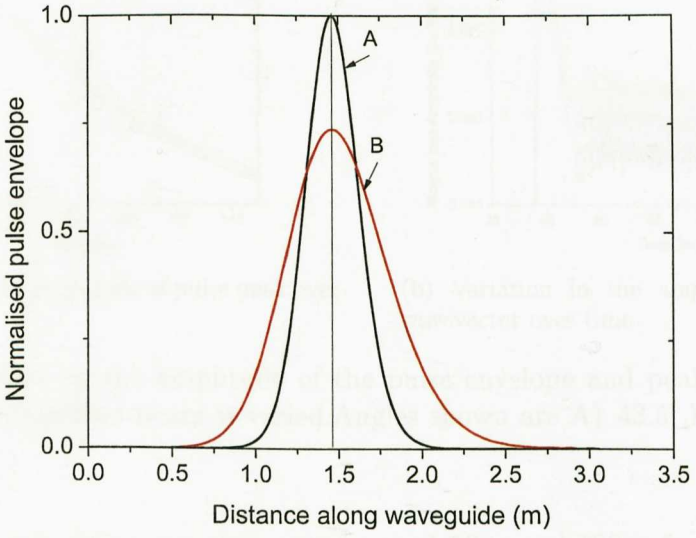

Figure 6.19: Evolution of pulse envelope when injection beam is set to an angle of 44.2345°. Envelope after 50ns (Black), envelope after 100ns (Red)

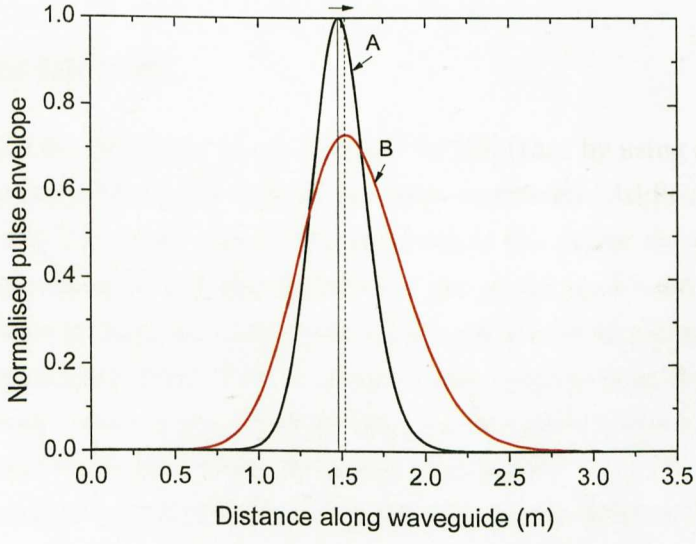

Figure 6.20: Evolution of pulse envelope when injection beam is set to an angle of 45°. Envelope after 50ns (Black), envelope after 100ns (Red)

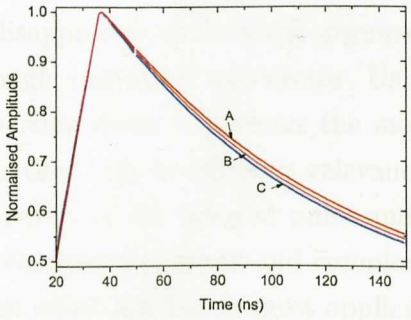

(a) Variation in the amplitude of pulse peak over time.

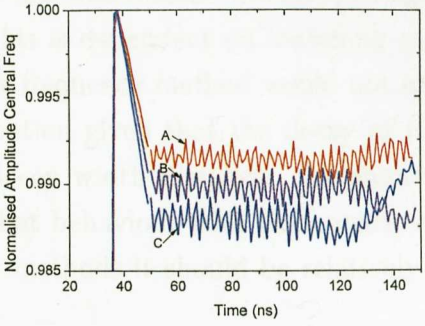

(b) Variation in the amplitude of the peak wavevector over time

Figure 6.21: Effect on the amplitude of the pulse envelope and peak wavevector when the angle of the injection beam is varied.Angles shown are A) 43.5°,B) 44.2345° and C) 45°.

be observed by comparing the pulse envelopes at 50ns and 100ns for the simulations in which angles of 43.5 ° , 44.2345 ° and 45.0 ° are used, see figures 6.18, 6.19 and 6.20.

Figures 6.18, 6.19 and 6.20 show a large decrease in the height of the pulse envelope over time. The decrease in the maximum amplitude of the pulse envelope is shown in figure 6.21a. However, this decrease in the H_z-field intensity is solely due to the pulse dispersion. Plotting the magnitude of the central wavevector over time, shows that once the prism is removed the magnitude of this wavevector stays constant, figure 6.21b.

6.14 Conclusions

By studying the same geometry, the claim made by [50] (that by using a prism the stopped mode can be excited and a pulse halted) has been confirmed. Additional features of this geometry have also been discovered. The presence of the prism not only allows light to radiate away from the core, but also favours the out coupling of lower value wavevectors. This asymmetric decay causes a shift in the pulse's peak wavevector, moving it away from that of the stopped light mode. This is an important point to consider when exciting the stopped light mode, since it is critical in order for the pulse to be stopped that it have the correct central wavevector when the prism is removed.

Another observation is that there is a slight shift in the centre of the pulse when the source is turned off. This occurs as a consequence of the right side of the source beam being the last point to hit the prism edge. This could be an important factor to consider in situations where the stop light mode is used to record data and read it out at a later time.

The most obvious area for future work is to examine the effect of introducing loss into the structure. Although it is claimed in [50] that this would cause the stopped light point to disappear (based on the argument of [64]) this is dependent on including the losses through a complex wavevector. Using a complex frequency method would not affect the dispersion curve and seems the most suitable option given that the decay of the pulse with time will be of more relevance than its decay width distance. By observing the behaviour of the injected pulse and matching that behaviour with that predicted using the complex frequency and complex wavevector methods it should be relatively easy to judge which method is most applicable.

Chapter 7

Conclusions

This thesis has examined some of the features of slow light in NRI waveguides. Particular attention has been paid to those aspects related to slow light and the trapped rainbow concept.

Initially, waveguides containing a lossless NRI material were examined. Using post-simulation analysis, the effective refractive index of modes propagating through these structures was extracted. An accurate check was then made between the simulation results and those predicted by analytic calculation. Over a range of core widths, the effective index values obtained using the two methods were found to agree to a high degree. A reduction of the propagating pulse's group velocity in waveguides containing thinner core widths was also observed.

Slowing the propagating mode by reducing the core width has been suggested in [17]. An alternative method of achieving slow light, that of increasing the refractive index of the core material, was proposed for use in Clarricoats-Waldron waveguides by [63]. In this thesis, this method is simulated in NRI waveguides. The variation in the effective refractive index of the pulse matched that predicted by an analytic method. As the core refractive index was increased, the pulse's group velocity decreased and its peak amplitude increased. Both of these features match those seen in simulations of waveguides with tapered core widths [51].

To make the simulations more realistic, loss was included in the NRI material mode. Gain material was then included in the waveguide to see if the degree of the effective loss could be reduced. The gain material was introduced in the form of a strip in the cladding material in a similar manner to that used for plasmonic waveguides [68]. It was found that, using this arrangement, it was possible to supply gain to the propagating pulse. As with plasmons, the gain experienced by the mode could be increased by reducing the separation between the core and the gain strip, increasing the width of the gain strip, and increasing the gain material's intrinsic gain. Through examination of the

confinement factor, it was confirmed that the higher frequency components of the mode excited extended further into the cladding than the lower frequency components.

After confirming the ability to supply gain to the propagating pulse through the use of a gain material in the cladding, the ability of this method to compensate for the loss of the NRI material was examined. With the appropriate choice of parameters it was found that loss in the core region could be compensated for by gain in the cladding. The real part of the effective refractive indices of the frequencies comprising the propagating pulse remained negative even in the regions of complete loss compensation and net gain.

As with the lossless case, the effect of varying the waveguide's core width is investigated. The thinner the waveguide core the greater the amount of gain experienced by the mode. This resulted from the increasing extension of the mode into the cladding with decreasing core width. When the change in the total energy density of the pulse was analysed it was found that a thinner core was required to completely compensate for the loss in the total energy of the pulse than that required to compensate for the loss at the pulse's central frequency. This is due to the asymmetric gain experienced by frequencies either side of the central frequency. The energy velocity of the pulse was also determined. This was achieved by finding the time required for the peak energy density of the pulse to travel between two points along the waveguide. By multiplying the complex wavevector with this velocity it was found that the complex frequency could be obtained

Finally, the use of prism coupling to excite the stopped light mode was investigated. Using this geometry a very slow light mode propagating at a speed of the order of 0.00002c was excited, confirming the results of [50]. Different post-simulation methods to those presented in [50] were used to examine the geometry. Using these it was discovered that the presence of the prism caused the central wavevector of the excited pulse to vary with time. This was caused by the variation in the rate of out coupling with wavevector. Due to this effect, there is an asymmetric reduction in the magnitude of the wavevector components around the stopped light point. This shifts the peak wavevector to higher values. Once the prism is removed, the amplitude of each wavevector remains reasonably constant, ensuring that the peak wavevector remains static.

From the simulations it was also observed that the center of the pulse shifted slightly when the source beam used to inject it was turned off. This shift was due to the source beam hitting the edge of the prism at an angle and, therefore, one side of the beam finishing before the other.

7.1 Future work

There are several areas where the work presented in this thesis could be extended. Recently, it has been suggested that the coupling between forward and backward modes would prevent the stopped light mode from existing for a long time in tapered waveguides [49]. So far this claim has been investigated using structures where the width of the waveguide core is tapered. A complementary method is to vary the refractive index of the core. This method of slowing down the light mode has been used in the slow light regime, but has not been extended to the stopped light point. In computer simulations this method could be used to engineer a more gradual taper. It would also be easier using this method to vary the gradient of the taper along the waveguide, i.e. reducing the gradient as the stopped light point is approached. Also, with regards to tapered waveguides, it would be interesting to determine why simulations seem to consistently show a fourfold increase of the pulse's peak amplitude [52, 51] at the stopped light point.

Another area which could be studied further is the use of a gain material to compensate for the loss in a NRI waveguide. Although the general principle of compensating loss by the introduction of gain has been examined in this thesis, the gain model used is static and therefore not realistic. The inclusion of non-linear equations to account for the population dynamics in the gain material would lead to more realistic results.

Lastly, future investigations could improve on the realistic description of the prism coupling geometry. The first step would be to introduce loss in the NRI material. Results would be particularly interesting because when loss is introduced through a complex wavevector it is believed that the stopped light mode would disappear [64]. This way, the existence of the stopped light mode in the presence of loss could be tested. The predictions from the complex wavevector and complex frequency methods could then be compared. The second step to make this geometry more realistic would be to introduce surface roughness at the core cladding interface. This could have a strong impact on the feasibility of trapping a stopped light mode within the waveguide for extended periods of time, as surface roughness could allow the mode to radiate into the cladding even in the absence of the prism.

To conclude, this thesis has examined different aspects of slow and stopped light in NRI waveguides. The general principles behind slowing light through reducing the core thickness and the magnitude of the core's intrinsic refractive index have been examined. The use of a gain material to compensate for the loss in the NRI material, and the positioning of a prism next to the waveguide as an alternate method of coupling to the stopped light point, have also been investigated. The next step is to make the simulations more realistic, paving the way for the experimental realisation of NRI waveguides.

Chapter 8

Appendix

8.1 Appendix A: The FDTD method

The basic principle of the FDTD method is that space and time can be divided into discrete units. Instead of acting on continuous variables, Maxwell's equations are modified so that they apply to discrete values of E- and H-fields, which are assigned to each point in space and modified at each time point.

The spatial discretisation is achieved by dividing the simulated region into cubic cells. The E- and H-field components are placed at the centre of each cell face and the middle of each cell edge, respectively.

The basic unit cell of this arrangement is called the Yee cell, Figure 8.1. As well as 3D, the Yee cell can be used to simulate 1D and 2D geometries in which the Yee cell is modified so that certain field values are located at the same positions.

In this work, only 2D simulations are carried out and the Yee cells used are all squares. The length of each side of the Yee cell is defined as Δx.

In the FDTD program, all distances are given in terms of the size of the Yee cell, as are the wavelengths of the frequencies excited. It is worth noting that provided the size of the Yee cell is used to define the simulation inputs, the results obtained are scalable, e.g. it could be possible, after a simulation has been run, to define the length of the Yee cell as being one meter and so a wave with a wavelength of 500 Yee cells would be a radio wave. If, however, the length of a Yee cell was defined as being one nanometer, then the same simulation would be examining optical radiation. In practice, though, there is often a simulation parameter which is scale dependent and so the choice of this value sets the scale of the simulation. An example of this would be if a realistic dispersive material was included. Since its optical properties vary with frequency and therefore with wavelength, the refractive index assigned to the material would define the frequency of the fields in the simulation and thus the dimensions of the simulation.

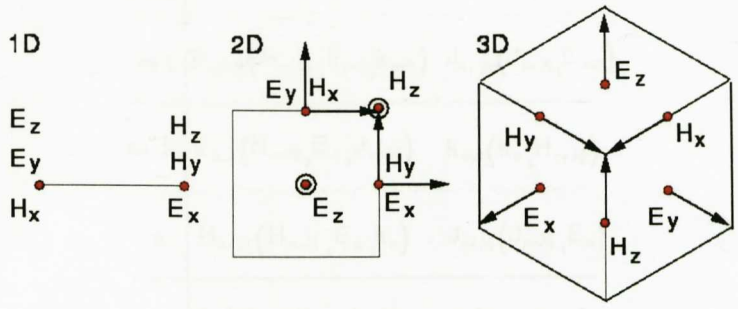

Figure 8.1: Layout of the Yee cell in 1, 2 and 3D.

As with space, time is also divided up into discrete units (steps)

Only one set of field values (either E or H) are updated in each step, withtableeplaceadv updated in the previous and following steps. It is common practive to define a simulation step as encompassing the update of both the E- and H-fields, thus half steps are used to maintain the separation E- and H-field updates. E-fields are taken to be updated on integer steps $(n + x)$, while H-fields are updated on half integers steps $(n + \frac{1}{2} + x)$. So, after one integer step, both fields have been updated, figure 8.2. The length of one whole time step is defined as Δt.

The discretisation of Maxwell's equations is achieved by representing:

- Averaged field values = Sometimes a field value is required at the half time step at which it is not calculated i.e. the value of the E-field at n+1/2 may be required. In such a situation, the field value is found by taking the average of the field's value half a time step before and after the time it is required, i.e. using the E-field value at n+1 and n.

- Spatial derivative = The rate of change with distance of a field component at a spatial location on the Yee cell. This is found by taking the difference between the field components either side of the desired position (in the direction of the derivative) and dividing by the spatial separation of the two (i.e. the length of the Yee cell).

- Temporal derivative = The rate of change with time of a field component at a

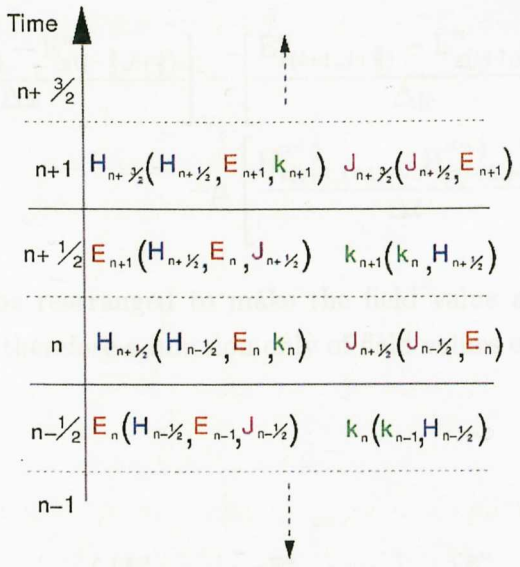

Figure 8.2: Fields updated in each time step.

particular time step. This is found by taking the difference between the field value components at the half time steps before and after the desired time step, and dividing the result by the time step.

An example of the equations used in an FDTD simulation are shown below. Here, the equations for a 2D geometry are examined for the TM mode (where only the H_z, E_x and E_z components are required). Note, for this example it is assumed that both the permittivity and permeability are independent of position and polarisation. In the notation for the discrete field values, it is usual for the spatial position (i, j, k) of the value to be written as a subscript, and the point in time (n) the value is calculated for to be written as a superscript, as in [78].

Starting with Faraday's equation, we have:

$$\nabla \times \mathbf{E} = -\mu_0 \frac{\partial \mathbf{H}}{\partial t}, \tag{8.1}$$

$$\frac{\partial \mathrm{E}_y}{\partial x} - \frac{\partial \mathrm{E}_x}{\partial y} = -\mu_0 \frac{\partial \mathrm{H}_z}{\partial t}, \tag{8.2}$$

$$\left[\frac{\mathrm{E}^n_{y(i+\frac{3}{2},,j+\frac{1}{2})} - \mathrm{E}^n_{y(i-\frac{1}{2},j+\frac{1}{2})}}{\Delta x}\right] - \left[\frac{\mathrm{E}^n_{x(i+1,,j+\frac{3}{2})} - \mathrm{E}^n_{x(i+1,j-\frac{1}{2})}}{\Delta y}\right] = -\mu\left[\frac{\mathrm{H}^{n+\frac{1}{2}}_{z(i+1,j+1)} - \mathrm{H}^{n-\frac{1}{2}}_{z(i+1,j+1)}}{\Delta t}\right]. \quad (8.3)$$

Equation (8.3) can be rearranged to make the field value at the latest time point ($\mathrm{H}_z^{n+\frac{1}{2}}$) the subject, and therefore a function only of field values calculated at earlier time steps:

$$\mathrm{H}^{n+\frac{1}{2}}_{z(i+1,j+1)} = \mathrm{H}^{n-\frac{1}{2}}_{z(i+1,j+1)} - \frac{\Delta t}{\mu_0}\left\{\left[\frac{\mathrm{E}^n_{y(i+\frac{3}{2},,j+\frac{1}{2})} - \mathrm{E}^n_{y(i-\frac{1}{2},j+\frac{1}{2})}}{\Delta x}\right] - \left[\frac{\mathrm{E}^n_{x(i+1,,j+\frac{3}{2})} - \mathrm{E}^n_{x(i+1,j-\frac{1}{2})}}{\Delta y}\right]\right\}. \quad (8.4)$$

Similarly, Ampere's equation can be discretised as:

$$\nabla \times \mathbf{H} = \epsilon_0 \frac{\partial \mathbf{E}}{\partial t}, \quad (8.5)$$

$$-\frac{\partial \mathrm{H}_z}{\partial x} = \epsilon_0 \frac{\partial \mathrm{E}_y}{\partial t}, \quad (8.6)$$

$$\frac{\partial \mathrm{H}_z}{\partial y} = \epsilon_0 \frac{\partial \mathrm{E}_x}{\partial t}, \quad (8.7)$$

$$-\left[\frac{\mathrm{H}^{n+\frac{1}{2}}_{z(i+2,j+1)} - \mathrm{H}^{n+\frac{1}{2}}_{z(i,j+1)}}{\Delta x}\right] = \epsilon_0\left[\frac{\mathrm{E}^{n+1}_{y(i+\frac{1}{2},j+1)} - \mathrm{E}^n_{y(i+\frac{1}{2},j+1)}}{\Delta t}\right], \quad (8.8)$$

$$\left[\frac{\mathrm{H}^{n+\frac{1}{2}}_{z(i+1,j+2)} - \mathrm{H}^{n+\frac{1}{2}}_{z(i+1,j)}}{\Delta y}\right] = \epsilon_0\left[\frac{\mathrm{E}^{n+1}_{x(i+1,j+\frac{1}{2})} - \mathrm{E}^n_{x(i+1,j+\frac{1}{2})}}{\Delta t}\right]. \quad (8.9)$$

Again, these equations can be rearranged allowing for the latest field value to be calculated:

$$\mathrm{E}^{n+1}_{y(i+\frac{1}{2},j+1)} = \mathrm{E}^n_{y(i+\frac{1}{2},j+1)} - \frac{\Delta t}{\epsilon_0}\left[\frac{\mathrm{H}^{n+\frac{1}{2}}_{z(i+2,j+1)} - \mathrm{H}^{n+\frac{1}{2}}_{z(i,j+1)}}{\Delta x}\right], \quad (8.10)$$

$$\mathrm{E}^{n+1}_{x(i+1,j+\frac{1}{2})} = \mathrm{E}^n_{x(i+1,j+\frac{1}{2})} + \frac{\Delta t}{\epsilon_0}\left[\frac{\mathrm{H}^{n+\frac{1}{2}}_{z(i+1,j+2)} - \mathrm{H}^{n+\frac{1}{2}}_{z(i+1,j)}}{\Delta y}\right]. \quad (8.11)$$

So, at integer time steps you would use equation (8.4) to calculate the next H-field value while at half-integer time steps you would use (8.10) and (8.11) to find the next E-field component values. The evolution of an EM field interacting with a system can therefore be determined simply by repeating these calculations; feeding the results found at one time step into the calculations for the next. Note, in the FDTD program the default value of ϵ_0 and $\mu_0$is 1. This value can be modified in the program (for instance to change the ϵ_∞ value of a material.

8.1.1 FDTD parameters

Several parameters in FDTD simulations can be varied to affect both the speed of the simulation and the accuracy of the results it produces.

The first parameter is the Courant factor (C_o) [78]. This defines the ratio between the time it takes for light to travel the distance Δx (calculated by $\Delta x/\mathrm{c}$ where c is the speed of light in free space) and the time step Δt. This factor affects the simulation stability. Too large a value and the simulation "blows up" , i.e. the fields increase in amplitude in an unphysical manner.

The relation between the temporal and spatial step size is given through:

$$\Delta t = \frac{C_0 \Delta x}{\mathrm{c}}, \tag{8.12}$$

where, Δx can be used to represent all the lengths of the Yee cells since the Yee cells used in all the simulations in this work are cubic $\Delta x = \Delta y = \Delta z$. Equation (8.12) is the same, no matter whether the terms are defined in SI or FDTD units (where c = 1).

The second parameter is the size of the Yee cell. The choice of size depends both on the geometry to be modelled (the smaller the features of the simulated structure relative to the wavelength of interest, the higher the required resolution) and on the wavelength of the light. Around 10-25 Yee cells per wavelength are necessary to be able to resolve the wave, the Nyquist frequency [87].

8.2 Appendix B: Analytic mode calculation

To serve as verification, the results obtained from the FDTD simulations were compared with those generated by an analytic mode solver created by other members of my research group. The mode solver is also able to calculate the mode properties in geometries, which it is difficult for the FDTD to model.

The architecture of the mode solver first generates the dispersion relation for the waveguide using the Transfer Matrix Method (TMM). A conformal mapping technique is used to generate a single value version of the dispersion relation, which is then solved using the Argument Principle Method (APM). This method is extremely useful, as it allows complex solutions to be found for multi-layered waveguide structures. This makes it ideal in examining the waveguide geometry when the gain material is included.

The TMM generates the dispersion relation for the waveguide by using solution ansatzs for the field in each layer of the waveguide [88]. This is a similar method to that used in section 4.3.2, except that in this case a sine term is also included, allowing odd modes to be examined as well as even:

$$\mathrm{H}_z(y) = e^{(-\gamma_i y)} \qquad y \geq 0, \tag{8.13}$$

$$\mathrm{H}_z(y) = A_i \cos(\kappa_i(y - y_{i-1})) + B_i \sin(\kappa_i(y - y_{i-1})) \qquad y_{i-1} > y > y_i, \tag{8.14}$$

$$\mathrm{H}_z(y) = A_N e^{(\gamma_i y)} \qquad y_{N-1} > y, \tag{8.15}$$

where, the i subscript with each variable denotes which layer that variable is calculated for, while N is the total number of layers, including the cover and substrate. The quantities A and B define the magnitude of each term and can vary between the different layers. As in section 4.3.2, the transverse field components are functions of the propagation wavevector β^2, i.e. $\kappa = \sqrt{k_0^2 n_i^2 - \beta^2}$ and $\gamma = \sqrt{\beta^2 - k_0^2 n_i^2}$. Using the solution ansatzs in each layer and the boundary equations, in (2.37), a transfer matrix can be produced. For the case of a TM mode it is expressed as:

$$M_i = \begin{pmatrix} \cos(\kappa_i d_i) & -\frac{\epsilon_i}{\kappa_i}\sin(\kappa_i d_i) \\ \frac{\kappa_i}{\epsilon_i}\sin(\kappa_i d_i) & \cos(\kappa_i d_i) \end{pmatrix}. \tag{8.16}$$

If, for each layer, a vector containing the values A and B is multiplied by the transfer matrix then the effect of the propagation across that layer is calculated. The value of these two quantities in the adjacent layer can then be determined:

$$\begin{pmatrix} A_{i+1} \\ B_{i+1} \end{pmatrix} = M_i \begin{pmatrix} A_i \\ B_i \end{pmatrix}. \tag{8.17}$$

This matrix multiplication leads to two simultaneous equations for A and B, $A(B,\kappa_i,\gamma_1)$ and $B(A,\kappa_i,\gamma_1)$. By specifying that the modes have to be bound, an additional relation between these two constants is obtained. This new constraint forces the quantities A

and B to be equal in the substrate (lowest layer) which, provided that the transverse field vectors become imaginary, allows the field in the substrate to be described using an exponential function:

$$F(\beta^2) = B_{sub} - \frac{\gamma_{sub}}{\epsilon_{sub}} A_{sub} = 0. \tag{8.18}$$

8.2.1 Calculating complex wavevector

Solutions to equation (8.18) can be obtained by finding the values of the longitudinal propagation constant which solve it.

However equation (8.18) is multi-valued. To make it easier to solve, it is mapped onto a new space. Once this has been accomplished it is possible to use the APM to find the solutions/roots. The argument principle method uses the generalised argument principle theorem, which can be used on a function provided that function does not contain any poles and is analytic. It states that the integral around a region, (provided that the integral does not pass through any roots of the function), can be used to determine the number of roots of the function which lie within the region. To search for these roots, the space which the function has been mapped onto is divided into a grid. The integral around each grid square is then taken. Those squares which contain no roots are ignored. In those which contain one root, the argument principle theorem is used to determine the exact position of that root. Regions which contain two or more roots are subdivided and the integrals of each sub-grid are found. The process is repeated until each root is isolated, so that its position can be determined.

The equations used for the conformal mapping can be reversed to obtain the longitudinal propagation constants denoted by each of these solutions.

8.2.2 Calculating complex frequency

In the calculation of the complex frequency results, the dispersion curve was derived as before, using the TMM method. However, the APM cannot be used to solve the dispersion equation with respect to the complex frequency, due to the presence of poles. To find the solutions the Newton-Raphson method is implemented. This method requires an initial guess for the $\mathrm{Im}(\omega)$ solution for a particular value of $\mathrm{Re}(\omega)$. Then, by using the dispersion curve and its derivative, a new more accurate $\mathrm{Im}(\omega)$ value is obtained. This new value is then substituted into the equation and the process is repeated until a $\mathrm{Im}(\omega)$ value with sufficient precision is found. When the derivative of the dispersion equation

is obtained, material modes have to be used in order to obtain the frequency dependence of the permittivity and permeability values in the equation.

8.3 Appendix C: The energy box

The derivation of the energy box used in the group's FDTD code is based upon Poyntings theorem. In the case of FDTD, the calculating of this theorem is difficult, since the E and H fields are separated by half a time step, as are the polarisation currents and magnetisations of the materials. As well as this, the E- and H-field components are calculated at different spatial positions.

Poynting's theorem can be arrived at using Ampere's and Faradays's equations:

$$\nabla \times \mathbf{H} = \epsilon_0 \frac{\partial \mathbf{E}}{\partial t} + \mathbf{j}, \tag{8.19}$$

$$\nabla \times \mathbf{E} = -\mu_0 \frac{\partial \mathbf{H}}{\partial t} - \mathbf{K}. \tag{8.20}$$

where $\mathbf{K}$ is the magnetic current density. It should be noted that the relative permittivity and permeability are determined partly through the electric and magnetic polarisation (or current densities), and that the ϵ_0 and μ_0 symbols in equation (8.19) and (8.20) denote the free space values. However, in the FDTD program the epsilon and mu infinity values ($\epsilon_\infty, \mu_\infty$) from the material models are included with the ϵ_0 and μ_0 values. This means that, when expresed in the form used in the FDTD program, these equations should be written as:

$$\nabla \times \mathbf{H}\,|^{n+\frac{1}{2}} = \epsilon \left(\frac{\mathbf{E}^{n+1} - \mathbf{E}^n}{\Delta t} \right) + \mathbf{j}^{n+\frac{1}{2}}, \tag{8.21}$$

$$\nabla \times \mathbf{E}|^n = -\mu \left(\frac{\mathbf{H}^{n+\frac{1}{2}} - \mathbf{H}^{n-\frac{1}{2}}}{\Delta t} \right) - \mathbf{K}^n, \tag{8.22}$$

where $\epsilon = \epsilon_0 \epsilon_\infty$ and $\mu = \mu_0 \mu_\infty$.

As detailed in section 8.1, the electric current density is calculated at the same half-integer time step as the H-field, while the magnetic current density is produced at the same half-integer time step as the electric field. To calculate the work done by the field on the material, the electric current density should be multiplied by the electric field [21] and the magnetic current density by the magnetic field vector. To ensure that the field values and currents are at the same point in the time step, the fields are averaged. To allow the equations to be simplified both sides of Ampere's equations is multiplied by

$\epsilon/\Delta t$ and Faraday's equation by $\mu/\Delta t$. Multiplying equations (8.21) and (8.22) through by these values gives:

$$\frac{\epsilon}{\Delta t}\left(\frac{\mathbf{E}^{n+1}+\mathbf{E}^{n}}{2}\right)\nabla\times\mathbf{H}\,|^{n+\frac{1}{2}}= \tag{8.23}$$

$$\frac{\epsilon}{\Delta t}\left(\frac{\mathbf{E}^{n+1}+\mathbf{E}^{n}}{2}\right)\epsilon\left(\frac{\mathbf{E}^{n+1}-\mathbf{E}^{n}}{\Delta t}\right)+\frac{\epsilon}{\Delta t}\left(\frac{\mathbf{E}^{n+1}+\mathbf{E}^{n}}{2}\right)\mathbf{j}^{n+\frac{1}{2}},$$

$$\frac{\mu}{\Delta t}\left(\frac{\mathbf{H}^{n+\frac{1}{2}}+\mathbf{H}^{n-\frac{1}{2}}}{2}\right)\nabla\times\mathbf{E}|^{n}= \tag{8.24}$$

$$\frac{\mu}{\Delta t}\left(\frac{\mathbf{H}^{n+\frac{1}{2}}+\mathbf{H}^{n-\frac{1}{2}}}{2}\right)\mu\left(\frac{\mathbf{H}^{n+\frac{1}{2}}-\mathbf{H}^{n-\frac{1}{2}}}{\Delta t}\right)+\frac{\mu}{\Delta t}\left(\frac{\mathbf{H}^{n+\frac{1}{2}}+\mathbf{H}^{n-\frac{1}{2}}}{2}\right)\mathbf{K}^{n}.$$

Adding the equations together allows a set of terms for the energy density of the field, the net Poynting vector into the region and the energy lost to the material within the region, to be obtained:

$$\frac{\partial U}{\partial t}= \tag{8.25}$$

$$\frac{\epsilon}{2\Delta t}\left(\mathbf{E}^{n+1}\mathbf{E}^{n+1}-\mathbf{E}^{n}\mathbf{E}^{n}\right)+\frac{\mu}{2\Delta t}\left(\mathbf{H}^{n+\frac{1}{2}}\mathbf{H}^{n+\frac{1}{2}}-\mathbf{H}^{n-\frac{1}{2}}\mathbf{H}^{n-\frac{1}{2}}\right),$$

$$\nabla\cdot\mathbf{S}= \tag{8.26}$$

$$\frac{1}{2}\left[\mathbf{H}^{n+\frac{1}{2}}\left(\nabla\times\mathbf{E}|^{n}\right)+\mathbf{H}^{n-\frac{1}{2}}\left(\nabla\times\mathbf{E}|^{n}\right)-\mathbf{E}^{n+1}\left(\nabla\times\mathbf{H}|^{n+\frac{1}{2}}\right)+\mathbf{E}^{n}\left(\nabla\times\mathbf{H}|^{n+\frac{1}{2}}\right)\right],$$

$$\mathbf{j}\cdot\mathbf{E}+\mathbf{K}\cdot\mathbf{H}= \tag{8.27}$$

$$-\frac{1}{2}\left[\mathbf{E}^{n+1}\mathbf{j}^{n+\frac{1}{2}}+\mathbf{E}^{n}\mathbf{j}^{n+\frac{1}{2}}+\mathbf{H}^{n+\frac{1}{2}}\mathbf{K}^{n}+\mathbf{H}^{n-\frac{1}{2}}\mathbf{K}^{n}\right].$$

The components of the net Poynting vector, along the three different grid axes, are found using different relations between the various field components. For example, equations (8.28) and (8.29) are the ones used to calculate the net flux along the x-axis:

$$\nabla\cdot\mathrm{S}_{x} = \mathrm{E}_{y}\left(\nabla\times\mathrm{H}_{z}\right)+\mathrm{H}_{z}\left(\nabla\times\mathrm{E}_{y}\right), \tag{8.28}$$

$$\nabla\cdot\mathrm{S}_{x} = \mathrm{H}_{y}\left(\nabla\times\mathrm{E}_{z}\right)+\mathrm{E}_{z}\left(\nabla\times\mathrm{H}_{y}\right). \tag{8.29}$$

So, using equation (8.26):

$$\nabla \cdot \mathrm{S}_x = \frac{1}{2}\left[\mathrm{H}_z^{n+\frac{1}{2}}\left(\nabla \times \mathrm{E}_y|^n\right) + \mathrm{H}_y^{n-\frac{1}{2}}\left(\nabla \times \mathrm{E}_z|^n\right) - \mathrm{E}_y^{n+1}\left(\nabla \times \mathrm{H}_z|^{n+\frac{1}{2}}\right) + \mathrm{E}_z^n\left(\nabla \times \mathrm{H}_y|^{n+\frac{1}{2}}\right)\right]. \tag{8.30}$$

If the curl operators are worked out and only the differentials which denote variation along the x direction are included, then the equation for the net Poynting flux, which enters the energy box region along the direction of the x-axis, is given by:

$$\nabla \cdot \mathrm{S}_x = \frac{1}{2}\left[\mathrm{H}_z^{n+\frac{1}{2}}\left(\frac{\partial \mathrm{E}_y^n}{\partial x}\right) + \mathrm{H}_y^{n-\frac{1}{2}}\left(\frac{\partial \mathrm{E}_z^n}{\partial x}\right) - \mathrm{E}_y^{n+1}\left(\frac{\partial \mathrm{H}_z^{n+\frac{1}{2}}}{\partial x}\right) + \mathrm{E}_z^n\left(\frac{\partial \mathrm{H}_y^{n+\frac{1}{2}}}{\partial x}\right)\right]. \tag{8.31}$$

The Poynting flux along the other axis can be calculated in a similar manner.

Bibliography

[1] D J Gauthier and R W Boyd. Fast light, slow light and optical precursors: What does it all mean? *Photonics Spectra*, pages 82–90, 2007.

[2] R Loudon. The propagation of electromagnetic energy through an absorbing dielectric. *Journal of Physics A: General Physics*, 3:233–45, 1970.

[3] R W Boyd, D J Gauthier, and A L Gaeta. Applications of slow light in telecommunications. *Optics and Photonics News*, 7:18–23, 2006.

[4] J T Mok and B J Eggleton. Expect more delays. *Nature*, 41433(811):811–2, 2005.

[5] M Salib, L Liao, R Jones, M Morse, A Liu, D Samara-Rubio, D Alduino, and M Paniccia. Silicon photonics. *Intel Technology Journal*, 08:143, 2004.

[6] T F Krauss. Slow light in photonic crystal waveguides. *Journal of Physics D: Applied Physics*, 40:2666–2670, 2007.

[7] M Soljacic, S G Johnson, S Fan, M Ibanescu, E Ippen, and J D Joannopoulos. Photonic-crystal slow-light enhancement of nonlinear phase sensitivity. *Journal of the Optical Society of America B*, 19:1052–9, 2002.

[8] J F McMillan, X Yang, N C Panoiu, R M Osgood, and C W Wong. Enhanced stimulated Raman scattering in slow-light photonic crystal waveguides. *Optics Letters*, 31:1235–7, 2006.

[9] M S Bigelow, N N Lepeshkin, and R W Boyd. Ultra-slow and superluminal light propagation in solids at room temperature. *Journal of Physics: Condensed Matter*, 16(R1321-R1340), 2004.

[10] S E Harris. Electromagnetically induced transparency. *Physics Today*, 50:36–42, 1997.

[11] M D Lukin and A Imamoglu. Controlling photons using electromagnetically induced transparency. *Nature*, 413:273–6, 2001.

[12] K Y Song, M G Herraez, and L Thevenaz. Observation of pulse delaying and advancement in optical fibers using stimulated brillouin scattering. *Optics Express*, 13:82–8, 2004.

[13] J D Joannopoulos, S G Johnson, J N Winn, and R D Meade. *Photonic Crystals Molding the Flow of Light 2nd Edition*. Princeton University Press, 2008.

[14] H Gersen, T J Karle, R J P Engelen, W Bogaerts, J P Korterik, E F van Hulst, T F Krauss, and L Kuipers. Real-space observation of ultraslow light in photonic crystal waveguides. *Physical Review Letters*, 94:073903, 2005.

[15] S Hughes, L Ramunno, J F Young, and J E Sipe. Extrinsic optical scattering loss in photonic crystal waveguides: Role of fabrication disorder and photon group velocity. *Physical Review Letters*, 94:033903, 2005.

[16] I V Shadrivov, A A Sukhoorukov, and Y S Kivshar. Guided modes in negative-refractive-index waveguides. *Physical Review E*, 67(057602):057602, 2003.

[17] K L Tsakmakidis, A Boardman, and O Hess. 'Trapped rainbow' storage of light in metamaterials. *Nature*, 450(15):397–01, 2007.

[18] V G Veselago. The electrodynamics of substances with simultaneously negative values of ϵ and μ. *Soviet Physics Uspekhi*, 10(4):509–14, 1968.

[19] G V Eleftheriades and K G Balmain, editors. *Negative-Refraction Metamaterials*. Wiely-InterScience, 2005.

[20] D Halliday, R Resnick, and J Walker, editors. *Fundamentals of Physics*. Wiley, 6th edition, 2001.

[21] J D Jackson. *Classical Electrodynamics*. John Wiley & Sons, 1999.

[22] J B Pendry, A J Holden, W J Stewart, and I Youngs. Extremely low frequency plasmons in metallic mesostructures. *Physical Review Letters*, 76(25):4773–6, 1996.

[23] J B Pendry, A J Holden, D J Robbins, and W J Stewart. Magnetism from conductors and enhanced nonlinear phenomena. *IEEE Transactions on Microwave Theory and Techniques*, 47(11):2075–84, 1999.

[24] D R Smith, W J Padilla, D C Vier, S C Nemat-Nasser, and S Schultz. Composite medium with simultaneously negative permeability and permittivity. *Physical Review Letters*, 84(18):4184–7, 2000.

[25] R A Shelby, D R Smith, and S Schultz. Experimental verification of a negative index of refraction. *Science*, 292(5514):77–9, 2001.

[26] S Zhang, W Fan, N N Panoiu, K J Mallory, R M Osgood, and S R J Brueck. Experimental demonstration of near-infrared negative-index metamaterials. *Physical Review Letters*, 95(137404), 2005.

[27] V M Shalaev, W Cai, U K Chettiar, H-K Yuan, A K Sarychev, V P Drachev, and A V Kildishav. Negative index of refraction in optical metamaterials. *Optics Letters*, 30(24):3356–8, 2005.

[28] G Dolling, C Enkrich, M Wegener, C M Soukoulis, and S Linden. Low-loss negative-index metamaterial at telecommunication wavelengths. *Optics Letters*, 31(12):1800–2, 2006.

[29] G Dolling, M Wegener, C M Soukoulis, and S Linden. Negative-index metamaterial at 780nm wavelength. *Optics Letters*, 32(1):53–5, 2007.

[30] S Xiao, U K Chettiar, A V Kildishev, V P Drachev, and V M Shalaev. Yellow-light negative-index metamaterials. *Optics Letters*, 34:3478–80, 2009.

[31] P Kinsler and M W McCall. Criteria for negative refraction in active and passive media. *Microwave and Optical Technology Letters*, 50:1804–7, 2008.

[32] M W McCall, A Lakhtaka, and W S Weiglhofer. The negative index of refraction demystified. *European Journal of Physics*, 23:353–9, 2002.

[33] A. Schuster. *An introduction to the theory of optics*. Edward Arnold, 1904.

[34] Y Sivan, S Xiao, U K Chettiar, A V Kildishav, and V M Shalaev. Frequency-domain simulations of a negative-index material with embedded gain. *Optics Express*, 17:24060–24074, 2009.

[35] S Wuestner, A Pusch, K L Tsakmakidis, J M Hamm, and O Hess. Overcoming losses with gain in a negative refractive index metamaterial. *Physical Review Letters*, 105:127401, 2010.

[36] L V Alekseyev and Narimanov. Slow light and 3D imaging with non-magnetic negative index systems. *Optics Express*, 14(23):11184–93, 2006.

[37] T Jiang and Y Feng. Compensating loss with gain in slow-light propagation along slab waveguide with anisotropic metamaterial cladding. *Optics Letters*, 34:3869–71, 2009.

[38] T Jiang and Y Feng. Slow and frozen waves in a planar air waveguide with anisotripic metamaterial cladding. In *Proceedings of International Conference on Microwave and Millimeter technology*, volume 4, pages 1627–30, 2008.

[39] C R Pollock and M Lipson. *Integrated Photonics*. Kluwer Academic Publishers, 2003.

[40] R Ruppin. Surface polaritons of a left-handed medium. *Physics Letters A*, 277:61–4, 2000.

[41] W L Barnes. Surface plasmon-polariton length scales: a route to sub-wavelength optics. *Journal of Optics A: Pure and Applied Optics*, 8(S87-S93), 2006.

[42] D-K Qing and G Chen. Goos-hänchen shifts at the interfaces between left- and right-handed media. *Optics Letters*, 29(8):872–74, 2004.

[43] K L Tsakmakidis, A Klaedtke, D P Aryal, C Jamois, and O Hess. Single-mode operation in the slow-light regime using oscillatory waves in generalized left-handed heterostructures. *Applied Physics Letters*, 89(201103), 2006.

[44] Y He, Z Cao, and Q Shen. Guided optical modes in asymmetric left-handed waveguides. *Optics Communications*, 245:125–35, 2005.

[45] R L Smith. The velocities of light. *American Journal of Physics*, 38:978–84, 1970.

[46] A C Peacock and N G R Broderick. Guided modes in channel waveguides with a negative index of refraction. *Optics Express*, 11(20):2502–10, 2003.

[47] J He and S He. Slow propagation of electromagnetic waves in a dielectric slab waveguide with a left-handed material substrate. *IEEE Microwave and Wireless Components Letters*, 16(2):96–98, 2005.

[48] A W Snyder and J D Love. *Optical Waveguide Theory*. Chapman and Hall, 1983.

[49] J He, Y He, and Z Hong. Backward coupling of modes in a left-handed metamaterial tapered waveguide. *IEEE Microwave and Wireless Components Letters*, 20:378–80, 2010.

[50] Q Bai, J Chen, N-H Shen, C Cheng, and H-T Wang. Controllable optical black hole in left-handed materials. *Optics Express*, 18:2106–2115, 2010.

[51] T Jiang, J Zhao, and Y Feng. Stopping light by an air waveguide with anisotropic metamaterial cladding. *Optics Express*, 17(1):170–7, 2008.

[52] J He, Y Jin, Z Hong, and S He. Slow light in a dielectric waveguide with negative-refractive-index photonic crystal cladding. *Optics Express*, 16(15):11077–82, 2008.

[53] Y Saito and T Baba. Stopping of light by the dynamic tuning of photonic crystal slow light device. *Optics Express*, 18:17141–53, 2010.

[54] Y Zhang, X Zhang, T Mei, and M Fiddy. Negative index modes in surface plasmon waveguides : a study of the relations between loss less and lossy cases. *Optics Express*, 18:12213–25, 2010.

[55] K L Tsakmakidis, C Hermann, A Klaedtke, C Jamois, and O Hess. Surface plasmon polaritons in generalized slab heterostructures with negative permittivity and permeability. *Physical Review B*, 73(085104), 2006.

[56] J B Pendry, L Martub-Moreno, and F J Garcia-Vidal. Mimicking surface plasmons with structured surfaces. *Science*, 305(5685):847–8, 2004.

[57] Q Gan, Z Fu, Y Ding, and F Bartoli. Ultrawide-bandwidth slow-light system based on THz plasmonic graded metallic grating structures. *Physical Review Letters*, 100(256803), 2008.

[58] Q Gan, Y Ding, and F Bartoli. 'Rainbow' trapping and releasing at telecommunication wavelengths. *Physical Review Letters*, 102(056801), 2009.

[59] Z Fu, Q Gan, Y J Ding, and F Bartoli. From waveguiding to spatial localization of THz waves within a plasmonic metallic grating. *IEEE Journal of Selected Topics in Quantum Electronics*, 14(2):486–490, 2008.

[60] Q Gan, Y Gao, K Wagner, D V Vezenov, Y J Ding, and F J Bartoli. Experimental verification of the "rainbow" trapping effect in plasmonic graded gratings. *arXiv:1003.4060vi*, 2010.

[61] P J B Clarricoats. Backward waves in waveguides containing dielectric. *Proceedings of the IEE - Part C : Monographs*, 108:496–501, 1961.

[62] A Salandrino and D N Christodoulides. Negative index clarricoats-waldron waveguides for terahertz and far infrared applications. *Optics Express*, 18:3626–3631, 2010.

[63] W Wang, J He, X Li, and Z Hong. Slow light in the Ga-As-rod-loaded metallic waveguide for terahertz wave. *Optics Express*, 18:11132–11137, 2010.

[64] A Reza, M M Dignam, and S Hughes. Can light be stopped in realistic metamaterials? *Nature (London)*, 455(E10):E10, 2008.

[65] A Reza. The optical properties of metamaterial waveguide structures. Master's thesis, Queen's University, Kingston, Ontario, Canada, 2008.

[66] K C Huang, E Lidorikis, X Jiang, J D Joannopoulos, and K A Nelson. Nature of lossy Bloch states in polaritonic photonic crystals. *Physical Review B*, 69:195111, 2004.

[67] S A Maier. Gain-assisted propagation of electromagnetic energy in subwavelength surface plasmon polariton gap waveguides. *Optics Communications*, 258:295–9, 2006.

[68] M P Nezhad, K Tetz, and Y Fainman. Gain assisted propagation of surface plasmon polaritions on planar metallic waveguides. *Optics Express*, 12(17):4072–8, 2004.

[69] D Correia and J M Jin. Theoretical analysis of left-handed metamaterials using FDTD-PML method. In *Proceedings of Microwave and Optoelectronics Conference,2003*, volume 2, pages 1033–6. IEEE MTT-S, 2003.

[70] R W Ziolkowski and E Heyman. Wave propagation in media having negative permittivity and permeability. *Physical Review E*, 64(056625), 2001.

[71] N. W. Ashcroft and N. D. Mermin. *Solid State Physics*. Saunders College, 1976.

[72] R W Ziolkowski. Pulsed and CW Gaussian beam interactions with double negative metamaterial slabs. *Optics Express*, 11(7):662–81, 2003.

[73] Y Zhao, P Belov, and Y Hao. Accurate modeling of the optical properties of left-handed media using a finite-difference time-domain method. *Physical Review E*, 75(037602), 2007.

[74] S A Cummer. Dynamics of causal beam refraction in negative refractive index materials. *Applied Physics Letters*, 82(13):2008–10, 2003.

[75] A S Nagra and R A York. FDTD analysis of wave propagation in nonlinear absorbing and gain media. *IEEE Transactions on Antennas and Propagation*, 46(3):334–40, 1998.

[76] Th. Koschny, A. Fang, and C. M. Soukoulis. Self-consistent calculations of loss-compensated fishnet metamaterials. *Physical Review B*, 82:121102(R), 2010.

[77] A A Govyadinov, V A Podolskiy, and M A Noginov. Active metamaterials: Sign of refractive index and gain-assisted dispersion managment. *Applied Physics Letters*, 91:191103, 2007.

[78] A. Taflove and S. C. Hagness, editors. *Computational Electrodynamics: The Finite-Difference Time-Domain Method.* Artech House, 3rd edition, 2005.

[79] Stuart.R.D. *Fourier Analysis.* Methuen & Co LTD, 1961.

[80] Y Zhao, P Belov, and Y Hao. Accurate modelling of left-handed metamaterials using finite-difference time-domain method with spatial averaging at the boundaries. *Journal of Optics A: Pure and Applied Optics*, 9:S468–75, 2007.

[81] H A Cherin. *An Introduction To Optical Fibers.* McGraw-Hill International Book Company, 1983.

[82] J B Pendry, D Schurig, and D Smith. Controlling electromagnetic fields. *Science*, 312(5781):1780–2, 2006.

[83] Y Zhao, C Argyropoulos, and Y Hao. Dispersive finite-difference time-domain simulation of electromagnetic cloaking devices. In *Proceedings Antennas and Propagation Conference, LAPC 2008*, pages 429–32, 2008.

[84] D B Li and C Z Ning. Giant modal gain, amplified surface plasmon-polariton propagation, and slowing down of energy velocity in a metal-semiconductor-metal structure. *Physical Review B*, 80:153304, 2009.

[85] P Kinsler and M W McCall. Causality-based criteria for a negative refractive index must be used with care. *Physical Review Letters*, 101:167401, 2008.

[86] M I Stockman. Criterion for negative refraction with low optical losses from a fundamental principle of causality. *Physical Review Letters*, 98:177404, 2007.

[87] D. M. Sullivan. *Electromagnetic simulation using the FDTD method.* Wiley-IEEE Press, 2000.

[88] M-S Kwon and S-Y Shin. Simple and fast numerical analysis of multilayer waveguide modes. *Optics Communications*, 223:119–126, 2004.